University of Kentucky

UKnowledge

Theses and Dissertations--Chemical and Materials Engineering

Chemical and Materials Engineering

2013

ELECTROMECHANICAL INTERACTION ON THE DEFORMATION BEHAVIOR OF METALLIC MATERIALS

Guangfeng Zhao
University of Kentucky, zhaomagf@gmail.com

Right click to open a feedback form in a new tab to let us know how this document benefits you.

Recommended Citation

Zhao, Guangfeng, "ELECTROMECHANICAL INTERACTION ON THE DEFORMATION BEHAVIOR OF METALLIC MATERIALS" (2013). *Theses and Dissertations--Chemical and Materials Engineering*. 19.
https://uknowledge.uky.edu/cme_etds/19

This Doctoral Dissertation is brought to you for free and open access by the Chemical and Materials Engineering at UKnowledge. It has been accepted for inclusion in Theses and Dissertations--Chemical and Materials Engineering by an authorized administrator of UKnowledge. For more information, please contact UKnowledge@lsv.uky.edu.

STUDENT AGREEMENT:

I represent that my thesis or dissertation and abstract are my original work. Proper attribution has been given to all outside sources. I understand that I am solely responsible for obtaining any needed copyright permissions. I have obtained and attached hereto needed written permission statements(s) from the owner(s) of each third-party copyrighted matter to be included in my work, allowing electronic distribution (if such use is not permitted by the fair use doctrine).

I hereby grant to The University of Kentucky and its agents the non-exclusive license to archive and make accessible my work in whole or in part in all forms of media, now or hereafter known. I agree that the document mentioned above may be made available immediately for worldwide access unless a preapproved embargo applies.

I retain all other ownership rights to the copyright of my work. I also retain the right to use in future works (such as articles or books) all or part of my work. I understand that I am free to register the copyright to my work.

REVIEW, APPROVAL AND ACCEPTANCE

The document mentioned above has been reviewed and accepted by the student's advisor, on behalf of the advisory committee, and by the Director of Graduate Studies (DGS), on behalf of the program; we verify that this is the final, approved version of the student's dissertation including all changes required by the advisory committee. The undersigned agree to abide by the statements above.

Guangfeng Zhao, Student

Dr. Fuqian Yang, Major Professor

Dr. Fuqian Yang, Director of Graduate Studies

ELECTROMECHANICAL INTERACTION ON THE DEFORMATION BEHAVIOR OF METALLIC MATERIALS

DISSERTATION

A dissertation submitted in partial fulfillment of the
Requirements for the degree of Doctor of Philosophy in the
College of Engineering
at the University of Kentucky

By

Guangfeng Zhao

Lexington, Kentucky

Advisor: Dr. Fuqian Yang, Professor of Materials Engineering
University of Kentucky, Lexington, Kentucky

2013

Copyright © Guangfeng Zhao 2013

ABSTRACT OF DISSERTATION

ELECTROMECHANICAL INTERACTION ON THE
DEFORMATION BEHAVIOR OF METALLIC MATERIALS

Metallic materials play important roles in providing electrical, thermal, and mechanical functions in electronic devices and systems. The understanding of the electrical-thermal-mechanical interaction caused by the passage of electric current with high density is important to improve the performance and reliability of electronic assembly and packaging. The electromechanical interaction on the deformation behavior of copper and tin is studied in this work.

The electromechanical response of Cu strips was studied by passing a DC electric current. The electric resistance linearly increased with time before the occurrence of electric fusing. The electrothermal interaction led to the buckling of the Cu strips with the maximum deflection increasing with the increase of the electric current density. The total strain was found to be proportional to the square of the electric current density. A power law relation was used to describe the dependence of the time-to-fusing on the electric current density.

Using the nanoindentation technique, the effect of electric current on the indentation deformation of copper and tin was studied. The reduced contact modulus of copper and tin decreased with increasing the electric current density. With the passage of a DC electric current, the indentation hardness of copper increased slightly with increasing electric current density. With the passage of an AC electric current, the indentation hardness of copper decreased with increasing the indentation deformation. With the passage of a DC electric current, the indentation hardness of tin decreased with increasing the indentation load, showing the normal indentation size effect. Both the limit of infinite depth and the characteristic length were dependent on the electric current density.

Using the tensile creep technique, the creep deformation of pure tin was studied with the passage of a DC electric current. The steady state creep rate increased with the increase in temperature, tensile stress and electrical current density. For the same tensile stress and the same chamber temperature, the steady state creep rate increased linearly with the square of the electric current density. The electric current density has no significant effect on the stress exponent and activation energy of the tensile creep of tin for the experimental conditions.

KEYWORDS: Metallic Materials, Electromechanical Interaction, Joule Heat, Nanoindentation, Creep Deformation

Guangfeng Zhao

Student's Signature

05/02/2013

Date

ELECTROMECHANICAL INTERACTION ON THE
DEFORMATION BEHAVIOR OF METALLIC MATERIALS

By

Guangfeng Zhao

Dr. Fuqian Yang

Director of Dissertation

Dr. Fuqian Yang

Director of Graduate Studies

05/02/2013

Date

Dedicated to my grandparents, parents and sister

ACKNOWLEDGEMENTS

I want to express my deepest acknowledge to my advisor Dr. Fuqian Yang, for his academic guidance, continuous encouragement, unselfish advising and friendship during my doctoral study and dissertation work.

I am also most grateful to the members of my committee, Dr. Thomas John Balk, Dr. Richard E. Eitel, and Dr. Yuan Liao for their time, efforts, and suggestion throughout my doctoral research.

My gratitude also goes to my instructors: Dr. Yang-Tse Cheng, Dr. Tongguang Zhai, Dr. Bruce J. Hinds, Dr. Richard E. Eitel, Dr. Matthew J. Beck, Dr. Jimmie Joe Cathey, and Dr. Ingrid St. Omer for their teachings and the high quality scholarship, to which I aspire.

I would like to thank Bruce Cole, Chelsea Hansing, Nancy Miller, Jerry Vice and Jerry Rougeux their assistant during my doctoral study.

I also would like to thank my lab mates, especially Ding Li, Juchuan Li, Ming Liu, Wei Sun, and Ning Zhang, for their support and help on my research. We have made our Ph.D. lives fun and productive.

My deepest gratitude is to my grandparents, parents and sister, for the love and encouragement which promote the accomplishment of the dissertation.

TABLE OF CONTENTS

ACKNOWLEDGEMENTS iii

List of Tables viii

List of Figures ix

Chapter 1 Introduction 1

Chapter 2 Literature review 4

2.1 Metallic materials 4

2.2 Current effect 6

2.2.1 Joule heating 6

2.2.2 Electromigration 7

2.3 Microstructure evolution 9

2.4 Current induced deformation 11

2.5 Indentation 14

2.6 Creep deformation 17

2.6.1 Tensile creep 18

2.6.2 Compression creep 20

2.6.3 Shear creep 21

2.6.4 Impression creep 22

2.6.5 Indentation creep 25

2.6.6 Stress relaxation.. 26

2.6.7 Electrical creep deformation.. 28

Chapter 3 Electromechanical responses of Cu strips 30

3.1 Introduction 30

3.2 Current-induced buckling of an elastic strip 31

3.3 Experimental 33

3.4 Results and discussion... 34

3.5 Summary 41

Chapter 4 Effect of electric current on nanoindentation of copper wires* 51

4.1 Introduction 51

4.2 Experimental 52

4.3 Results and discussion... 53

4.4 Summary 59

Chapter 5 Effect of alternating electric current on the nanoindentation of copper*. 65

5.1 Introduction 65

5.2 Experimental 67

5.3 Results and discussion... 68

5.3.1 Electrothermal curves 68

5.3.2 Electric nanoindentation 69

5.4 Summary 74

Chapter 6 Electric current effect on the nanoindentation behavior of tin* 81

6.1 Introduction 81

6.2 Electrothermal analysis 82

6.3 Experimental 84

6.4 Results and discussion 85

6.4.1 Electrothermal curves 85

6.4.2 Electric nanoindentation 86

6.5 Summary 93

Chapter 7 Effect of DC current on the tensile creep of pure tin 102

7.1 Introduction 102

7.2 Experimental 103

7.3 Results and discussion 104

7.3.1 Electrothermalbehavior 104

7.3.2 Tensile creep 105

7.3.3 Dependence of creep rate on electric current and tensile stress 107

7.3.4 Activation strain volume and activation energy 109

7.4 Summary 111

Chapter 8 Summary 122

8.1 Conclusion.. 122

8.2 Future work 125

8.2.1 Characterization of Joule heat and temperature distribution in metallic materials.. 125

8.2.2 Microstructure evolution 126

8.2.3 Electromechanical response of metallic materials.. 126

8.2.4 Indentation deformation of metallic materials.. 127

8.2.5 Creep behavior of metallic materials.. 127

Reference 128

Vita 149

List of Tables

Table 3.1 Summary of the current exponent 43

Table 4.1 Variation of the temperature rise with electric current density 61

Table 5.1 Variation of the β value with the indentation load 75

Table 5.2 Variation of the H_0 and λ values with the electric current density 75

Table 6.1Variation of the H_0 and h^* values with the electric current density 95

Table 7.1 Stress exponents for the creep deformation of Sn under the action of electric current 113

Table 7.2 List of the stress exponents and activation energies for the creep of Sn . 114

Table 7.3 Apparent activation energies for the creep deformation of Sn under the action of electric current 115

List of Figures

Figure 3.1 Deflection of a copper strip of 0.085 mm in thickness as a function of time under the action of an electric current of19.24kA/cm^2 (length of the Cu strip: 50 mm) 44

Figure 3.2 An SEM image of a melted Cu strip showing three distinct regions – melted region, heat-affected zone, and oxidation region (Cu-strip thickness: 0.085 mm, Cu-strip length: 50 mm, electric current density: 20.72 kA/cm^2).... 45

Figure 3.3 SEM micrographs of a melted Cu strip; (a) microstructure in the melted region, (b) microstructure in the heat affected zone, and (c) microstructure in the oxidation region (Cu-strip thickness: 0.085 mm, Cu-strip length: 50 mm, electric current density: 20.72 kA/cm^2) 46

Figure 3.4 Two-dimensional Synchrotron XRD (2D XRD) patterns of the melted Cu strip in different regions; (a) rolled Cu, (b) oxidation region, (c) heat-affected zone, and (d) melted region (Cu-strip thickness: 0.125mm, Cu-strip length: 50 mm, electric current density: 14.31kA/cm^2) 47

Figure 3.5 XRD patterns of the melted Cu strip in different regions; (a) rolled Cu, (b) oxidation region, (c) heat-affected zone, and (d) melted region (Cu-strip thickness: 0.125mm, Cu-strip length: 50 mm, electric current density: 14.31kA/cm^2) 48

Figure 3.6 Variation of the maximum deflection with time (strip thickness: 0.086 mm, strip length: 50 mm).......... 49

Figure 3.7 Variation of the maximum deflection of the Cu strips in the quasi-steady state period with electric current density.......... 49

Figure 3.8 Temporal variation of the electric resistance over the Cu strips of 50 mm in length and 0.085 mm, in thickness.......... 50

Figure 3.9 Dependence of the time-to-failure on electric current density................ 50

Figure 4.1 Typical indentation loading-unloading curves for the indentation of copper wires with the passing of an electric current; (a) J= 0 A/cm^2, and (b) J=25.5 kA/cm^2.. 62

Figure 4.2 Variation of the contact modulus with the contact depth for various current densities.. 63

Figure 4.3 Dependence of the contact modulus on electric current density for several indentation loads 63

Figure 4.4 Dependence of the indentation hardness on electric current density for several indentation loads 64

Figure 5.1 Temporal evolution of the surface temperature at the center of the Cu-strips for several current densities (*J*: electric current density).......................... 76

Figure 5.2 Dependence of the surface temperature rise on the electric current density 76

Figure 5.3 Typical indentation loading-unloading curves for the indentation of the Cu-strips with and without the passing of an electric current (J= 0 kA/cm^2, and J=4.88 kA/cm^2) 77

Figure 5.4 Variation of the contact depth on the electric current density for different indentation loads 77

Figure 5.5 Variation of the contact modulus with the indentation load for various current densities.. 78

Figure 5.6 Dependence of the contact modulus on the electric current density for several indentation loads 78

Figure 5.7 Dependence of the indentation hardness on the electric current density for several indentation loads 79

Figure 5.8 Variation of the indentation hardness with the contact depth for various current densities.. 79

Figure 5.9 Variation of the ratio of HS^2/F with the indentation load for various current densities.. 80

Figure 6.1 Temporal evolution of the surface temperature at the center of the Sn-strips for several current densities (*J*: electric current density).......................... 96

Figure 6.2 Dependence of the surface temperature rise on the electric current density 96

Figure 6.3 Load-displacement curves of the Sn-strips; a) without the pass of an electric current, and b) with the pass of an electric current of 4087.89 A/cm^2 .. 97

Figure 6.4 Variation of the contact depth with the electric current density for various indentation loads 98

Figure 6.5 Dependence of the contact modulus on the holding time for the indentation load of 100 μN and different electric current densities.................. 98

Figure 6.6 Variation of the contact modulus with the indentation load for various current densities.. 99

Figure 6.7 Dependence of the contact modulus on the electric current density for three indentation loads 99

Figure 6.8 Curve-fitting of the contact modulus as a function the electric current density for three indentation loads (J<4.09 kA/cm^2) 100

Figure 6.9 Dependence of the indentation hardness on the electric current density for various indentation loads 100

Figure 6.10 Variation of the indentation hardness with the contact depth for various current densities 101

Figure 7.1Temporal evolution of the surface temperature at the center of the Sn specimens at a chamber temperature of 373 K for different electric current densities 116

Figure 7.2 Dependence of the equilibrium surface temperature, T_e,on electric current density for several chamber temperatures 116

Figure 7.3 Time dependence of the tensile strain for several tensile stresses at a chamber temperature of 323 K and an electric current of 1.89 kA/cm^2........ 117

Figure 7.4 Time dependence of the tensile strain for several electrical current densities at a chamber temperature of 348 K and a tensile stress of 4.63 MPa 117

Figure 7.5 Effect of electromechanical interaction on the SEM micrographs of the polycrystalline tin specimens for ~4.7 hr; (a) J=0 A/cm^2, σ=0 MPa, and T=273 K, (b) J=0 A/cm^2, σ=0 MPa, and T=348 K,(c) J=0 A/cm^2, σ=0 MPa, and T=376 K, (d) J=0 A/cm^2, σ=3.08MPa, and T=348 K, and (e) J=2.52 kA/cm^2, σ=3.08MPa, and T=348 K,and (f) J=2.52 kA/cm^2, σ=3.08MPa, and T=348 K(titled angle: 80º) 118

Figure 7.6 Dependence of the steady state creep rate on the electric current density for several chamber temperatures (T_{cham}) under the action of a tensile stress of 3.09 MPa 118

Figure 7.7 Dependence of the steady state creep rate on the tensile stress with J= 0 kA/cm^2 for several chamber temperatures 119

Figure 7.8 Dependence of the steady state creep rate on the tensile stress at a chamber temperature of 323 K for several electric current densities............... 119

Figure 7.9 Stress dependence of the activation shear strain volume for different electric currents at a chamber temperature of 323 K 120

Figure 7.10 Temperature dependence of the steady state creep for several tensile stresses with $J = 0$ kA/cm^2 120

Figure 7.11 Temperature dependence of the steady state creep for several electric current densities under a tensile stress of 3.09 MPa 121

Chapter 1 Introduction

Metallic materials provide electrical, thermal, and mechanical functions for electronic devices and systems. Among those materials, copper has been used both as electronic interconnects and as electrical connectors due to its high electrical conductivity, low thermal expansion, high thermal conductivity, and good mechanical properties, and tin has been the basic component of soldering materials for the electronic industry due to its low melting point, mechanical properties, thermal conductivity, and manufacturability. With the development of electronics having electric interconnects of micron and submicron size, the passage of electric current of high current density has placed great challenges on understanding the effect of electric current on the mechanical behavior of these metallic materials.

With an electric current passing through metallic materials, local temperature rise due to Joule heating has been observed [1]. In an operating electronic device, the metallic materials used for electric interconnects have different designs and contact conditions, making it necessary to fully understand thermal conduction and the temperature distribution caused by the electric current. The increase in temperature as well as its distribution has a great effect on the mechanical response of metallic materials with the passage of an electric current of high current density.

With the temperature rise due to Joule heating, mechanical stresses can be generated in electric interconnects due to the difference in the coefficient of thermal expansion between electric components of electric devices and systems. Also, atomic mobility could be increased through the momentum exchange between high speed electrons and lattice atoms [2-4]. As a result, the physical behavior of metallic materials could be affected by the passage of an electric current, such as mechanical properties, electrical properties, thermal properties, microstructure, and surface morphology. These properties and behaviors play an important role in determining the performance and reliability of electronic devices and systems. This dissertation focuses on the effect of electric current on the deformation behavior of metallic materials, including electromechanical response, indentation deformation, and creep deformation.

Mechanical properties, such as hardness and modulus, are sensitive to temperature and microstructure [5, 6]. Electric current introduces not only local temperature rise due to Joule heating, but also the increase of atomic mobility due to the momentum exchange between high speed electrons and lattice atoms. Under certain conditions, the temperature change and/or the atomic mobility change could be the dominant factors influencing the mechanical behavior of metallic materials. A localized mechanical testing method, such as indentation technique, can be used to study the deformation behavior of metallic materials with the passage of an electric current [7]. The current effect on elastic modulus and hardness can be determined from the load and displacement data [8].

Under service conditions, external stress through contacting and internal stress caused by electric current could be continuously applied to metallic materials. Electric interconnects made of low melting materials will experience creep deformation and stress relaxation, even at room temperature. The creep deformation and stress relaxation could generate defects and damage. Then it is important to fully understand the creep behavior of metallic materials with the passage of an electric current.

It is difficult to use high density current in conventional creep tests due to large cross-section area of samples. There are reports about solder alloys whose creep rate increased with increasing DC electric current using double shear creep and impression creep techniques [9-13]. In this dissertation work, the tensile creep test technique is used to study the creep deformation of pure tin with the passage of an electric current. The coupled effect of electromechanical interaction is examined.

In this dissertation, Chapter 1 introduces the brief background and motivation. Chapter 2 is the literature review, giving the overview of previous research on the current induced deformation, indentation deformation, and creep deformation of copper and tin through which electric current passes. Chapter 3 studies the electromechanical response of copper with different electric current conditions. Chapter 4 reports the effect of a direct current (DC) on the indentation deformation of copper, including the Joule heating, the dependence of indentation hardness on the electric current, and the dependence of reduced contact modulus on the electric current. Chapter 5 addresses the effect of an

alternation current (AC) on the indentation deformation of copper. Chapter 6 focuses on the effect of a DC electric current on the indentation deformation of tin. Chapter 7 investigates the tensile creep of tin with the passage of a DC electric current. The steady state creep rate, the stress exponent, and the activation energy are examined for different electric current conditions. Chapter 8 is the summary of the dissertation work and the future research opportunities.

Chapter 2 Literature review

2.1 Metallic materials

Metallic materials have been used for electronic devices and systems from the very beginning of the electronic industry in the 19th century. They provide electrical conductivity, mechanical support, thermal conductivity, and signal connection among all types of components in the electronic devices and systems. With the development of today's electronics, the metallic materials used are required to have high energy efficiency with micron and submicron size. As a result, the metallic materials are subjected to the action of high current density. The understanding of the deformation behavior of metallic materials with the passage of high density electric current plays a curial role in determining the performance and reliability of electronic devices and systems.

Copper is one of the most important metallic materials, which has been used by human being for thousands years, since the Copper Age. Pure copper has a very high electrical conductivity of 59.6×10^6 S/m, and the second highest thermal conductivity among pure metals. It has a melting temperature of 1083 °C. Currently, copper is the preferred material for the electronic interconnects because of its low resistivity, low RC (Resistance capacitance) delay and good manufacturability [14, 15].

Tin is another important metallic material for electronic devices and systems. The use of tin can be dated to the Bronze Age around 3000 BC, when it was mined and incorporated with copper to make bronze. It has a melting temperature of 231°C. Tin has three allotropic structures, α the gray diamond cubic tin, β the white tetragonal tin and γ the rhombic tin [16].

In electronic devices and systems, tin has been used as the basic component for soldering materials due to its low melting temperature, solderability, thermal properties, electrical properties, and thermal-mechanical properties. Many tin-based alloys have been developed as soldering materials such as Sn-Pb, Sn-Zn, Sn-Cu, Sn-Ag, Sn-Bi, Sn-In, etc. Among these, Sn-Pb eutectic solder alloy has been used as the interconnect material for a

long time in most electronic circuits [17] such as printed circuit board (PCB), ball grid array (BGA), flip chip, surface mount techniques (SMT), etc. Due to the hazard of lead contamination to human health, lead-free solders have been developed in the last few decades. Most electronic devices have been designed based on the properties of Sn-Pb eutectic alloy. This gives us the primary alloy design criteria for lead-free soldering materials such as melting temperature, solderability, thermal properties, electrical properties, and thermal-mechanical properties. Generally, all these properties are required to be comparable to those of Sn-Pb eutectic solder, since current electronic assembly devices are designed based on the behavior of Sn-Pb solder [18]. In addition, the cost to make the alloy needs to be considered. Among all those substitutes, Sn-based lead-free solder materials have been considered as the leading potential candidates [19]. But these binary Pb-free solders cannot satisfy the property requirements for application, so ternary and even quaternary Pb-free solders have been developed by adding other elements to improve the performance [19, 20].

When these materials are used for electronic devices and systems, external force might be applied to them through mechanical contact. As a result, mechanical stress and strain could be generated in these metallic materials. Under working conditions, an electric current could be passed through these materials. The high speed electrons will interact with the lattice atoms in the metallic materials, leading to Joule heat and momentum exchange. Temperature rise is generated due to the Joule heating, causing thermal expansion. Due to the difference of the thermal expansion coefficients of different structural contacting components, metallic materials will experience additional force under the action of an electric current. Mechanical deformation of metallic materials could be observed under the initial contacting force and additional force generated by the electric current. These induced-combined stresses could be in different forms such as tension, compression, and shear stresses. In some cases, the metallic materials, such as soldering materials, might serve under stresses at temperatures higher than the half melting points, leading to the creep deformation of these materials. To evaluate structural reliability and improve device performance, understanding the

mechanical deformation of metallic materials with the passage of an electric current is crucial for their applications in electronic devices and systems.

2.2 Current effect

2.2.1 Joule heating

When an electric current passes through an electronic interconnect, Joule heat is released leading to local temperature rise [1]. Since most of solder alloys have low melting points, these soldering materials could experience creep deformation and stress relaxation. The temperature rise under working conditions will play an important factor in determining the mechanical behavior of solder joints. From a macro scale, the Joule heat can be expressed as

$$Q = I^2 Rt = j^2 \rho Vt \tag{2.1}$$

where Q is the heat generated by Joule heating, I is electric current, R is resistance, t is time, j is electric current density, ρ is electrical resistivity and V is volume. From a micro scale, the Joule heat can be expressed as

$$\frac{dT}{dt} = \frac{s\left|\nabla \phi\right|^2}{\rho c} \tag{2.2}$$

where T is the temperature, s is the electric conductivity, ϕ is the potential of the electric field, ρ is the density of the materials, and c is the specific heat of the materials.

The current induced heat conduction can be described as [21]

$$\rho_d c \frac{\partial T}{\partial t} = \lambda \nabla^2 T + \rho j^2 \tag{2.3}$$

here ρ_d is density, c is specific heat, λ is thermal conductivity, and T is temperature. The temperature gradient could be generated in materials. However, the thermal conduction is controlled by the contacting condition and the shape and size of metallic materials. The

electrocontact heating depends on the electric properties and the interface between different components. The change of temperature distribution due to Joule heating in the contacting interface, in turn, influences the evolution of temperature in the materials.

2.2.2 Electromigration

There are interactions due to phonon vibration between the moving electrons and lattice atoms when an electric current passes through the metallic materials, leading to energy and momentum exchange. With low electric current density, the scattering interaction does not activate the atoms out of their equilibrium positions, and therefore, there is no atom displacement and mass transportation. However, atom movement and mass transportation can be caused by the scattering interaction when the electric current density is high enough, generally above 10^4 A/cm^2 [22]. Atom movement and mass transportation caused by an electric current is called electromigration. During electromigration, atoms are transferred from the cathode to the anode, causing tension in the cathode and compression in the anode. According to the Nabarro-Herring model of equilibrium vacancy concentration in a stressed solid [23], there is a vacancy concentration gradient across the material from the cathode region to the anode region. This concentration gradient might induce atomic flow from anode to the cathode. This atomic flow moves opposite of the electromigration direction. The electrical force acting on the diffusing atom F_{em} combining electrical and mechanical forces can be expressed as [24]

$$F_{em} = Z^{*}eE = (Z_{el}^{*} + Z_{wd}^{*})eE \tag{2.4}$$

Here e is the electron charge, E is the electric field intensity, and Z^{*} is the effective change number if the charge carriers, Z_{el}^{*} can be regarded as the nominal valence of the diffusing ion in the material when the dynamic screening effect is ignored, responsible for the field effect, and $Z_{el}^{*}eE$ is the direct force. Z_{wd}^{*} can be treated as the charge number representing the momentum exchange effect, and $Z_{wd}^{*}eE$ is the electron wind force. For metallic materials as a good conductor, the electron wind force is much greater that the

direct force for electromigration. The mechanical force can be regarded as the gradient of the chemical potential in a stressed solid

$$F_{em} = -\nabla \mu = -\frac{d\sigma\Omega}{dx} \tag{2.5}$$

Here is μ the chemical potential, σ is the hydrostatic stress in the metal, and Ω is the atomic volume. Thus, the phenomenological equations for atomic and electron fluxes can be expressed as

$$J_{em} = -C\frac{D}{kT}\frac{d\sigma\Omega}{dx} + C\frac{D}{kT}Z^{*}e\xi j \tag{2.6}$$

$$J_{e} = -L_{21}\frac{d\sigma\Omega}{dx} + n\mu_{e}e\xi j \tag{2.7}$$

Here J_{em} is the atomic flux, J_{e} is electron flux, C is the concentration of atoms, n is the concentration of conduction electrons, ξ is the resistivity, j is the current density, D/kT is atomic mobility, μ_{e} is the electric mobility, and L_{21} is the phenomenological coefficient of irreversible processes containing the deformation potential.

If there is no electromigration flux, then we can take J_{em}=0. In that case, a critical length, for which a steady state without electromigration flux, can be obtained

$$\Delta x = \frac{\Delta\sigma\Omega}{Z^{*}e\xi j} \tag{2.8}$$

This critical product can be a very important parameter to be considered in designing electrical devices and systems containing metallic materials that have electromigration during service.

With high density electric current, electromigration leads to atoms moving to the anode side and voids forming on the cathode side. Over time, the hillock and void formation resulting from accumulation of atoms and vacancies could lead to short and

open failures [25]. The mean time to failure (MTTF), which was proposed by Black [26], can be expressed as

$$MTTF = A\frac{1}{j^{n_b}}\exp(\frac{Q}{kT}) \tag{2.9}$$

Where A is a constant, j is the electric current density, n_b is a constant, Q is the activation energy, and k is the Boltzmann's constant. The MTTF is an important parameter to understand the performance and reliability of electronics.

2.3 Microstructure evolution

The temperature rise due to Joule heating and the atom mobility increase due to the momentum exchange between the high speed electrons and the lattice atoms have been the pathways for electric current to transfer energy to metallic materials. As temperature increases, the microstructure damage of metallic materials, such as grain size, might occur. Also, electromigration could induce the flow of atoms and vacancies inside the materials, which results in the change of microstructure. The combined effect of Joule heat and electromigration due to the passage of an electric current likely introduces grain size and orientation change for pure Cu and Sn, and causes the whisker growth in pure Sn.

Conrad et al [27, 28] found that direct current, during the annealing of copper, enhanced recrystallization and grain growth and retarded the formation of annealing twins. They proposed that the higher mobility of dislocations produced by the electric current is in part responsible for these effects.

Kuo and Lin [29] observed the recrystallization of dispersed Zn second phases in Sn–9Zn alloy. The Zn polycrystal of aged Sn–9Zn alloy recrystallizes under the action of electromigration to form a thin prism sheet crystal of basal plane unit with (0001) preferred orientation. They suggested that the higher growth rate of the incoherent interface rather than that of the coherent interface would result in the formation of thin prism sheet crystals dispersed in the Sn matrix.

Chen et al [30] studied the failure mechanism of lead-free solder interconnections of the chip-scale package–sized Ball Grid Array. They found that the failure of the interconnections was associated with the change of microstructures by the recrystallization in the strain concentration regions of the solder interconnections.

Wu et al [31] discussed the grain rotation and growth in beta Sn under constant current electromigration. They suggested that the direction change of grains with different electric resistance caused the resistance drop. The mechanism of the grain growth and grain rotation was proposed and discussed. Wu et al [32] studied the grain rotation in anisotropic beta Sn induced by electromigration. They suggested that the anisotropic resistivity caused the divergence of the vacancy fluxes at the grain boundary and induced vacancy gradients. They assumed that the vacancy gradient along the grain boundaries is proportional to the stress gradients. The stress along the grain boundary generates a torque leading to the grain rotation.

The whisker growth is another important issue in microelectronics, which can be observed even at room temperature [33-36]. A whisker is the single crystalline filament eruption from the metal surface. Compressive stress is recognized as the driving force for tin whisker formation [37]. Many pathways could induce compressive stress in the Sn interconnects: residual stress from manufacturing, contact force between different components, and the stress due to thermal mismatch between different components. The tin whisker growth has been studied under different conditions, such as applied external compressive stress [38, 39] and thermal conditions [40, 41]. It was found that whisker growth has a nucleation period, a growth period, and a saturation period [42].

The Sn whisker growth has been studied under the action of an electric current. Liu et al [43] investigated the whisker growth of Sn at an electric current density of 10^5 A/cm^2 near ambient temperature. They found that Sn whisker grew with current stressing time and was driven by a compressive stress.

Liu et al [33] studied the tin whisker growth in pure Sn using Blech structure. They found that the average growth rate increased as the testing temperature increased and as

the electric current density increased. They suggested that the whisker grew on where the crack driven by the compressive stress from electron flow to break the localized weak spots on Sn oxide layer on the anode side.

Kim et al [44] investigated the growth of Sn whisker for pure Sn-plated lead frames. They found longer whiskers for higher electric current levels than low electric current levels at the same temperature. They also studied the effect of the surface oxidization on the growth of Sn whiskers.

2.4 Current induced deformation

The volume or dimensions of substances changes with temperature because of the change of the equilibrium distance among atoms. As temperature increases, the interaction energy increases, leading to the increase of the equilibrium distance among atoms. With the passage of an electric current, thermal expansion is induced due to Joule heating. Also, atomic mobility could be increased through the momentum exchange between atoms and high-speed electrons [2, 3, 45]. As a result, the equilibrium distance might be changed due to the increased atomic mobility. For bulk materials, this effect is negligible compared with the materials size. However, for solder alloys in the micro or nano-scales, the change in the equilibrium position caused by electric current could be detected, when the current density is high enough.

Over time, electromigration occurs in metallic materials with the passage of an electric current. Under the combined effect of the thermomigration and electromigration, large plastic deformation might occur. For electronic interconnects, the plastic deformation induced by long time current stressing could cause failure of electronics, which is very important to understand the reliability of electronic devices and systems.

Ye et al [46, 47] investigated the deformation of lead-free solder joint under electric current stressing. They observed large deformation when the current density was as high as 10^4 A/cm^2. They suggested that the deformation was due to the electromigration in the solder joints and the deformation generated by high current density was irreversible. During the deformation, the movement of vacancies and atoms in the solder joint caused

the permanent deformation. They used finite element method to simulate the deformation. From the experimental and simulation results, they found that the current density distribution within the solder joint also had effect on the deformation behavior, in addition to the current density level.

Chen et al [48] studied the failure induced by current stressing in Pb-free SnAg solder joints under 9.7 kA/cm^2 at 150 °C. They found void formation in the powered bumps, regardless the direction of the current flow. They suggested that the driving force of the Cu diffusion is the large thermal gradient accredited to Joule heating across the solder bumps. The thermomigration force was thought to be larger than the electromigration force tested in their study.

Ryu et al [49] studied the effects of texture and grain structure on the electromigration lifetime of Cu interconnects. They found that the electromigration lifetime of (111) Cu interconnect is much longer than that of (200) Cu interconnect. They also observed a current density exponent of 2 for the time-to-failure at 473 K.

Michael et al [14] presented two different electromigration failure mechanisms for the Cu interconnects with SiN or SiCN passivation. They found that the failure mechanism was dependent on the interface condition of the capping layer. Their results suggested that the failure mechanisms could be either interface eletromigration or grain boundary electromigration.

Shao et al [15] investigated the electromigration in dual damascene Cu interconnects using package level electromigration tests and failure analysis techniques. When subjected to a current density of 1.2 MA/cm^2 at 573 K, they found that the interface diffusion along the Cu/Si_3N_4 interface was the dominant electromigration path. They also noted that the increasing reservoir length could improve the electromigration failure time, which was consistent with the mechanism of vacancy movement along the Cu/Si_3N_4 interface.

Wei et al [50] studied the electrtomigration in a Cu/low-k interconnect at either an electric current density of 1.25 or 4.0 MA/cm^2. They observed void formation at the cathode end of the sample and hillock formation at the anode end. They discussed the critical stress required for extrusion formation.

Cheng et al [51] studied the effect of metal line width on electromigration in Cu interconnects. They found that the electromigration time to failure increased as the line width for long metal lines increased. However, the electromigration time to failure decreased as the line width for short metal lines increased.

Budiman et al. [52] studied the electromigration in damascene Cu interconnect using an in situ technique with an electric current of 3.1 MA/cm^2 at 300 °C for the wide samples and with an electric current of 3.3 MA/cm^2 at 360 °C for the narrow samples. They found plastic deformation caused by electromigration even before the onset of visible microstructure evolution. Budiman et al [53] investigated the electromigration induced plastic deformation in Cu interconnects with an electric current of 2 MA/cm^2 at temperature of 300 °C. They found plastic deformation in the Cu interconnects with electromigration with preliminary evidence of a texture correlation. They observed that the extent of plastic deformation was larger in lines with strong (111) textures than that of weaker textures. They thought that strong (111) texture leads to high preference of <112> direction along the length of the line, and this subsequently leads to a higher tendency for the grains to behave plastically in response to EM stressing. They also the MTTF of Cu interconnects with various electric current density from 0.5 to 9.5 MA/cm^2 at temperature of 350 °C [54].

Zhang et al [55] studied the local melting of damascene Cu conductor lines at temperature of 300 °C and 350 °C with electric current densities in the range of 0.6×10^6 to 1.6×10^6 A/cm^2. They found that the resistance increase due to the formation and growth of voids in the conductor line. However, the resistance could decrease due to the local melting of Cu. There are combining effect of the void formation and local melting in the conductor lines on the resistance evolution during the passage of electric current.

Zhang et al [56] investigated the electromigration induced strain relaxation in Cu conductor lines with a passivation layer. After current stressing for 120 h with an electric current of 2.2×105 A/cm^2 at 270°C, they observed strain relaxation and homogenization occurring in the Cu lines.

2.5 Indentation

Indentation technique is an advanced method to characterize the mechanical properties of materials by contacting two materials under designed force conditions. The mechanical properties can be directly measured from the indentation load and displacement monitored by the high resolution testing facilitates [7]. Elastic modulus, hardness, and fracture toughness can be calculated from the load and displacement data [8]. Among these parameters, hardness and elastic modulus are the initial concern for the instrumented indentation, which was developed in 1992 [57, 58]. Due to its capabilities of characterizing the mechanical properties of thin films and small-scale materials, instrumented nanoindentation has been used as one of the most important mechanical characterization techniques, especially on the micro- and nano-scale [57].

Many works have been done to improve the testing equipment and analyzing method for nanoindentation tests. Among these, the Oliver-Pharr model has been the most widely used method to determine the mechanical properties. This model is based on the method proposed by Doerner and Nix who approximated the unloading curves as the elastic indentation of a semi-infinite elastic material by a rigid indenter of flat-end [59].

Oliver and Pharr [57, 60] approximated the unloading curves by a power law relation as

$$P = \alpha(h - h_f)^m \tag{2.10}$$

Where P is the indentation load and h is the indenter displacement, h_f is the final indentation depth, α and m are the power-law fitting constants. Here m=1 is for the flat-end indenter and m=1.5 for a parabolic indenter. The contact area of an indentation is

calculated as a function of indentation depth, which is calibrated by independent measurements. The hardness is measured as

$$P = \frac{P_{\max}}{A} \tag{2.11}$$

and the contact modulus can be calculated through the relation

$$E_{eff} = \frac{\sqrt{\pi} S}{2\beta\sqrt{A}} \tag{2.12}$$

$$S = \frac{dP}{dh}\bigg|_{unloading} \tag{2.13}$$

The contact modulus is defined as

$$\frac{1}{E_{eff}} = \frac{1-\nu^2}{E} + \frac{1-\nu_i^2}{E_i} \tag{2.14}$$

Here P_{max} is the peak indentation load, A is the projected area of the hardness impression, S is the measured stiffness of the upper portion of the unloading curve, E and ν are Young's modulus and Poisson's ratio for the specimen and E_i and ν_i are the same parameters for the indenter.

During the loading phase, a pop-in phenomenon may be observed from the load-displacement curves following the elastic loading for some metallic materials. It has been proposed that these discontinuities are due to the onset of dislocation nucleation [57, 61-65]. The first pop-in occurs at an constant indentation load, at which the maximum shear stress at the tip of the indenter reaches the theoretical shear strength of materials [66].

Due to the plastic deformation during indentation, materials may pile up around the indenter. It was observed that the change of contact area caused by the pile-up could be as high as 50% [67]. The pile-up of materials depends on the ratio of effective modulus to yield stress and the work hardening behavior, and it likely causes the error in measuring

the contact modulus and hardness. The pile-up is greater for larger ratios of effective modulus to yield stress [60].

With the development of nanoindentation, many researchers have worked on the nanoindentation of materials not only at room temperature but also at high or elevated temperatures, due to the consideration of work environment of materials. High temperature has an obvious influence on the testing and analysis of nanoindentation. Heat management, thermal drift, and surface oxidation are the problems which needed to be addressed when conducting nanoindentation tests at high temperature [68]. Stable temperature and minimal thermal drift are required to reduce the effect of temperature on the displacement during indentation [68]. Several studies have been conducted on the high temperature nanoindentation of different materials; and improvements have been made on both instrument and analyzing methods. Nowadays, the modified nanoindentation systems containing temperature controlling components can be used at a wide temperature range from -10°C up to 750°C [68].

Thermal drift is caused by the temperature change between indenter tip and specimen. To obtain the real indentation load and displacement data, temperature fluctuations must be avoided during tests. Although an artificial drift displacement caused by a temperature change of 1K was observed to be as high as 100 nm during setup, acceptable drift rates could satisfy experimental requirement with enough equilibrium time [69]. Generally, the thermal equilibrium between tip and specimen can be reached in contact with the sample under the preset force at the thermal-equilibrium temperature for 1 hour. Also, the tip is required to be in contact with the specimen surface during the test to avoid extra thermal drift [70-75].

Oxidation is another important issue for nanoindentation at high temperatures. The oxidation layer could influence the response of materials during indentation, especially when nanoindentation is carried out in the sub-micro-scale. Special technique has been developed to reduce the effect of oxidation. Volinsky et al. introduced an oxidation-proof coating of a very thin platinum layer to prevent surface oxidation of copper for nanoindentation at 130°C [76]. At higher temperatures, the oxidation of the indenter is

also considered, not only the oxidation of the sample surface. In this case, a diamond or sapphire tip needs to be used [68].

Most tests conducted have been focused on the influence of temperature on the mechanical properties measured by nanoindentation. When passing an electric current through electric interconnect, the mechanical behavior of solder alloys will change not only due to the temperature rise, but also due to the momentum exchange. As a result, the mechanical properties measured from nanoindentation might represent the combined effect of the temperature rise and the momentum exchange.

There is little reported research about the instant effect of an electric current on the indentation of metallic materials. Gilman [77] studied the effects of a small electric current on the indentation hardness of a semiconductor. He found that the indentation hardness decreased as the electric current density increased. He suggested that the charged surface states introduced surface dipole layers, and modified the local energy band gaps which affect the local dislocation mobilities, and in turn affected the indentation hardness.

2.6 Creep deformation

Creep is the time-dependent plastic deformation of materials. It is one of the most important mechanical properties of materials at high temperatures. Metal creeps under the action of stress at temperatures higher than one-half of the absolute melting temperature [78]. The characteristic curves for tensile creep are usually divided into three stages: primary creep, steady state creep, and tertiary creep [78]. However, not all tests have the three stages; some materials only have the primary creep stage. Among these three stages, the steady state creep stage is the most important, since the strain rate used to characterize the creep behavior refers to the rate in this stage. The steady state creep can be described by the Dorn equation [79]

$$\dot{\varepsilon}_s = \frac{AGb}{kT} D_0 \exp(-Q_c / RT)(\frac{b}{d})^p (\frac{\sigma}{G})^n \tag{2.15}$$

where $\dot{\varepsilon}_s$ is the steady state creep strain rate, A is a dimensionless constant, D_0 is the frequency factor, G is the shear modulus, b is the Burgers vector, k is the Boltzmann's constant, T is the absolute temperature, σ is the stress, d is the grain size, p is the inverse grain size exponent, n is the stress exponent, Q_c is the activation energy, and R is the gas constant. Stress exponent and activation energy are related to specific dominant creep mechanism. From the equation, it can be seen that the steady state creep rate is dependent on applied stress, temperature, activation energy, grain size, and shear modulus. The steady state creep rate will increase with decreasing grain size, increasing applied stress, or increasing service temperature during the creep lifetime [80].

Several techniques have been used to characterize the creep behavior of materials, including tensile creep, compressive creep, impression creep, indentation creep and torsional creep [16, 81-83].

2.6.1 Tensile creep

Murty et al. [84] studied the tensile creep of Sn5%Sb for various strain-rates and temperatures. During the tensile tests, a maximum ductility of about 350% was noted at ambient temperature. The stress exponents were about 3 and 5 at low and high stresses, respectively, and the activation energy was about 54.4 kJ/mol. They compared the results with those from automated ball indentation tests and they found that the results were in good agreement.

Mavoori et al. [85] compared the creep behavior of two eutectic lead-free solders (96.5Sn-3.5Ag and 91Sn-9Zn) using conventional creep and stress relaxation tests. The creep tests were conducted in load-control model with initial stresses in the range of 10-22 MPa at two temperatures, 25 and 80 °C. They found that the stress exponents were 11.3 and 5.7, the activation energies were around 80.8 and 66.6 kJ/mol, for 96.5Sn-3.5Ag and 91Sn-9Zn, respectively. The activation energies obtained from the tensile creep tests were close to those for self diffusion of pure lead and tin, suggesting that the creep process were dominated by dislocation climb. They also performed stress relaxation tests under constant-strain conditions with strains in the range of 0.3-2.4% and temperature at

25°C and 80°C. They obtained the stress exponent of 6 and 4.2, and the activation energies of 33.5 and 106.9 kJ/mol, for 96.5Sn-3.5Ag and 91Sn-9Zn, respectively.

McCabe and Fine [86] investigated the creep behavior of tin-antimony and tin-indium-antimony alloys using tensile creep method. They found that the formation of intermetallic SbSn and InSn provided a significant composite strengthening effect which was relatively unaffected by aging at temperatures below 100 °C. They suggested that even better creep resistance could be achieved in alloys containing distributions of both InSb particles and SbSn whiskers.

Shohji et al. [87] studied the creep behavior of Sn-8Zn-3Bi alloy using tensile creep at temperatures of 298, 348, and 398 K. They observed that the minimum strain rate had a linear relationship with the applied stress for high stresses. The stress exponents were 9.3, 7, and 4 at 298, 348, and 398 K, respectively.

Mathew et al. [88] studied the creep properties of Sn, Sn-3.5Ag and Sn-5Sb solder alloy at temperatures ranging from 296 to 473 K. They found that the stress exponents were 7.6, 5.0 and 5.0, and the activation energies were 60.3, 60.7, and 44.7 kJ/mol for Sn, Sn-3.5Ag and Sn-5Sb respectively. Based on the results, they suggested that the creep was controlled by dislocation climb through lattice diffusion in pure tin and Sn-3.5Ag alloy, but by viscous glide through dislocation pipe diffusion in Sn-5Sb alloy.

Zhu et al. [89] investigated the creep behavior of Sn96.5Ag3Cu0.5 solder using tensile tests. They observed a long time creep fracture at room temperature of 25 °C and low stress of 20 MPa. At an elevated temperature of 100 °C, the creep rupture time was short even under a constant creep stress of 15 MPa.

Zhang et al. [90] studied the eutectic 80Au/20Sn solder alloy using tensile creep at temperature of 25, 75 and 125 °C. They obtained a stress exponent of 2.07 and an activation energy of 102 kJ/mol, suggesting that the grain boundary sliding might be the dominant creep mechanism. The 80Au/20Sn alloy has the typical creep deformation

characteristics. The creep strain increased and creep lifetime decreased with the improved applied stress level and temperature.

Che et al. [80] conducted the tensile creep of Sn-1.0Ag-0.5Cu-0.02Ni solder in the stress range of 5-45 MPa at temperatures of -35 °C, 25 °C, 75 °C, and 125 °C. They obtained stress exponents of 6.1 for low stress and 12.8 for high stress at 25 °C, and 5.0 for low stress and 10.8 for high stress at 125 °C. The activation energy calculated was 58.4 kJ/mol. Different stress exponents represented different creep mechanisms.

2.6.2 Compression creep

Vianco et al. [91, 92] studied the creep deformation of ternary 95.5Sn-3.9Ag-0.6Cu solder using compression creep tests for as-casted and aged alloys with compressive stress varying from 2 to 45 MPa and temperature ranging from -25 °C to 160 °C. For as-casted solder, they obtained stress exponent of 4.4 and activation energy of 25 kJ/mol for temperature less than 75 °C and stress exponent of 5.2 and activation energy of 95 kJ/mol for temperature over 75 °C. They suggested that the rate mechanism was short-circuit diffusion creep at low temperatures and lattice diffusion creep at high temperatures. For aged alloy, they obtained stress exponent of 5.3 and activation energy of 49 kJ/mol for all the temperatures. The result suggested that lattice diffusion dominated at high temperatures.

Vianco et al. [93] investigated the creep behavior of 97In-3Ag, 58In-42Sn solders and their counterparts 80In-15Pb-5Ag, 70In-15Sn-9.6Pb-5.4Cd solders at temperature of -25, 25, 75, 100, and 125 °C. They performed the tests for both as-fabricated and post-annealed conditions. They found that the activation energies were 99 and 46 kJ/mol for as-fabricated and post-annealed conditions for In-Ag alloy, respectively, which suggested that lattice diffusion creep dominated for as-fabricated conditions and fast-diffusion creep dominated for post-annealed conditions. The activation energies for In-Sn alloy were 55 and 48 kJ/mol for as-fabricated and post-annealed conditions for In-Ag alloy, which suggested that fast-diffusion creep dominated for both conditions.

Park et al. [94] studied the creep behavior of pure polycrystalline Sn by compression creep test and impression creep test. They obtained stress exponent of 5 and activation energy of 52 kJ/mol from both testing methods.

Lopez et al. [95] used compression test to study the deformation behavior of Sn-Ag-Cu alloy with strain rates of 4.2×10^{-5} s^{-1} and 8.3×10^{-4} s^{-1} at temperatures of -25, 25, 75, and 125 °C. They found that the work-hardening diminished with increasing temperature. The aging treatment had a small effect on the stress-strain curves.

2.6.3 Shear creep

Fang et al. [96] studied the creep behavior of a Pb-9Sn solid solution alloy for temperatures ranging from 489 to 539 K and stresses ranging from 3×10^{-6} to 4×10^{-5} G, using double-shear type specimens. The stress exponent was 5 at low stress region and 3.5 at intermediate stress region. For low stresses, the creep was dominated by dislocation climb. Also, they found that there was a transition from metal behavior at low stresses to alloy behavior at high stresses.

Murty [97] investigated the creep behavior of Pb-9Sn alloy using double shear creep method. They found that the stress exponent was unity at low stresses and increased with stress at high stresses. The activation energies were 21.15±3.67 kcal/mol and 25.01±1.16 kcal/mol at low and high stress ranges, respectively. The activation energy in high stress range was close to that for self diffusion in pure lead.

Alizadeh et al. [98] used the shear punch creep test method to study the creep properties of Sn-5Sb alloy under the punch stress in the range of 8-26 MPa and the temperature in the range of 298-370 K. They also carried out conventional creep tests with stress in the range of 7-21 MPa for comparison. The stress exponents decreased from 4.7 at 298 K to 3.6 at 370 K for the shear punch creep and from 4.6 at 298 K to 3.6 at 370 K for the conventional creep. The activation energies were 37.5 kJ/mol and 39.0 kJ/mol obtained from the shear punch creep and tensile creep tests, respectively.

2.6.4 Impression creep

Chu and Li [81] introduced the impression creep technique to avoid the problems in conventional creep tests, such as sample preparation and multiple samples. A flat-end cylindrical indenter was pressed into the sample with a constant load to reach a steady state creep. They found that the steady state impression velocity was a power function of the applied stress, which can be used to calculate the stress exponent. In addition, the activation energy can be calculated from the relationship between the impression velocity and reciprocal of absolute temperature. The stress exponent and activation energy obtained were comparable with those from conventional creep tests. They analyzed the possible creep mechanisms, including bulk diffusion, interface diffusion between the indenter and the specimen, and dislocation motion. Based on this method, many soldering materials have been examined by the impression creep test under wide stress range at various temperatures.

Chu and Li [99] conducted the impression creep tests of β-tin with the punching stress ranging from 7.53 to 47.7 MPa, and temperature ranging from 313 to 481 K, for different crystal orientations. They found that the creep mechanisms were different at low and high temperatures. At high temperature, the activation energy was 104.7– 108.9 kJ/mol independent of the punching stress. At low temperature, the activation energy was stress dependent, which was 34.3 kJ/mol for the [001] orientation in the stress range of 16-20 MPa, 41.9 kJ/mol for [100] at 12-16 MPa, and 39.4 kJ/mol for [110] at 16-20 MPa. The stress exponent was in the range of 3.6 to 5.0 for all testing conditions. They suggested that the creep deformation was controlled by dislocation slip at low temperature and dislocation climb at high temperature.

Juhasz et al. [100] studied the superplasticity of the Pb-Sn eutectic alloy using the impression creep test. The stress exponents were about 2.5 at low strain rate and about 5 at high strain rate. The activation enthalpy was found to be a function of the punching stress with a value of 60 kJ/mol extrapolated to zero stress. These results were equivalent to those obtained from tensile tests [101].

Yang and Li [102] carried out the impression creep tests of a 63Sn-37Pb eutectic alloy under stress ranging from 1.5 to 47 MPa and temperature ranging from 25 to 110 °C. They found that the stress exponents increased with increasing temperature. The exponents were 1 to 3.5 at temperature ranging from 80 to 110°C and 2.5 to 6 at temperature ranging from 25 to 65 °C, respectively. They used a hyperbolic sine function to describe the creep deformation for all stresses and temperatures in their work. The activation energy with a value of 55 kJ/mol was obtained from the result.

Shettigar and Rao [103] used the impression creep method to study the creep behavior of the Pb-Sn eutectic alloy of two different grain sizes, 3.4 and 7.5 μm in the temperature range of 30-125 °C. They confirmed the attractive application of the impression creep test method for the creep study of small volume material.

Balani and Yang [104] conducted the impression creep of 90Pb-10Sn alloy in the temperature range of 298-393 K and the punching stress range of 17.1-102.8 MPa. The stress exponent of 4.3 was calculated from the results. They found that the impression velocity and the punch diameter had a linear relationship, which was in agreement with the numerical simulation reported in the literature. The creep mechanism was the interfacial sliding between two phases.

Rani and Murthy [105] investigated the creep behavior of eutectic Sn-3.5Ag, Sn-0.7Cu and Sn-9Zn solder alloys in the stress range of 21 to 148 MPa and the temperature range of 303 to 439 K. A linear relationship between the impression velocity and the punch diameter was found. The stress exponents were in the range of 3.5 to 6.5 for all three materials. The activation enthalpies were 41 kJ/mol for Sn-3.5Ag and were 52 and 74 kJ/mol for Sn-0.7Cu and Sn-9Zn, respectively. From the values of stress exponents and activation enthalpies, they suggested that the creep was controlled by dislocation climb during the tests.

Dutta et al. [106] studied the creep behavior of Sn-3.5Ag solders using impression creep. For the as-reflowed alloy, the stress exponent was about 3 at low stress. At high stress, the stress exponent was about 6.5 and the activation energy was close to that of

dislocation pipe diffusion in pure Sn. For the aging alloy, the stress exponent was found to be 4.4 at low stresses. They suggested that the change of the dissolved solute concentration caused by aging led to the dislocation climb mechanism in the low stress region.

Mahmudi et al. [107] used the impression method to investigate the creep behavior of Sn-5Sb lead free solder for the punching stress in the range of 18 to 135 MPa at temperature in the range of 298 to 403 K. For wrought material, the stress exponent was 2.8 and the activation energy was 41.3 kJ/mol, which was very close to the activation energy for grain boundary diffusion of β-Sn. For the cast alloy, the exponents were 5.4 and 11.4 and the activation energies were 53.8 and 75.8 kJ/mol for low and high stresses, respectively. At low stress region, the activation energy was 53.8 kJ/mol.

Mahmudi et al. [108] studied the creep behavior of the hypoeutectic Sn-Zn alloys and compared to that of the eutectic Sn-9Zn alloy. The punching stress was in the range of 50-110 MPa and the temperature was in the range of 298-370 K. They obtained the average stress exponents of 6.2, 6.4, 7.3, and 7.4 and the activation energies of 41.9, 43.9, 44.5 and 46.0 kJ/mol for Sn-2.5Zn, Sn-4.5Zn, Sn-6.5Zn and Sn-9Zn, respectively. The values of activation energies were close to 46 kJ/mol for dislocation climb in pure Sn. They suggested that the operative creep mechanism was dislocation climb controlled by dislocation pipe diffusion. The higher volume fraction of Zn-rich second phase precipitates in the more concentrated alloys was the main strengthening mechanism in these Sn-Zn alloy systems.

Mahmudi et al. [109] carried out the impression creep of Sn-Zn based alloy with addition of rare earth elements for stress in the range of 40 to 135 MPa and temperature in the range of 298 to 420 K. They found that the addition of rare earth element could improve the creep resistance of Sn-Zn alloy. The mean stress exponents were 6.8, 6.9, 7.1, 6.8 and the activation energies were 42.6, 40.6, 43.0 and 44.9 kJ/mol for Sn-9Zn, Sn-9Zn-0.1RE, Sn-9Zn-0.25RE, and Sn-9Zn-0.5RE, respectively. These results suggested that the creep was dominated by dislocation climb controlled by dislocation pipe diffusion.

Park et al. [94] compared the impression creep and compression creep of polycrystalline β-tin in the temperature range of 323–423 K. They found that the creep parameters determined from the impression and compression creep were identical. The stress exponent was about 5 and the activation energy was about 42 kJ/mol.

2.6.5 Indentation creep

The depth sensing indentation can also be used to characterize the viscoplastic behavior of materials. The load and displacement curves during indentation can be used to determine the creep properties. Temperature is one of the most important variables for creep tests. The thermal fluctuations caused by temperature change can lead to error during the test. As a result, special care must be made to reduce the effect of thermal fluctuation during indentation creep tests.

Juhasz et al. [101] used indentation to study the creep properties of Pb-Sn eutectic alloy at temperature in the range of 251 to 318 K. They obtained the stress exponents of 2.0 to 2.4 under various testing loads and the activation energy of 53 kJ/mol. Their results were in good agreement with the results reported in the literature.

Fujiwara and Hirokawa [110] studied the creep properties of tin crystals at the temperatures of 298, 333 and 373 K using a Vickers microhardness tester. They observed [001] pencil glide in the crystals and compared the results with that from tensile tests. The activation energy was about 41 kJ/mol. They suggested that the creep was controlled by the cross slip between planes containing the [001] slip vector.

Mayo and Nix [83] investigated the creep properties of Pb, Sn and Sn38wt%Pb alloy using nanoindentation with a Berkovich pyramidal nanoindenter. They also carried out conventional tensile creep for comparison. For pure Pb and Sn, the stress exponents obtained within one single grain were 8.5 and 11, which were higher than those from the conventional creep tests. The effect of grain boundary was small for the indentation creep of single grain. However, the stress exponent was 6 for polycrystalline Sn obtained from indentation creep involving the deformation of many grains. For polycrystalling

Sn38wt%Pb alloy, the stress exponent was 2 which is equivalent to that from the tensile creep test.

Geranmayeh and Mahmudi [111] studied the creep behavior of the Sn-5%Sb solder alloy using a Vickers hardness tester at room temperature. The stress exponents were determined for the materials with different heat-treatment, unhomogenized cast (UC), homogenized cast (HC), unhomogenized wrought (UW), and homogenized wrought (HW). They found that the stress exponent values of about 5 and 12, depending on the processing route of the materials. The stress exponents were very close to those from the conventional testing method. The HW alloy had stress exponent of about 5, and for all other conditions, the stress exponents were about 12.

Han et al. [112] used Berkovich depth-sensing indentation to study the creep behavior and hardness of Sn-3.5Ag-0.7Cu solder at temperatures ranging from 25 °C to 125 °C. The activation energy was about 40 kJ/mol and the stress exponents were about 7.4, 5.5, and 3.7 at 25 °C, 75 °C, and 125 °C, respectively. They observed that, with increasing temperature, the steady-state creep strain rate increased whereas the stress exponent decreased. The stress exponent and activation energy results indicated that the creep mechanism was dislocation climb, assisted by diffusion through dislocation cores in Sn. Furthermore, the hardness results exhibited a decreasing trend with increasing temperature, which was attributed to softening at high temperature.

2.6.6 Stress relaxation

Stress relaxation is the stress relief for materials under constant strain condition. During the stress relaxation tests, the stress condition and deformation process are similar to those for real soldering joints. It has been thought that the stress relaxation and tensile tests were more suitable for the characterization of solder reliability than creep tests [113]. Compared with conventional creep test, the stress relaxation can save testing time. Also, the stress relaxation technique covers the response of material over relatively broad stress and temperature range without large plastic deformation [113]. The stress and strain relationship used to analyze the behavior of material is similar to that for the creep test.

Baker and Kessler [114] conducted compressive stress relaxation tests of chill cast 60/40 Sn-Pb solder under initial stress of 6.89 and 24.8 MPa at temperature ranging from 27 °C to 108 °C. The activation energy was found to be 67 kJ/mol, which did not depend on the initial stress level. The stress exponent was around 3.4 for strain rates between 7×10^{-8} and 10^{-9} s^{-1}.

Kashyap and Murty [115] studied the stress relaxation behavior of eutectic Sn-Pb solder alloy in the temperature range of 298 to 443 K. They found that the stress exponent was 1.7 and the activation energy was 44.5 kJ/mol at lower stress levels and the stress exponent was 11.1 and the activation energy was 100 kJ/mol at higher stress levels. The activation energy at higher stress levels suggested that the stress relaxation was dominated by dislocation climb.

Arrowood and Mukherjee [116] investigated the stress relaxation behavior of eutectic Sn-Pb alloy. They found that the stress exponent were 2.08 in the stress range of 1 to 6 MPa and 2.92 at higher stress which suggested that different rate controlling processes operated in the low and the high stress region.

Hare and Stang [113] investigated the stress relaxation behavior of eutectic tin-lead solder with different casting microstructures. The stress relaxation data was analyzed to extract constitutive relations for creep. According to the power law relation, the stress exponent was 3.2 at low stress levels and 6.2 at higher stress levels. The activation energies were 69 kJ/mol at low stress levels and 64 kJ/mol at high stress levels. The stress exponents and activation energies values indicated that the stress relaxation was controlled by viscous dislocation glide at low stress regime and by dislocation climb at high stress regime.

Mavoori et al. [85] compared the creep behavior of two eutectic lead-free solders (96.5Sn-3.5Ag and 91Sn-9Zn) using conventional creep and stress relaxation tests. The stress relaxation tests were performed under constant-strain condition with strains in the range of 0.3-2.4% and at 25°C and 80°C. They found that the stress exponents were 6 and

4.2, and the activation energies were 33.5 and 106.9 kJ/mol, for 96.5Sn-3.5Ag and 91Sn-9Zn, respectively.

2.6.7 Electrical creep deformation

Recently, Zhu's group investigated the stress relaxation behavior of pure tin and Sn-3.8Ag-0.7Cu solder joints [117, 118]. They found that the stress relaxation was accelerated after exposing to current stressing for a certain time. The accelerating effect increased with the current stressing time. They suggested that electromigration caused the vacancy accumulation, which then led to the increase of the stress relaxation rate. For Sn-3.8Ag-0.7Cu joints, the stress relaxation rate was enhanced when the solder joints was subjected to a current density of 2 x 10^4 A/cm^2. They found that the formation of Sn hillock was dependent on the current passing time. The hillock volume increased with the increasing current application time. For pure tin, the stress exponent was 2.4 for the sample without current stressing, while the value was only 9 for the sample after current stressing. The activation energy was 86.4 kJ/mol for the sample without current stressing and 42.9 kJ/mol for the sample after current stressing. From the measured values of stress exponent and activation energy, the dominant mechanism of the stress relaxation changed from dislocation climb to grain boundary diffusion after current stressing. They suggested that the change of vacancy concentration at the grain boundary was the main mechanism for a higher stress relaxation rate after current stressing.

There are few publication about the creep deformation of solder alloys through which there is an electric current. Kinney et al. [9, 10] reported the creep deformation of Sn-Ag-Cu solder alloy with imposed current using double shear creep technique. The imposed current densities were ranging from 1×10^3 A/cm^2 up to 6.5 x 10^3 A/cm^2. They found that the creep rate obviously increased with the imposed current density. As the imposed current density increased, the steady state creep rate increased. Their results showed that the microstructure of the solders was different between the specimens prepared by electromigration and isothermal aging. They found no significant effect of the microstructure on the creep rate no matter whether the change of the microstructure was caused by temperature or current. They concluded that the increase of creep rate was

caused by the temperature increase and the imposed electric current may reduce the steady state creep rate.

It is difficult to apply electric current of high density current in conventional creep tests due to larger cross-section area of solder samples. Impression creep is a good way to apply high current density during tests. Chen and Yang [13] studied the creep behavior of a Sn60Pb40 alloy with passing an electric current through the sample by using impression creep. The punching stress was in the range of 9.7 to 110 MPa, and the temperature was in the range of 323 to 383 K. They found that the steady state impression velocity increased with increasing electric current under the same punching stress. The activation energy decreased linearly with the square of the electric current. They also investigated the impression creep of pure tin with the passing of electric current [12]. The punching stress was in the range of 12 to 55 MPa, and the temperature was in the range of 343 to 398 K. Similar to the creep deformation of Sn60Pb40 alloy, the steady state impression velocity increased with increasing electric current, and the activation energy decreased with increasing electric current. They suggested that the increased velocity was due to Joule heating and the momentum exchange between atoms and electrons.

Chapter 3 Electromechanical responses of Cu strips

3.1 Introduction

The continuous demand for high speed and great performance of electronic devices and systems has led to the miniaturization of electronics and a significant increase in electric current density. This has led to the replacement of Al by Cu as electronic interconnects in high-performance electronics and high-power IC chips due to low resistivity and low RC delay of Cu [14, 15]. It is known that electronic interconnects of small scale can carry electric current of high densities of $1MA/cm^2$ or higher [119], and high current density can seriously affect device's reliability and potentially cause electromechanical failure of electronic interconnects.

There are numerous studies focusing on analyzing the effect of "electron wind" created by electric current of high current density on the mass transport and structural stability in Cu-interconnect lines [14, 15, 50, 51, 53-55, 119, 120]. Using package level electromigration tests, Shao et al. [15] investigated the electromigration in dual damascene copper interconnects and found that the Cu/Si_3N_4 interface is the fast path of Cu migration when subjected to a current density of $1.2\ MA/cm^2$ at 573 K. Wei et al. [50] observed the formation and growth of hillock in Cu/low-k interconnect structures under the action of electric current of 1.25 and $4.0\ MA/cm^2$.Ryu et al. [49] examined the effects of texture and grain structure on the electromigration of Cu interconnects and found a current density exponent of 2 for the time-to-failure at 473 K. Michael et al. [14] evaluated the mechanisms controlling electromigration failure in submicron Cu interconnects and pointed out that there are two electromigration-failure mechanisms competing in the Cu interconnects depending on the interface condition of the capping layer. Budiman et al. [54] revealed possible effect of electromigration-induced plastic deformation in Cu interconnects on the time-to-failure. Zhang et al. [55] observed local melting during electromigration of Cu conductor lines at 573 and 623 K. Most of the work has focused on the defects and damage created by electromigration in Cu interconnects.

It is known that Cu interconnects experiences electrical-thermal-mechanical deformation due to the passage of electric current of high current density which can lead to the weakening of the mechanical strength of Cu and cause structural failure [121, 122]. Budiman et al. [52] used synchrotron X-ray microdiffraction to reveal the current-induced plastic deformation in damascene Cu interconnects. Zhang and Cargill [56] used synchrotron X-ray microdiffraction to characterize the strain evolution in submicron Cu connector lines with a passivation layer and observed strain relaxation and homogenization in the Cu lines after 120 h of current passage through the Cu lines at 543 K. Zhao and Yang [121] and Yang and Zhao [122] used nanoindentation to examine the effect of AC and DC electric currents on the Young's modulus of Cu wires and observed the decrease of the Young's modulus of Cu wires with increasing electric current density. Park et al. [123] and Zhang et al. [124] used AC current to study thermal fatigue of Cu interconnects. However, there is little study addressing local fusing and current-induced deformation in Cu wires and interconnects.

The material behavior under the action of an electric current depends on local electrical-thermal-mechanical interactions [125, 126], which plays an important role in determining the performance and reliability of microelectromechanical devices and structures. In this work we investigate the electric fusing and current-induced deformation of Cu strips when there is an electric current passing through the Cu strips. The effect of electric current density on the time-to-fusing is examined. The dependence of the deformation of the Cu strips on electric current density is also discussed.

3.2 Current-induced buckling of an elastic strip

Consider a conducting strip with two clamped ends. An electric current passes through the strip and releases Joule heat, which induces thermal deformation of the strip. Zhao et al. [125] had analyzed the steady-state temperature distribution in a conducting strip through which there is an electric current passing. Assuming that the material properties are independent of temperature, one can obtain the temperature distribution for a conducting strip of length L and cross-section area A as [125]

$$T = \left(T_0 - T_\infty - \frac{\rho_e A J^2}{c h_c} \right) \frac{\cosh \omega x}{\cosh(\omega L / 2)} + T_\infty + \frac{\rho_e A J^2}{c h_c} \quad (3.1)$$

where T_0 is the temperature at the ends of the strip, T_∞ is the temperature of environment (i.e. the temperature suitably far from the surface), J is electric current density, c is the summation of the surface area per unit length, ρ_e is electric resistivity, h_c is the heat transfer coefficient, and $\omega^2 = c h_c / kA$ with k being thermal conductivity.

For small-thermal deformation of a Cu strip under the action of an electric current of small current density, the deflection of the Cu strip can be described as linearly elastic. The average electrothermal strain of the Cu strip with clamped ends is calculated as

$$\varepsilon_{therm} = -\frac{\alpha}{L} \int_{-L/2}^{L/2} (T - T_\infty) dx$$

$$= -\alpha \left[\left(T_0 - T_\infty - \frac{\rho_e A J^2}{c h_c} \right) \frac{\tanh(\omega L / 2)}{\omega L / 2} + \frac{\rho_e A J^2}{c h_c} \right] \quad (3.2)$$

which gives the current-induced axial force to the Cu strip as

$$F = \sigma A = -\alpha E A \left[\left(T_0 - T_\infty - \frac{\rho_e A J^2}{c h_c} \right) \frac{\tanh(\omega L / 2)}{\omega L / 2} + \frac{\rho_e A J^2}{c h_c} \right] \quad (3.3)$$

Here σ is stress, is the coefficient of thermal expansion, and E is Young's modulus. It is known that there is a critical load for the occurrence of the beam buckling (lateral deflection) under the action of a compressive axial force. The critical load for the buckling of a rectangular strip depends on the dimensions and the elastic modulus as [127]

$$F_{cr} = -\frac{\pi^2 E w t^3}{3L^2} \quad (3.4)$$

With w and t being the width and the thickness of the strip, respectively. Note that the negative sign represents compressive force. Substituting Eq. (3.3) into Eq. (3.4), one obtains the critical current density for the current-induced buckling of the Cu strip as

$$J_{cr} = \left(\frac{ch_c}{\rho_e wt}\right)^{1/2} \left(\frac{\pi^2 t^2}{3\alpha L^2} - (T_0 - T_\infty)\frac{\tanh(\omega L/2)}{\omega L/2}\right)^{1/2} \left(1 - \frac{\tanh(\omega L/2)}{\omega L/2}\right)^{-1/2} \tag{3.5}$$

Which is independent of elastic properties of materials. For elastic strips of the same length and thickness, the critical current density increases with decreasing the strip width; and for the same cross-section size, the critical current density decreases with increasing the strip length.

Note that the above analysis is based on elastic buckling of Eq. (3.4). For plastic bucking of a rectangular strip, the tangent-modulus theory [127] needs to be used and the calculation of the stress in the strip needs to consider the stress-strain relationship for the plastic deformation of copper.

For the buckled strip with small deflection, the maximum deflection can be calculated as

$$\delta = -\frac{6FeL^2}{Ewt^3} = \frac{6\alpha eL^2}{t^2}\left[\left(T_0 - T_\infty - \frac{\rho_e wtJ^2}{ch_c}\right)\frac{\tanh(\omega L/2)}{\omega L/2} + \frac{\rho_e wtJ^2}{ch_c}\right] \tag{3.6}$$

with e being the eccentricity. The maximum deflection is a linearly increasing function of the square of electric current density and increases with the increase of the strip length. It is worthy of pointing out that it is impossible to obtain closed-form solutions for large deflection of the buckled strip. One needs to consider the contribution of plastic deformation and uses numerical techniques to obtain numerical solutions.

3.3 Experimental

The pure Cu wires used in this study were obtained from McMaster-Carr (Chicago, IL). The Cu wires of 0.254 mm and 0.508 mm in diameter were rolled into thin strips,

and the thickness of the Cu strips was 0.085±0.002 mm for the wires with a diameter of 0.254 mm and 0.125±0.002 mm for the wires with a diameter of 0.508 mm. The thin strips were then cut into the controlled lengths. All the specimens were cleaned with acetone using an ultrasonic cleaning machine before being placed between two electrodes.

The configuration of a beam clamped at both ends was used in experiments, and two Al-based electrodes were made to support the Cu strips. A small tensile force was applied to the strips when mounting the specimen to the electrodes. The tensile force and mechanical pressing at the electrodes between the strip and the Al block caused intimate contact between the strip and the electrodes, which prevented any possible sliding motion of the strips during test. A programmable DC power supply was used to control the electric current passing through the Cu strips in air at room temperature. The passage of electric current caused the release of Joule heat and the deflection of the Cu strips. The deflection of the Cu strips was detected and recorded by a Nikon Digital Camera (Tokyo, Japan).The electric current densities were in the range of 18.26 to 29.60 kA/cm^2 for the Cu strips with thickness of 0.085±0.002 mm and 12.33 to 22.20kA/cm^2 for the Cu strips with thickness of 0.125±0.002 mm. The change of the electric voltage between the two electrodes was recorded and the resistance change of the thin Cu-strips was calculated for each specimen.

3.4 Results and discussion

During the passing of an electric current through the Cu strips, the electric current intensity was maintained constant. The deflection of the strips was recorded. Figure 3.1 shows the deflection evolution of a Cu strip of 0.085 mm in thickness and 50 mm in length under the action of an electric current of 19.24kA/cm^2. Shortly after passing the electric current through the Cu strip, the Cu strip deflected with the central portion moving downwards. The magnitude of the maximum deflection increased with time. Such behavior resembles to the buckling of an elastic beam when subjected to an axial-compressive load. Note that the upward deflection was also observed. The deflection direction depended on local surface curvature at the initial state.

It is interesting to note that a hot spot started at the center of the Cu strip and grew towards both ends with increasing time. Finally, local fusing occurred accompanying with strong thermal radiation at the center of the strip. After electric fusing, the geometrical configuration of the Cu strip remained approximately the same as that just before the occurrence of the electric fusing. This result indicates that the Cu strip experienced plastic deformation due to the passage of the electric current. It is worthy of pointing that, for electric currents of small current densities, Cu strips approximately restored to the initial shape after switching off the electric circuit.

A Leo 1526 scanning electron microscopy (SEM) (LEO Electron Microscope Ltd., England) was used to characterize the microstructures of the Cu strips which were melted during the passing of electric current of high current density. In general, there exist three regions: 1) melted region, 2) heat-affected zone, and 3) oxidation region, as shown in Fig. 3.2 for a melted Cu strip of 0.085 mm in thickness and 50 mm in length after passing an electric current of 20.72 kA/cm^2 through the Cu strip. The microstructures in all three regions are depicted in Fig. 3.3.The Cu strip in the melted region clearly had equal-axial grain structures on the surface with grain boundaries showing off-sets, which was due to the fast cooling from melting point to room temperature. Under the condition of fast cooling, atoms did not have enough time to migrate to the equilibrium positions. The grain size in the melted region varied from 5 to 100 μm. In contrast to the microstructures in the melted region, relatively uniform-distributed grains on the surface of the Cu strip were present in the heat-affected zone. The grain size was about 10 μm. The grain boundaries in the heat-affected zone also showed off-sets, even though a thin layer of Cu oxide was formed. In the oxidation region, no grain structures were observable due to the formation of a thick layer of Cu oxide. Local delamination of the Cu oxide was observed which likely was due to large compressive stress created during the oxidation of Cu.

High energy synchrontron X-ray diffraction experiment of the melted Cu strip with incident energy 115 keV, and beam size 250×500 μm^2 was done at the 11-ID-C beam line of the Advanced Photon Source, Argonne National Laboratory (ANL).The incident X-ray transmitted to the thickness of the sample and was perpendicular to the rolling direction.

The diffraction data was collected by a PerkinElmer 2-D detector. Figures 3.4 and 3.5 show the XRD diffraction rings and the corresponding XRD patterns in different regions, respectively. For comparison, the results for the cold rolled Cu are also included in Figs. 3.4 and 3.5.

The cold rolled Cu strip shows strong textures. Only pure FCC Cu can be identified in the cold rolled Cu with unique textures of <111> and <200> along the rolling direction and <220> with 45 ° to the rolling direction. In the oxidation region, the textures remained approximately the same as the cold-rolling textures due to the lack of enough thermal energy to change the textures in this region. The textures were slightly changed in the heat-affected region, due to grain recrystallization and grain rotation. Large diffraction spots confirmed the presence of grains of large grain sizes in the Cu strip, indicating grain growth due to Joule heating. Slight oxidation occurred and the oxide is Cu_2O. Grains with different grain sizes were present in the heat-affected zone. FCC Cu and FCC Cu_2O were identified through the peak analysis. The XRD diffraction rings suggest that relatively uniform grains of large grain sizes were present in the melted region. The <111> and <200>textures disappeared with the grain growth. Grain rotation likely occurred in the Cu strip under the action of the electric current of high current density as suggested by Chen et al. [128], and the grain growth was likely due to the Joule heat created by the passage of the electric current.

It is worthy of mentioning that the temperature distribution in the melted region was not uniform which resulted in non-uniform distribution of temperature gradient. The recrystallization in the melted region thus caused the formation of grains with different grain sizes, as revealed by the SEM and XRD. Due to fast cooling from near melting point to room temperature after electric fusing, the surface of the Cu strips experienced faster cooling than the inside and large grains formed inside the Cu strip. In the heat-affected zone, grains of small, uniform grain sizes were formed on the surface as observed by SEM and grains of large, non-uniform grain sizes was present inside as shown in the XRD patterns.

As shown in Fig. 3.1, both the deflection and length of the Cu strips increased with time with the passage of an electric current of high current density. The increase in the length generally is controlled by thermal expansion and the axial load due to the confinement to the motion of the ends of the Cu strips. Figure 3.6 shows the variation of the maximum deflection with time for four melted Cu strips with the passage of electric current of four current densities. The strips had 0.085 mm in thickness and 50 mm in length. Immediately after the passage of the electric currents, the maximum deflection of the Cu strips increased to the maximum values at the time of 4~5 s, remained at the maximum values for some time before the occurrence of electric fusing. It is interesting to note that there was a period in which the deflection of the Cu strips remained unchanged. This result suggests that, in this period, the electric current could not cause further deformation of the Cu strips possibly due to local softening near the hot spot. The hot spot caused the decrease of local yield stress and electrical-thermal-mechanical interaction led to plastic deformation of the Cu strips.

Figure 3.7 shows the variation of the maximum deflection of the Cu strips in the quasi-steady state period with electric current density. The maximum deflection in the quasi-steady state period increases linearly with increasing electric current density in contrast to the square dependence as given in Eq. (3.6). Such a difference is due to the plastic deformation of the Cu strips. When subjected to electric current of high current density, Joule heating caused the increase of the temperature in the Cu strips as shown in Fig. 1 and the decrease of yield stress. The decrease of yield stress and the increase of temperature made it easily to introduce plastic deformation in the Cu strips under the action of current-induced thermal axial-load. For Cu strips with the same cross-sectional area under the action of the same current density, the maximum deflection increases with the increase of the strip length qualitatively in accord with the analysis in the previous section. From Fig. 3.7, one can note that the rate of $L^{-1}d\delta / dJ$ approximately is a constant for the experimental conditions used in this work, which is independent of the strip length and electric current density. The mechanism controlling such behavior is unclear.

Generally the change in the maximum deflection of the Cu strips is related to the change in the strip length of ΔL. From Fiq. 3.1, the deflection profile of the Cu strip can be approximated as

$$w = \frac{\delta}{2}(1 + \cos\frac{2\pi x}{L}) \tag{3.7}$$

With w being the deflection of the Cu strip. Note that Eq. (3.7) has been extensively used to analyze the buckling of an elastic beam. However, the Cu strip as shown in Fig. 3.1 had experienced elastoplastic deflection, which suggests that Eq. (3.7) can also be used to approximate the elastoplastic buckling of a beam under the condition of $\delta / L < 0.09$. Thus, the length change of the Cu strip can be calculated as

$$\Delta L = \int_{-L/2}^{L/2} \sqrt{1 + \left(\frac{dw}{dx}\right)^2}\, dx - L \approx \frac{\pi^2}{4}\frac{\delta^2}{L} \tag{3.8}$$

For $\delta / L < 0.09$, the total strain can be approximated as $\Delta L / L$ for the period of quasi-steady state, i.e.

$$\varepsilon_T \approx \frac{\Delta L}{L} \approx \frac{\pi^2}{4}\frac{\delta^2}{L^2} \tag{3.9}$$

According to the results shown in Fig. 3.7, there is

$$L^{-1} d\delta / dJ = \chi \tag{3.10}$$

With χ being a constant dependent on the material properties and geometrical configuration of the Cu strip. Substituting Eq. (3.10) in Eq. (3.9), one obtains

$$\varepsilon_T \approx \frac{\pi^2}{4}\chi^2 J^2 \tag{3.11}$$

for the current-induced buckling of the Cu strips with the passage of an electric current of high current density. Here ζ_c is the intercept on the axis of the maximum deflection of the Cu strips in Fig. 3.7. The total strain is a quadratic function of the electric current density for the experimental conditions used.

The total strain consists of the contribution from elastic strain of ε_e, thermal strain of ε_{therm}, and plastic strain of ε_p, which can be expressed as

$$\varepsilon_T = \varepsilon_e + \varepsilon_t + \varepsilon_p \tag{3.12}$$

Here,

$$\varepsilon_e = \frac{1}{L}\int_{-L/2}^{L/2} \frac{\sigma dx}{E} + \frac{\zeta J^2 wt}{2L}\int_{-L/2}^{L/2} \frac{\nu \mu_m dx}{E} \tag{3.13}$$

$$\varepsilon_{therm} = -\frac{1}{L}\int_{-L/2}^{L/2} \alpha(T - T_\infty) dx \tag{3.14}$$

The second term on the right side of Eq. (3.13) represents the elastic strain induced by the pinch effect. Here ζ is a geometrical factor for the Cu strip, ν is Poisson's ratio, and μ_m is the permeability. For a strain hardening material, the relationship between the plastic strain and stress can be expressed as

$$\varepsilon_p = k\sigma^n \tag{3.15}$$

Where k is a pre-factor, n is the stress exponent. Substituting Eqs. (3.11), (3.13), (3.14), and (3.15) into Eq. (3.12), one obtains an integral equation describing the dependence of the current-induced stress in the Cu strip on electric current density as

$$\frac{1}{L}\int_{-L/2}^{L/2} \frac{\sigma dx}{E} + \frac{\zeta J^2 wt}{2L}\int_{-L/2}^{L/2} \frac{\nu \mu_m dx}{E} - \frac{1}{L}\int_{-L/2}^{L/2} \alpha(T - T_\infty) dx + \frac{1}{L}\int_{-L/2}^{L/2} k\sigma^n dx = \frac{\pi^2}{4}(\chi J + \zeta_c)^2 \tag{3.16}$$

If the temperature dependence of the material properties is negligible, Eq. (3.16) can be simplified as

$$\frac{\sigma}{E}+\frac{\zeta\nu\mu_m J^2 wt}{2EL}-\alpha\left[\left(T_0-T_\infty-\frac{\rho_e AJ^2}{ch_c}\right)\frac{\tanh(\omega L/2)}{\omega L/2}+\frac{\rho_e AJ^2}{ch_c}\right]+k\sigma^n=\frac{\pi^2}{4}(\chi J+\zeta_c)^2 \quad (3.17)$$

The stress evolution is a quadratic function of the electric current density.

From the measurement of the difference of electric potential across the two electrodes, one can calculate the electric resistance of the Cu strips. Figure 3.8 shows the variation of the electric resistance with time for various current densities. Following the transient state, the electrical heating reached a quasi-steady state, in which the electric resistance of the Cu strips increased linearly with time, and the increase rate of the electric resistance increased with the increase of electric current density. Eventually, there was a rapid increase in the electric resistance, representing the occurrence of electric fusing and open circuit. The increase rate of the electric resistance likely is due to the increase in temperature and the growth of surface oxidation. The period of constant increase rate of the electric resistance is corresponding to that in which the deflection of the Cu strips remained unchanged, as shown in Fig. 3.6. In general, the electric resistivity is a linear function of temperature [125, 129]. With the growth of the hot spot in the Cu strips, local temperature increase led to the increase of local electric resistivity and the electric resistance of the Cu strips.

From the change of electric resistance (electric voltage) with time, one can determine the time-to-failure (electric fusing) of the Cu strips when subjected to an electric current of high current density. Figure 3.9 shows the dependence of the time-to-failure of the Cu strips on electric current density in the log-log scales. The time-to-failure decreases with increasing electric current density, as expected, since local temperature increases with the increase of electric current density as given in Eq. (3.1). The time to electric fusing of the Cu strips can be separated into two regions; one is for high electric current density and the other for relatively low current density. In both regions, the time-to-failure, *TTF*, can be expressed as a power function of electric current density as

$$TTF = \omega J^{-m} \quad (3.18)$$

Where ω is a constant dependent on the geometrical configuration of the Cu strips and initial temperature, and m is an current exponent. Using the best curve-fitting, one can determine the current exponent of m, which is listed in table 3.1. In general, the current exponent for relatively low current densities decreases with increasing the length of the Cu strips, while it is relatively independent of the geometrical size of the Cu strips for high current densities. All the current exponents are larger than the current exponent of 2 as predicted by Onderdonk [130] for electric fusing of metals and alloys. Such a difference is likely due to the contribution of surface oxidation to electric fusing, which was not considered by Onderdonk [130]. With the growth of the oxidation layer, the cross-sectional area for the passage of the electric current decreases, and local temperature increases. This trend has accelerated local fusing. For the region of small current exponents, the growth of the surface-oxidation layer is limited by the fast release of Joule heat with the passage of the electric current of high current densities. The current-induced fusing is dominant. For the region of large current exponents, it is the coupling of the surface oxidation and Joule heating which determines the electric fusing of the Cu strips.

3.5 Summary

Electrical-thermal-mechanical interaction determines the electromechanical function of a conducting material when there is an electric current passing through the material. Electric current of a large electric current density can cause electrical-thermal-mechanical deformation of microelectromechanical structures and electronic interconnects. The electromechanical response of Cu strips was studied for the current densities ranging from 12.34 to 29.60 kA/cm^2.The experimental results showed that the passage of the electric current of high current densities caused the growth of a hot spot starting at the center of the Cu strips and eventually led to the electric fusing of the strips. There were three regions related to the growth of the hot spot; they are a) a melted region, b) a heat–affected zone, and c) an oxidation region. Grain growth and grain rotation occurred in both the melted region and heat–affected zone.

The passing of the electric current of high current densities caused the buckling of the Cu strips. The maximum deflection of the Cu strips linearly increased with increasing the electric current density, and there was a quasi-steady state in which the buckling profile of the Cu strips approximately remained unchanged. The total strain is a quadratic function of the electric current density. An integral equation describing the dependence of the current-induced stress in the Cu strip on electric current density was developed. From the measurement of the change of the electric potential difference across two electrodes, it was found that there was a steady state in which the electric resistance of the Cu strips linearly increased with time, which was likely due to the increase of the local temperature and surface oxidation. The experimental results show that the time-to-failure (electric fusing) was a power function of the electric current density, which can be divided into two regions. For the region of relatively low current densities, the current exponent ranged from 17.9 to 44.6; for the region of high current densities, the current exponent ranged from 2.5 to 5.2.

Table 3.1 Summary of the current exponent

Thickness, length (mm):	m For low current density	m For high current density
0.085, 20	44.6	
0.085, 25	37.3	2.5
0.085, 30	27.2	3.7
0.085, 50	17.9	4.9
0.125, 25	32.8	4.1
0.125, 30	34.3	4.2
0.125, 50	20.6	5.2

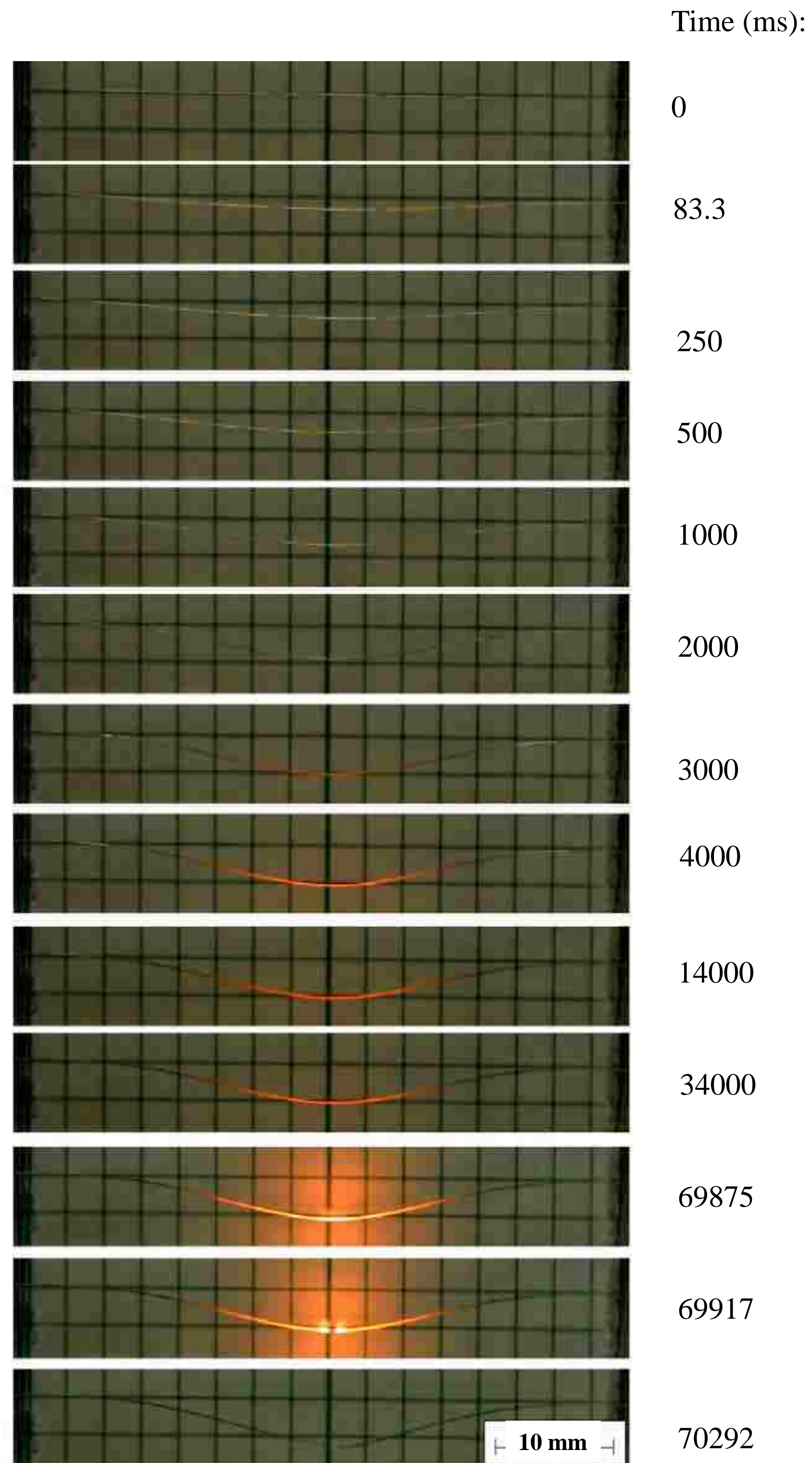

Figure 3.1 Deflection of a copper strip of 0.085 mm in thickness as a function of time under the action of an electric current of19.24kA/cm^2 (length of the Cu strip: 50 mm)

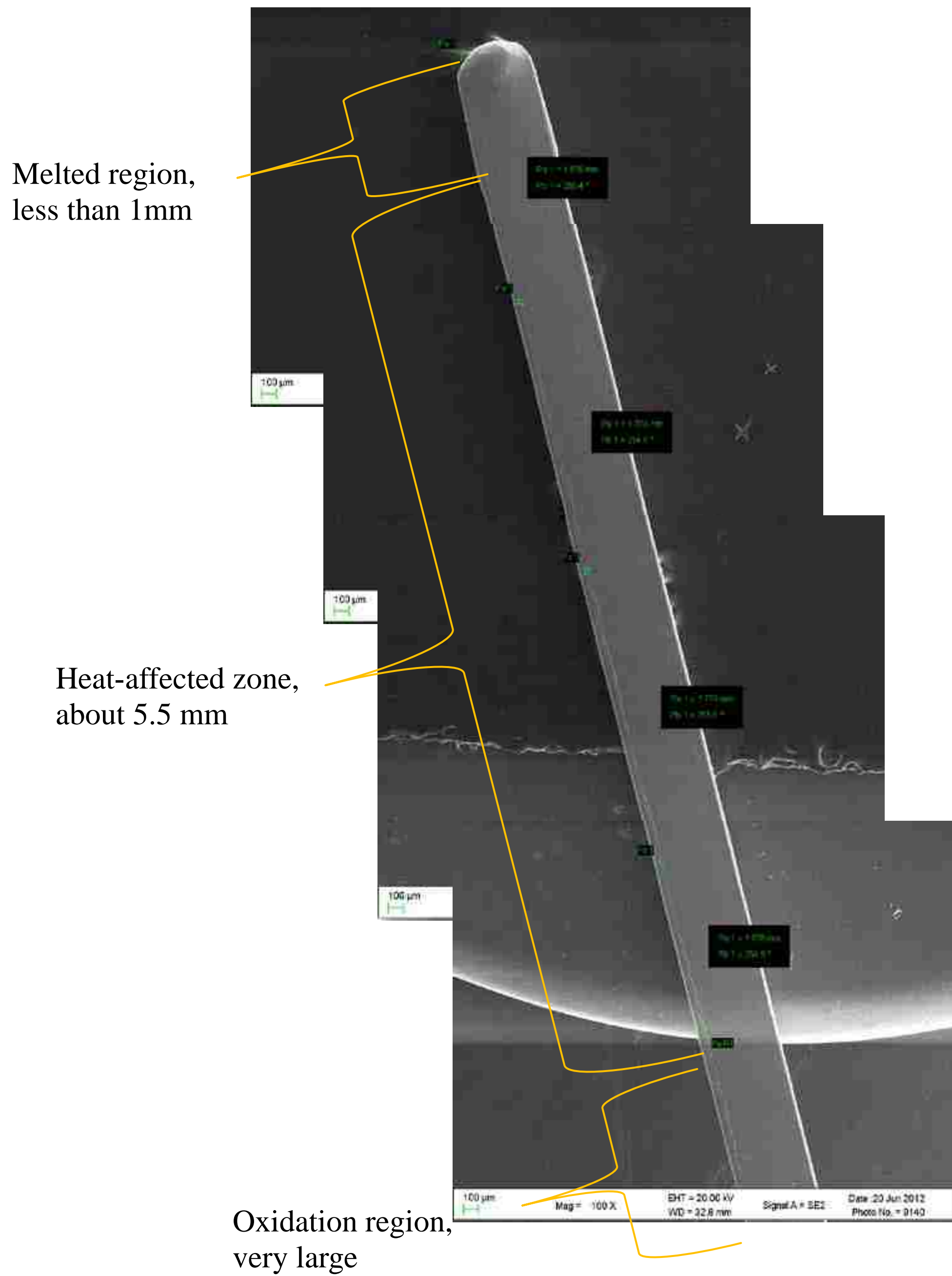

Figure 3.2 An SEM image of a melted Cu strip showing three distinct regions – melted region, heat-affected zone, and oxidation region (Cu-strip thickness: 0.085 mm, Cu-strip length: 50 mm, electric current density: 20.72 kA/cm^2)

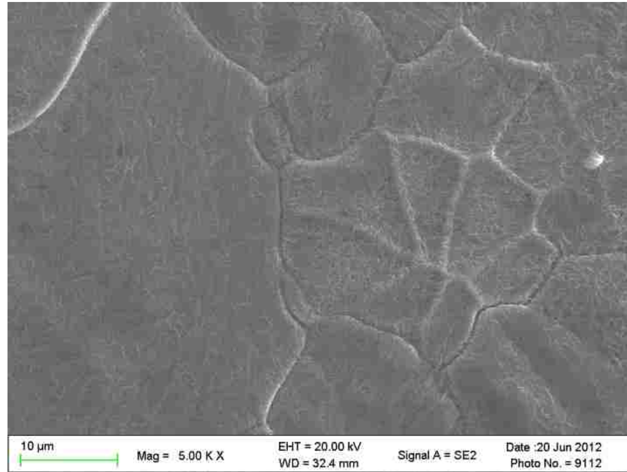

(a)

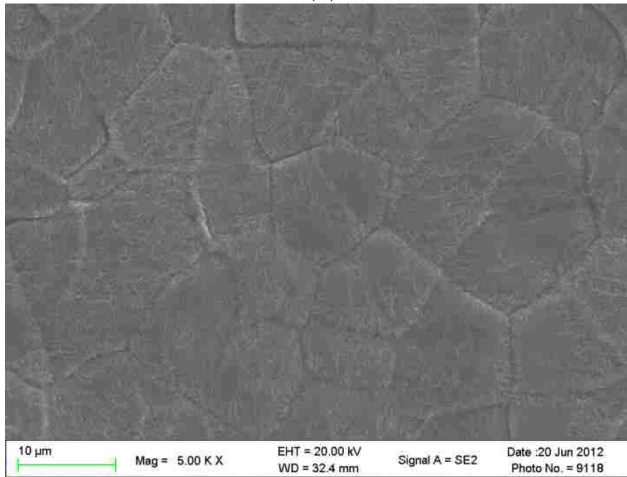

(b)

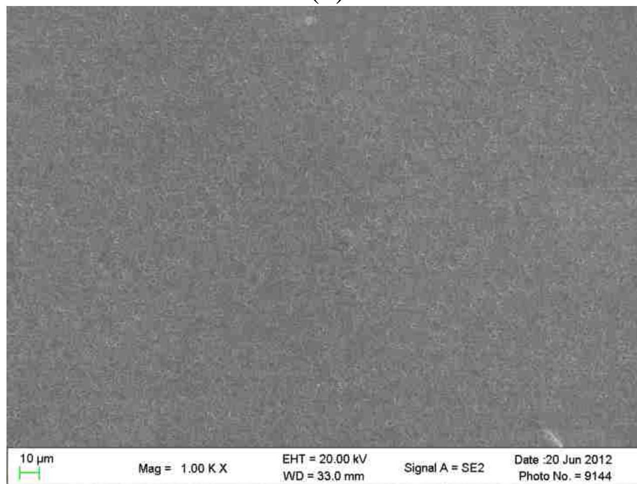

(c)

Figure 3.3 SEM micrographs of a melted Cu strip; (a) microstructure in the melted region, (b) microstructure in the heat affected zone, and (c) microstructure in the oxidation region (Cu-strip thickness: 0.085 mm, Cu-strip length: 50 mm, electric current density: 20.72 kA/cm^2)

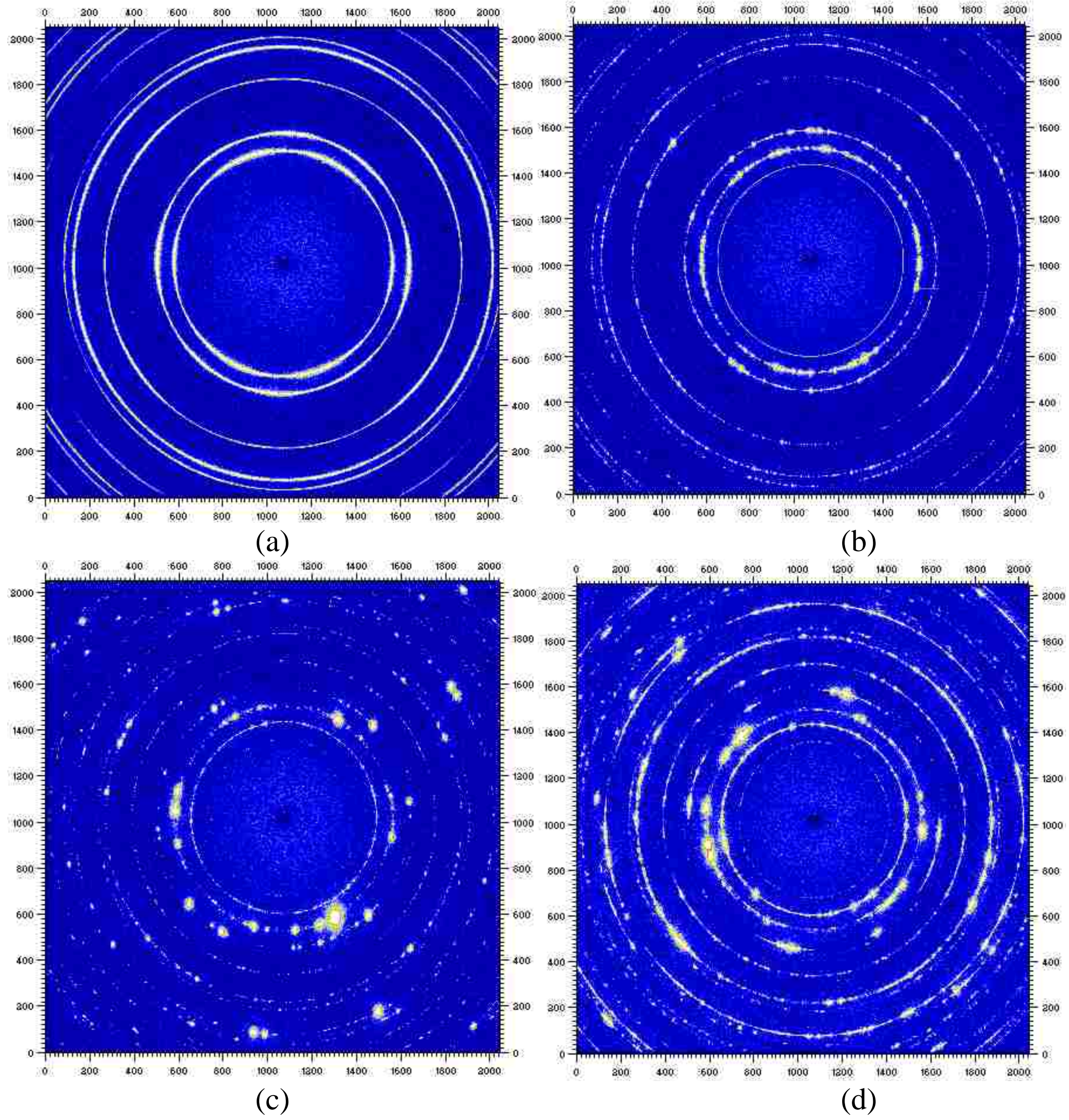

Figure 3.4 Two-dimensional Synchrotron XRD (2D XRD) patterns of the melted Cu strip in different regions; (a) rolled Cu, (b) oxidation region, (c) heat-affected zone, and (d) melted region (Cu-strip thickness: 0.125mm, Cu-strip length: 50 mm, electric current density: 14.31kA/cm^2)

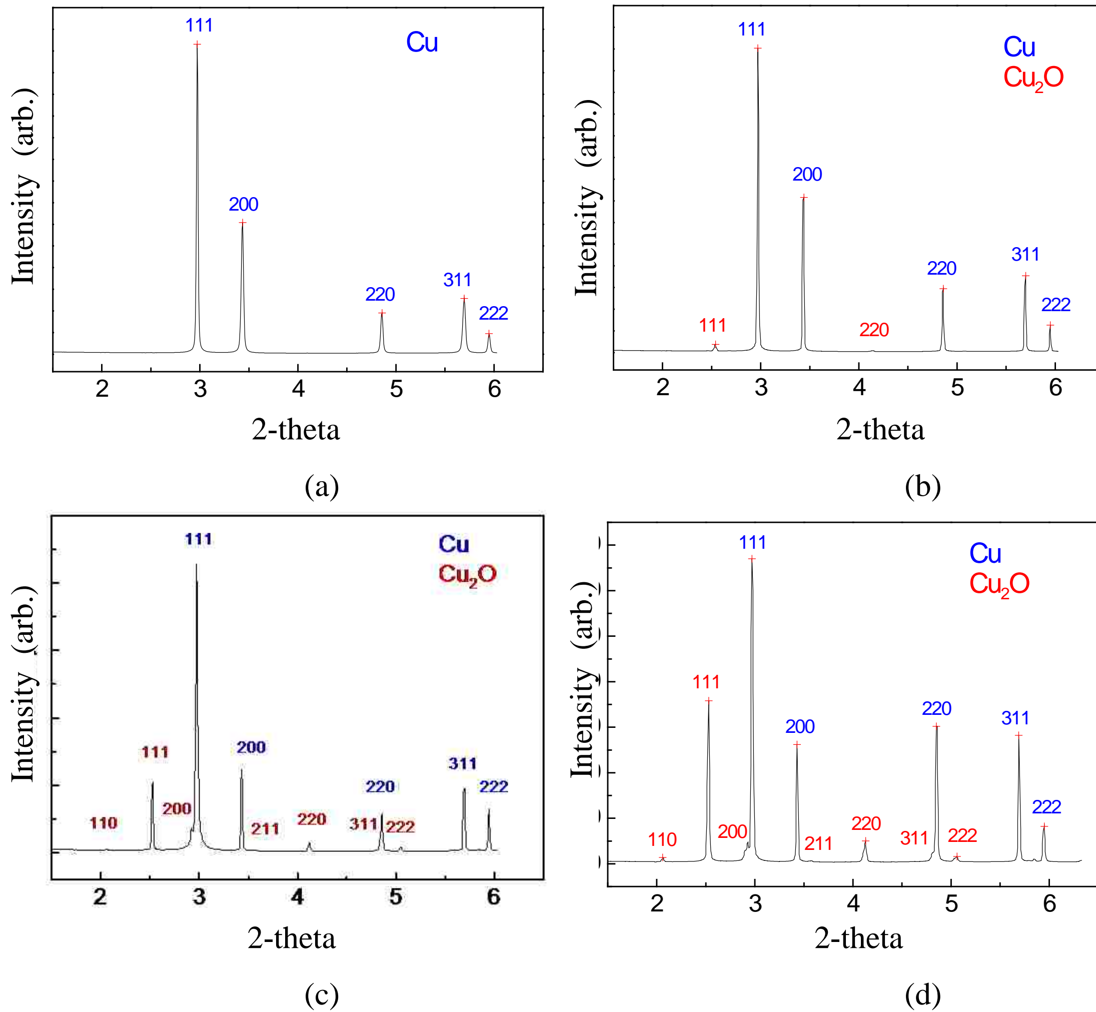

Figure 3.5 XRD patterns of the melted Cu strip in different regions; (a) rolled Cu, (b) oxidation region, (c) heat-affected zone, and (d) melted region (Cu-strip thickness: 0.125mm, Cu-strip length: 50 mm, electric current density: 14.31kA/cm^2)

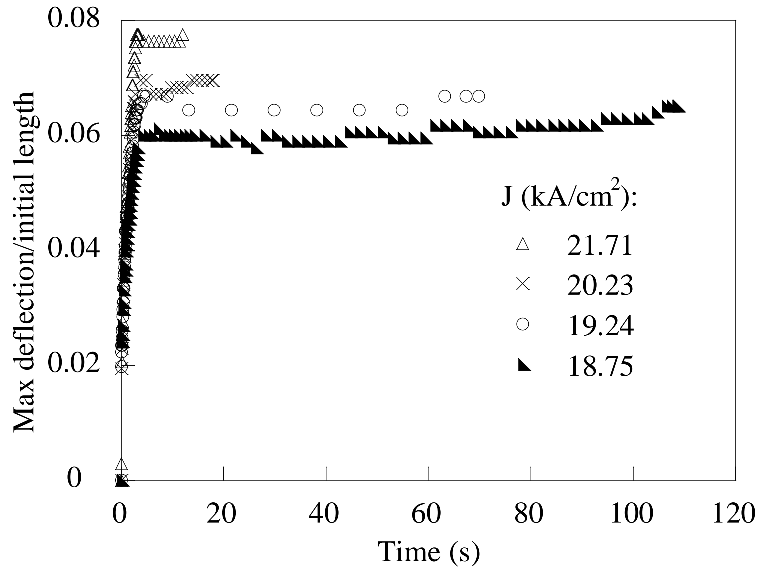

Figure 3.6 Variation of the maximum deflection with time (strip thickness: 0.086 mm, strip length: 50 mm)

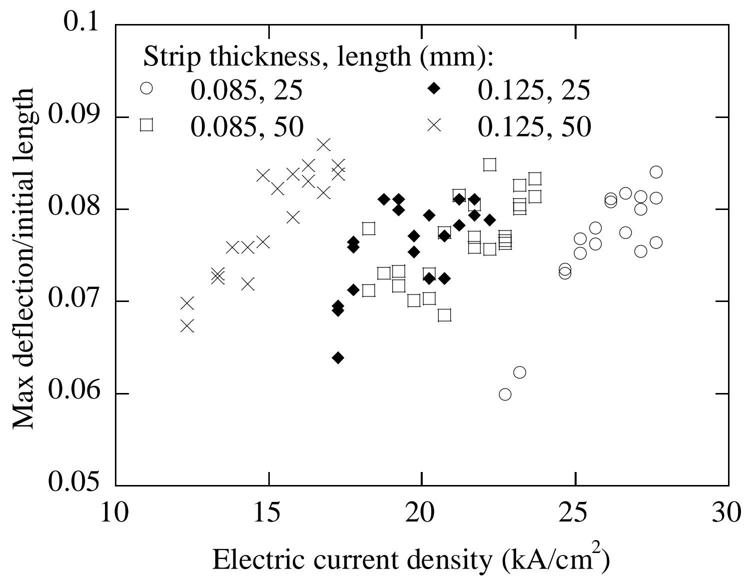

Figure 3.7 Variation of the maximum deflection of the Cu strips in the quasi-steady state period with electric current density

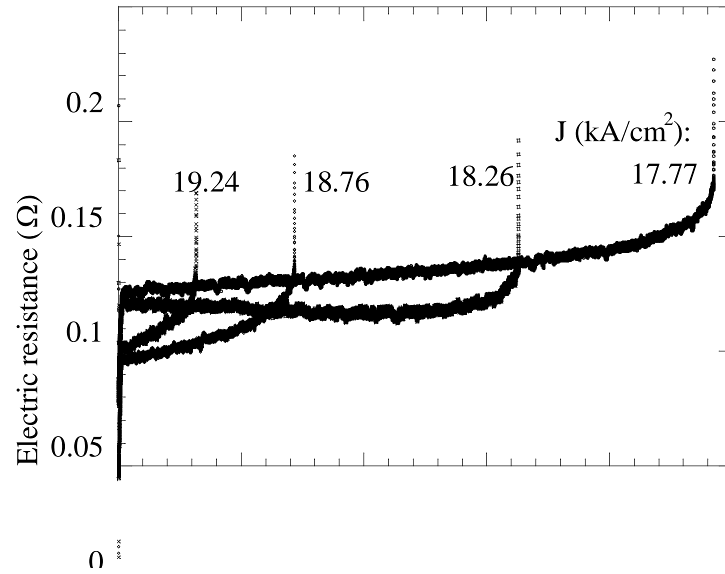

Figure 3.8 Temporal variation of the electric resistance over the Cu strips of 50 mm in length and 0.085 mm, in thickness

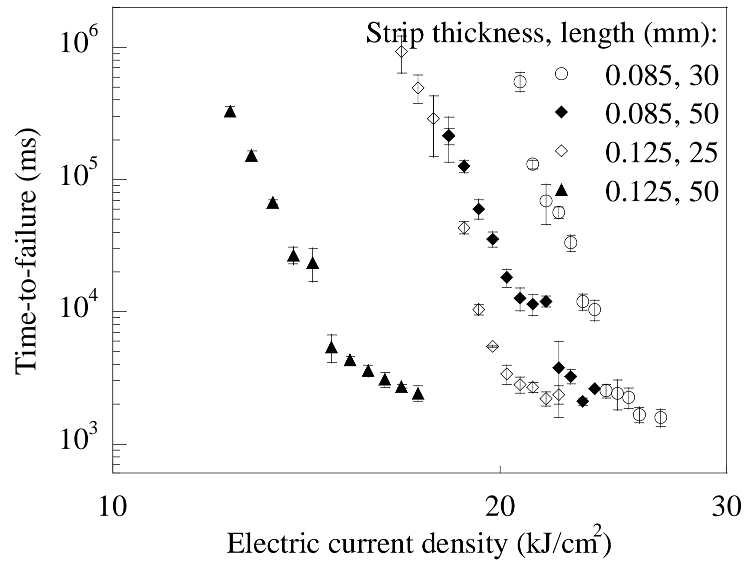

Figure 3.9 Dependence of the time-to-failure on electric current density

Chapter 4 Effect of electric current on nanoindentation of copper wires*

4.1 Introduction

The advances in the microfabrication processing over the past 10-20 years have made it possible to manufacture electromechanical devices on the submicron scale. To increase the device speed and reduce the failure due to electromigration in micro- and nanoelectronics, copper has become a widely used interconnect material due to high electric conductivity and mechanical strength. With the decrease in the feature size of devices and the increase in local electric current density in electronic interconnects, it is necessary to understand the electromechanical behavior of copper in order to improve the structural design of electronic interconnects and our capability of analyzing and predicting structural reliability and the device's performance.

Nanoindentation is a localized testing technique, which can measure the contact modulus and hardness of materials of small volumes. Fang and Chang [131] studied the indentation behavior of copper thin films over several substrates and observed that the indentation hardness of copper films was a function of substrates. Volinsky et al. [76] examined the temperature effect on the nanoindentation of Au and Pt/Cu thin films and found that both the indentation hardness and contact modulus of the films decreased with increasing temperature. Using molecular dynamics simulation, Hsieh et al. [132]simulated the nanoindentation of copper and showed the decrease of the elastic modulus of copper with increasing temperature. None of them had addressed the electromechanical effect on the indentation behavior of copper; and there is no research available on the effect of electric current on the nanoindentation of metallic alloys.

---

*Reproduced with permission from Guangfeng Zhao and Fuqian Yang, Nanoscience and Nanotechnology Letters, 2010. 2(4): p. 322-326. Copyright 2010 American Scientific Publishers

Recently, Chen and Yang [133, 134] studied the effect of electric current on the creep deformation of Sn and Sn60-Pb40 alloy and observed that the passing of an electric current through Sn-based alloys increased the creep rate. They suggested that the increase of the creep rate was due to Joule heating and the momentum exchange between high-speed electrons and atoms. One expects that the passing of an electric current likely will have an effect on local mechanical response of conducting materials due to electromechanical interaction. It is the purpose of this work to study the indentation deformation of copper wires when there is an electric current passing through the wires. The effect of electric current density is examined on the apparent contact modulus and apparent indentation hardness.

4.2 Experimental

The copper wires used in the study were obtained from McMaster-Carr (Chicago, IL). The as-received copper wires of 0.254 mm in diameter were mechanically ground and polished parallel to the axial direction to obtain a flat and mirror-like surface for the test. The as-polished wires had a cross-section area of about 1.57×10^{-2} mm^2 and were attached to the surface of a glass slide. A small tensile force was applied to the wires during the sample mounting to avoid possible slipping of the copper wires on the glass slide, which might introduce the measurement error. The tensile force and mechanical pressing at both ends of the wires caused intimate contact between the wires and the glass slide, which prevented the indentation-induced flexing motion of the wires. Using the current control, a direct electric current was passed through the wires before performing the indentation test and was maintained a constant value during the test. The temperature rise due to Joule heating was measured using a thermocouple on the surface of the copper wires.

The nanoindentation tests were performed near the central portion of the wires in a Hysitron TriboScope (Minneapolis, MN) attached to a Quesant (Agoura Hills, CA) atomic force microscope (AFM), after reaching thermal equilibrium with continuous passing of electric current. A non-conducting diamond NorthStar cubic indenter with a nominal tip radius of 40 nm (Minneapolis, MN) was used. Constant loading and unloading rates were used in the indentation tests without an intermediate pause between

the loading phase and the unloading phase. For each loading and current condition, at least five indents were performed. The indentation depth and indentation load were recorded, and the slope of the upper portion of the unloading curves was used to calculate the contact modulus and indentation hardness. The machine compliance was calibrated to be 1.0 nm/mN. The calculated apparent contact modulus and apparent indentation hardness were statistically analyzed, and the standard deviation for each condition was used for the error bar in the corresponding diagrams.

To calculate the apparent contact modulus and apparent indentation hardness from the indentation test, the projected contact area must be determined from the unloading curves. This requests the calibration of tip geometry or area function. Using fused quartz (Hysitron, Minneapolis, MN), a series of indentations was made in the depth range of 24.2 nm to 315.3 nm (the corresponding indentation load was in the range of 175 μN to 4500 μN). The curve-fitting of a plot of the projected contact area, A_c in the unit of nm^2, versus the contact depth, h_c in the unit of nm, gave

$$A_c = 2.5807 h_c^2 + 6.9592\times10^2 h_c - 1.391\times10^3 h_c^{1/2} \qquad (4.1)$$

4.3 Results and discussion

Table 1 lists the temperature rise on the surface of the copper wires at thermal equilibrium state. The time to reach the thermal equilibrium state was less than 5 min. The steady state temperature increased with the increase of electric current density. This was due to the release of larger amount of Joule heating when a high electric current was passed through the material. It is known that the Joule heat is proportional to the square of electric current (density). A least square fit of the temperature rise as a function of the current density confirms that the surface temperature rise is proportional to the square of the electric current density in good accord with the Joule heating, i.e., $\Delta T = 3.44 J^2$ (the temperature of T is in the unit of K, and the electric current density of J is in the unit of 10^4 A/cm^2).

Consider the Joule-heating-induced temperature rise in a circular metallic wire of radius a. For a given surface temperature of T_0, the temperature distribution in the wire is [135]

$$T = \frac{J^2}{4k_T\sigma_I}(a^2 - r^2) + T_0 \tag{4.2}$$

Where k_T is thermal conductivity, and σ_I is electrical conductivity. The temperature at the center of the wire is

$$T\Big|_{r=0} = \frac{a^2 J^2}{4k_T\sigma_I} + T_0 \tag{4.3}$$

For copper, the electric conductivity is 59.6×10^6 S/m and the thermal conductivity is 401 W/mK, the temperature rise at the center of a copper wire of radius of 0.07 mm is 37.3 K for an electric current density of 31.8 kA/cm^2 and a surface temperature rise of 37.26 K. Thus, for the experimental conditions used in the work, the temperature gradient in the wires was negligible and the copper wires had a uniform distribution of temperature.

Figure 4.1 shows typical indentation loading and unloading curves of the copper wires with J=0 and 2.55×10^4 A/cm^2. The loading curves for different peak-indentation loads and the same electric current density overlap, suggesting that the loading rate has a negligible effect on the load–displacement relation. For the same indentation load, the slopes of the unloading curves for the indentation of the copper wires with the passing of an electric current of the current density of 25.5 kA/cm^2 are less than those without the passing of an electric current. This trend suggests that the passing of electric current caused the decrease of the apparent contact stiffness of the copper wires. Using Eq. (4.1) and the relationship between the apparent contact stiffness and the contact modulus, one can calculated the apparent contact modulus of the copper wires.

Figure 4.2 shows the variation of the apparent contact modulus of the copper wires with the contact depth for various current densities. In general, the apparent contact modulus decreases slightly with increasing the contact depth, which is consistent with the contact modulus for the nanoindentation of copper films [136]. When there was no electric current passing through the copper wires, the apparent contact modulus is

143.4±17.5 GPa for the contact depth of 22.2 nm in accord with the calculated result of 146.7 GPa for bulk copper at room temperature. The apparent contact modulus of the copper wires with the passing of an electric current is less than that without the passing of an electric current. This result suggests that the passing of an electric current through a copper wire causes the decrease of Young's modulus, i.e. the copper wires became easily deformed elastically. It is worth of mentioning that additional indentation of the copper wires was performed after immediately switching off the electric circuit for an electric current density of 6.4 kA/cm^2. Both the apparent contact modulus and the apparent indentation hardness were the same as those when there was no electric current passing through the wires. For the current density larger than or equal to 12.7 kA/cm^2, it was impossible to make indentation due to the unstable state of the wires possibly from the wire shrinking during the cooling.

The dependence of the apparent contact modulus on electric current is depicted in Fig. 4.2 for various indentation loads. The apparent contact modulus linearly decreases with increasing electric current density for different indentation loads. For the same electric current density, the apparent contact modulus also decreases slightly with the increase of the indentation load. This result implies the effect of electromechanical interaction on the indentation response of the copper wires with the passing of an electric current.

As discussed above, Joule heating can cause a temperature rise in the copper wires, which may result in the decrease in Young's modulus of the copper wires. According to Varshni [5], the temperature dependence of Young's modulus of metals can be expressed as

$$E = E_0 - s/(e^{t/T} - 1) \tag{4.4}$$

Where E is Young's modulus of materials at temperature of T, E_0 is Young's modulus of materials at 0 K, and s and t are constants. At a reference temperature of T_r ($>> 0\,\text{K}$), Eq. (4.4) can modified to the first order of approximation of $\Delta T / T_r$ ($|\Delta T / T_r| < 0.1$) as

$$E = E_0 - \frac{sT_r}{t}\left(1 + \frac{\Delta T}{T_r}\right)$$

$$\equiv E_r - \frac{s\Delta T}{t} \qquad (4.5)$$

Where E_r is the Young's modulus of the material at the reference temperature of T_r, and ΔT is the temperature variation around T_r. The Young's modulus of a material is a linear function of the temperature change, which supports the modulus decrease of bulk copper with increasing temperature in the temperature range of 293 to 403 K [76]. For the temperature rise created by Joule heating ($\Delta T = \alpha J^2$, α is a constant), Eq. (4.5) yields

$$E = E_r - \frac{\alpha s}{t} J^2 \qquad (4.6)$$

Thus, the Young's modulus of the copper wires is a linear function of the square of the current density if Joule heating is the dominant mechanism controlling the variation of elastic response of the copper wires. Obviously, the experimental data shown in Fig. 4.2 does not support Eq. (4.6). This strongly suggests that Joule heating is not the dominant mechanism for the decrease of the Young's modulus of the copper wires when there is an electric current with the current density greater than or equal to 0.64×10^4 A/cm^2 passing through the wires. Equation (4.6) may be used to explain the decrease of Young's modulus with electric current if there is an electric current of small current density passing through materials. In addition, there is an about 75.6% decrease in Young's modulus when an electric current of 3.18×10^4 A/cm^2 was passed through the copper wires, which basically cannot be explained by the temperature dependence of Young's modulus.

It is known that the passing of an electric current through materials can cause the increase in atomic mobility through the momentum exchange between high-speed electrons and atoms in addition to the temperature increase due to Joule heating [2-4]. Under certain conditions, the momentum exchange between electrons and atoms can lead

to electromigration and the electromigration-induced structural damage [4]. As a general rule, copper is susceptible to considerable electromigration at electric current densities greater than or equal to 10^6 A/cm^2 [2]. One expects that the momentum exchange between electrons and atoms created by electric current with current density greater than or equal to 0.64×10^4 A/cm^2 can cause structural distortion and increase the equilibrium distance among atoms.

The change of the equilibrium distance among atoms is dependent on the electromechanical interaction between high-speed electrons and atoms. According to Black [137], the interaction force, *F*, between high-speed electrons and atoms can be written as

$$F = qz^{*}\rho J \tag{4.7}$$

Where qz^{*} is the effective lattice charge and ρ is the resistivity of the material. The force balance on the immobile atoms at lattice sites leads to an increase of the equilibrium distance, Δr, which can be approximately calculated by

$$\Delta r = \frac{qz^{*}\rho}{k} J \tag{4.8}$$

from the lattice model of crystals. Here, k is the spring constant, representing the attraction among atoms. From an atomic viewpoint, Young's modulus of a crystalline material can be calculated as

$$E = \frac{1}{r_e}\left(\frac{d^2U}{dr^2}\right)_{r=r_e} \tag{4.9}$$

Where r_e is the equilibrium distance between atoms at temperature of T and U is the interaction energy among atoms. For $|\Delta r / r_0| << 1$, Eq. (4.9) gives

$$E \approx \frac{1}{r_0}\left(\frac{d^2U}{dr^2}\right)_{r=r_0}\left(1-\frac{\Delta r}{r_0}\right)$$

$$= E_r\left(1-\frac{\Delta r}{r_0}\right) \quad (4.10)$$

With r_0 being the equilibrium distance between atoms at the reference temperature of T_f when there is no electric current passing through the material. Substitution of Eq. (4.8) into Eq. (4.10) yields

$$E = E_r\left(1-\frac{qz^*\rho}{r_0 k}J\right)$$

$$\equiv E_r - \beta J \quad (4.11)$$

The decrease of Young's modulus is a linear function of the current density if the electron-atom interaction controls the variation of the elastic response of materials. This linear relationship is in accord with the experimental results as shown in Fig. 4.3, when there is an electric current of the current density greater than or equal to 0.64×10^4 A/cm^2 passing through the copper wires. From the proportionality between Young's modulus and the contact modulus, a curve-fitting of the results in Fig. 5.2 gives β as 2.55, 2.93, and 2.78 in the unit of GPa/(kA·cm^{-2}) for the indentation loads of 200, 600, and 1000 μN, respectively. It looks like that the parameter of β is relatively independent of the indentation load. The average value of β is 2.75 GPa/(kA·cm^{-2}). This is in accord with Eq. (4.11) that the parameter of β is only controlled by the interaction of high-speed electrons and atoms.

Combining Eq. (4.6) with Eq. (4.11), one obtains the current dependence of Young's modulus to the first order of approximation as

$$E = E_r - \beta J - \frac{\alpha s}{t}J^2 \quad (4.12)$$

Equation (4.12) represents the contribution of Joule heating and the momentum change among high-speed electrons and atoms to the elastic modulus of conducting materials.

Figure 4.4 shows the variation of the apparent indentation hardness on electric current density. For the same electric current density, the apparent indentation hardness decreases with increasing the indentation load, which shows the normal indentation-size effect. In contrast to the decrease of the contact modulus with increasing electric current density, the apparent indentation hardness increases slightly with increasing electric current density. The mechanism for the increase of the apparent indentation hardness is unclear.

It needs to point out that the large error of the apparent indentation hardness for the indentation load of 100 μN might be due to the effect of surface irregularity on the indentation deformation for the indentation by small indentation loads. For small indentation load, surface irregularity such as small asperity can cause large error in calculating the contact depth and contact area. For most of the indentations, the percentage error of the contact depth is less than 10%. However, the percentage error of the contact depth for the indentations made by the indentation load of 100 μN was about 14% for the current densities of 12.7 and 25.5 kA/cm^2 and about 25% for the current density of 31.8 kA/cm^2, which results in the large error bars.

4.4 Summary

Electromechanical interaction determines the mechanical response of electronic interconnects, which plays an important role in controlling the performance and reliability of structural elements used in electromechanical devices of small scales. Large electric current density through electronic interconnects can cause structural distortion and enhance the interaction of electrons and structural defects. Using the nanoindentation technique, the effect of electric current on the indentation deformation of copper wires was studied for the current densities ranging from 0.64 to 3.18 10^4 A/cm^2. The experimental results showed that the contact modulus decreased with increasing electric current density. The decrease of the apparent contact modulus was likely due to the electromechanical interaction, possibly involving the momentum exchange between high-

speed electrons and atoms which increases the equilibrium distance between atoms. An approximate relationship between elastic modulus and electric current density was obtained, which was in good accord with the experimental observation. In contrast to the decrease of the apparent contact modulus with the increase of electric current density, the apparent indentation hardness increased with the increase of the electric current density.

Table 4.1 Variation of the temperature rise with electric current density

Electric current density (10^4 A/cm^2)	0.64	1.27	1.91	2.55	3.18
Temperature rise (K)	3.28±0.61	5.96±0.65	11.00±0.90	19.20±2.42	37.26±1.97

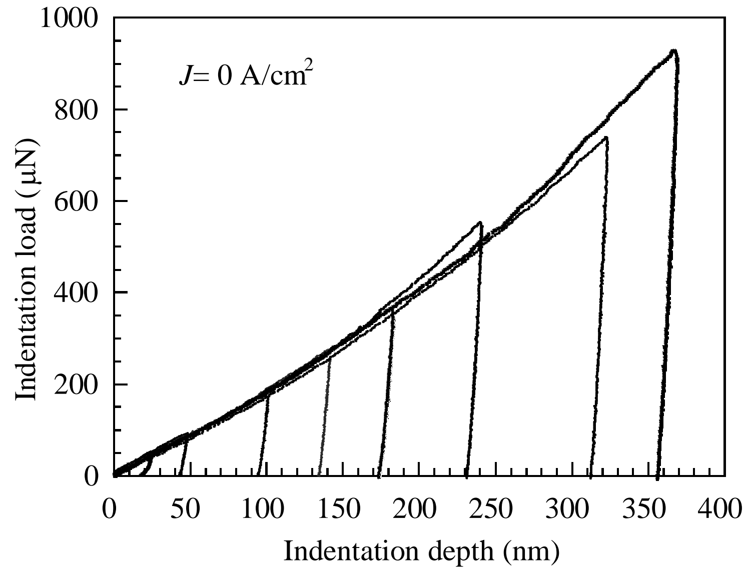

(a)

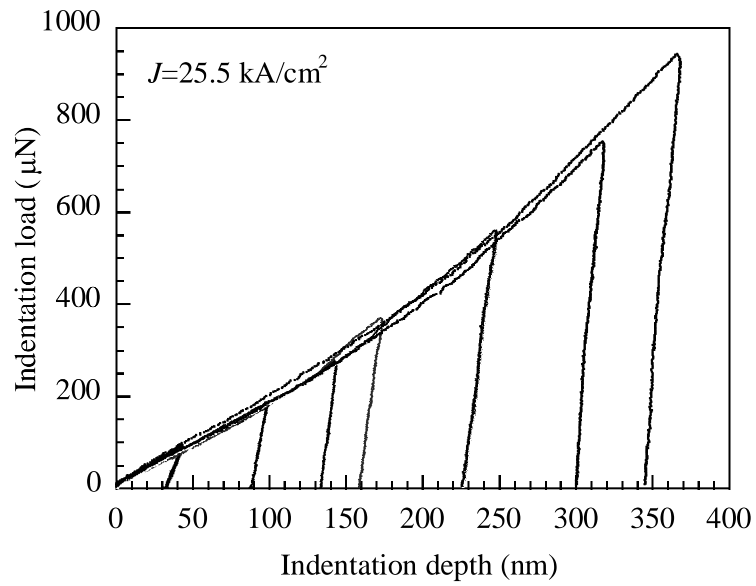

(b)

Figure 4.1 Typical indentation loading-unloading curves for the indentation of copper wires with the passing of an electric current; (a) J= 0 A/cm^2, and (b) J=25.5 kA/cm^2

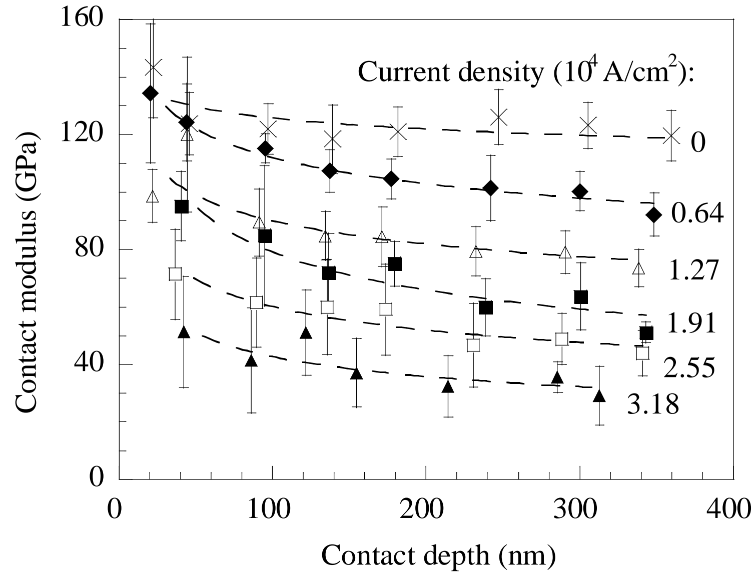

Figure 4.2 Variation of the contact modulus with the contact depth for various current densities

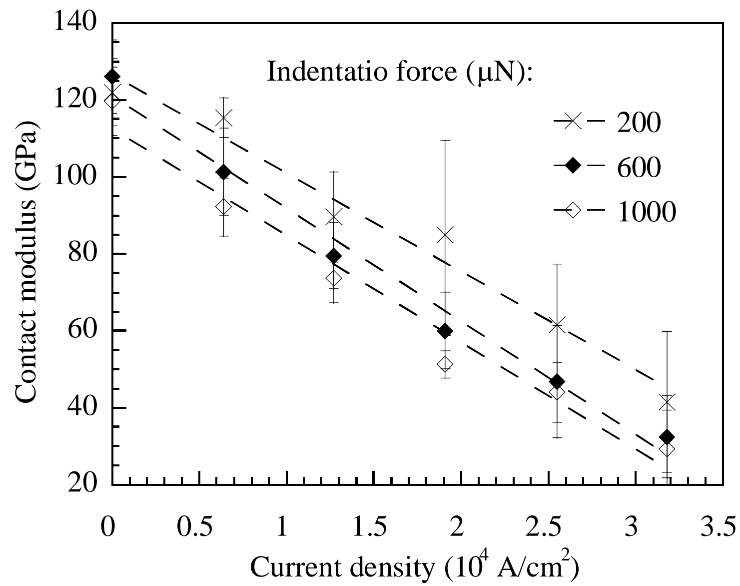

Figure 4.3 Dependence of the contact modulus on electric current density for several indentation loads

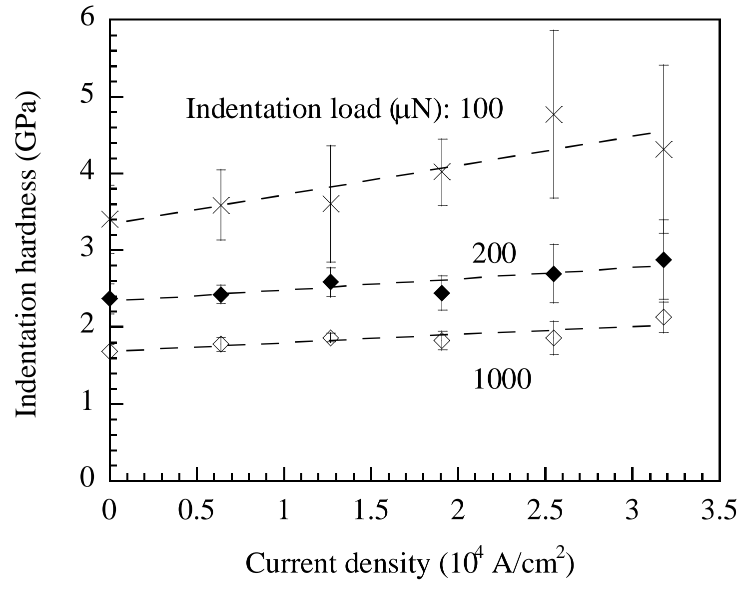

Figure 4.4 Dependence of the indentation hardness on electric current density for several indentation loads

Chapter 5 Effect of alternating electric current on the nanoindentation of copper*

5.1 Introduction

Copper (Cu) has been extensively used in electronic devices and systems as electronic interconnects and electrical connector due to low electrical resistivity. In contrast to structural materials, Cu experiences electrical-thermal-mechanical deformation due to the passing of electric current of high electric current density in an operating electronic device. When an electric current passes through an electronic interconnect, free electrons move with high speed and interact with atoms through momentum transfer, resulting in the change of local structure, including the formation of microvoids [138] and hillocks [139], which can cause structure damage and failure of devices. Recently, researchers had shown that Cu lines may suffer the same electrical-thermal-mechanical reliability problem as the Al ones [140, 141]. It is of paramount importance to understand and analyze the effect of electrical-thermal-mechanical interaction on the mechanical behavior of materials on micro and nanoscales.

The electrical-thermal-mechanical interaction determines the mechanical behavior of materials when there is an electric current of high electric current density passing through the materials. Budiman et al. [52] used synchrotron X-ray microdiffraction to reveal the current-induced plastic deformation in damascene Cu interconnects. Zhang and Cargill [56] used synchrotron X-ray microdiffraction to study the strain evolution in submicron Cu connector lines with a passivation layer and observed strain relaxation and homogenization in the Cu lines after 120 h of current passing through the Cu lines at 270 ^{o}C. Chen et al. [142] used *in situ* high-resolution transmission electron microscopy to

*Reproduced with permission from Guangfeng Zhao and Fuqian Yang, Applied Physics A: Materials Science Processing, 2012. 109(3): p. 553-559. Copyright 2012 Springer

investigate the current-driven migration of incoherent twin boundary in nanotwinned Cu lines through which there was an electric current passing. Ogi et al [143] used picosecond ultrasound spectroscopy to study the high-frequency vibrations of copper nanowires on a silicon substrate and found softening of the copper nanowires under the action of electric current. However, none of these studies has quantitatively characterized the effect of electric current on the mechanical behavior of Cu.

It is known that the contact between two solids will cause local deformation. The study of the contact deformation has led to the development of the sharp instrumental indentation technique, impression technique, and atomic force microscopy, which have been extensively used to characterize the near-surface mechanical behavior of materials. Sebastian and Biswas [144] used wedge indenters to evaluate the effect of interface friction on the indentation hardness of Cu-strips and demonstrated the effect of surface roughness on the hardness-penetration characteristics. Pole et al. [145] studied the size dependence of the microhardness in annealed and work-hardened Cu and addressed the contribution of strain gradients to the indentation deformation. Chaudhri [146] characterized the subsurface strain distribution around Vickers indentation in annealed polycrystalline Cu. Recently, Yang and Zhao [147] examined the effect of direct electric current on the nanoindentation behavior of Cu-wires with the passing of an electric current and observed the decrease of the reduced contact modulus with increasing electric current density. Chen and Yang [133, 134, 148] used the impression technique to study the effect of direct electric current on the creep deformation of Pb, Sn, and Sn60Pb40 alloy and found that the steady state creep rate increased with increasing the electric current density. There is little study addressing the effect of alternating electric current on the local mechanical deformation of Cu, which determines the structural durability of electronic interconnects.

Nanoindentation is a localized testing technique, which has been used to characterize electroplastic deformation of materials of small volumes and has provided numerous insights into the fundamentals controlling localized deformation of materials. This work is focused on the indentation deformation of Cu-strips under the action of electric current.

The effect of the electric current density is examined on Joule heating and the reduced contact modulus. The dependence of the indentation hardness on the electric current density is also discussed.

5.2 Experimental

The Cu-wires used in this study were obtained from McMaster-Carr (Chicago, IL). The as-received copper wires of 0.254 mm in diameter were mechanically rolled into thin strips of 0.2~0.3 mm in thick and ~10 cm in length. The thin strips were then heat-treated in air at 773 K for one hour to release the residual stresses created by machining and rolling and to obtain a homogeneous microstructure before being attached to the surface of a glass slide. A small tension was applied to the strips during the sample mounting to avoid possible slipping of the Cu-strips on the glass slide. The tensile force and mechanical pressing at the contact ends between the strips and the glass slide caused intimate contact between the strips and the glass slide, which prevented the possible indentation-induced sliding motion of the strips.

The copper strips then were mechanically ground and polished parallel to the longitudinal direction, and the cross-section areas of the polished samples were in the range of 1.57×10^{-3} to 1.64×10^{-3} cm^2. Using the current control, an AC electric current of 60 Hz in frequency was passed through the strips before performing the indentation test and the electric current density was maintained a constant value during the indentation test. The electric current densities were in the range of 1.25 to 4.88 kA/cm^2. During the passing of an electric current through the copper strips, the surface temperature of the strips was measured using a thermocouple.

The nanoindentation tests were performed in a Hysitron TriboScope (Minneapolis, MN) attached to a Quesant atomic force microscope (AFM) (Agoura Hills, CA), after reaching thermal equilibrium with continuous passing of an electric current. A non-conducting diamond NorthStar cubic indenter with a nominal tip radius of ~40 nm (Minneapolis, MN) was used. The machine compliance was calibrated to be 1.0 nm/mN. During the test, the indentation load in the range of 100 μN to 1600 μN was used. Both

the loading time and unloading times were 10 s, and there was no intermediate holding period between the loading phase and the unloading phase. The tests were conducted after reaching thermal equilibrium with the passing of an electric current. For each loading and current condition, at least fifteen indents were performed. The indentation depth and indentation load were used to calculate the reduced contact modulus and indentation hardness.

5.3 Results and discussion

5.3.1 Electrothermal curves

During the electrothermal test, an AC electric current was passed through the specimen and the electric current intensity was maintained constant. The local surface temperature at the center of the Cu-strips was measured as a function of time. Figure 5.1 shows the variation of the surface temperature of the Cu-strips with time. The surface temperature initially increased with time and reached a constant value following a transient state. The time to reach local thermal equilibrium was less than 200 s. The surface temperature increased with increasing the current density. This was due to the release of larger amount of Joule heat when an electric current of high electric current density was passed through the strips.

Figure 5.2 depicts the dependence of the steady state surface temperature rise ($\Delta T = T - T_\infty$, T: the surface temperature, and T_∞: the temperature of environment) on the current density, J, in the unit of kA/cm^2. The surface temperature rise increased with the increase of the electric current density due to the release of Joule heat. The highest temperature rise was 10.1 K for an electric current density of 5.19 kA/cm^2. It is known that Joule heat is proportional to the square of electric current (density). A least square fit of the temperature rise as a function of the current density confirms that the surface temperature rise is proportional to the square of the electric current density in good accord with the Joule heating for the experimental conditions, which can be expressed as

$$\Delta T = 0.378 J^2 \tag{5.1}$$

The temperature rise in the Cu-strips was controlled by the Joule heating due to the passing of an electric current.

5.3.2 Electric nanoindentation

During the indentation test, the electric current intensity was maintained constant. The loading-unloading curves are shown in Fig. 5.3 for the indentation of the Cu-strips without the passing of an electric current. For comparison, the corresponding curves with the passing of an electric current density of 4.88 kA/cm^2 are also shown in the figure. The loading curves for different indentation loads under each individual current condition overlap, suggesting that the loading rate has a negligible effect on the load–displacement relation. There was no pop-in event observable for both the loading and unloading phases. For the indentations made by the indentation load larger than or equal to 1000 μN, the slops of the unloading curves for the indentation of the Cu-strips without the passing of an electric current are larger than those with the passing of an electric current of the current density of 4.88 kA/cm^2, which suggest that the passing of electric current reduces the apparent contact stiffness of the pure copper.

Figure 5.4 shows the variation of the contact depth with the electric current density for the indentation of the Cu-strips. For the indentations made by the indentation load less than 600 μN, the contact depth is independent of the electric current density; while, for the indentations made by the indentation load larger than or equal to 600 μN, the contact depth decreased with increasing the current density. The mechanism for such behavior is unclear.

Using the area function obtained from the indentation of quartz, we calculated the reduced contact modulus and indentation hardness from the loading-unloading curves. The dependence of the reduced contact modulus, E_r, on the indentation load is depicted in Fig. 5.5. For the electric current density less than or equal to 1.25 kA/cm^2, the reduced contact modulus is independent of the indentation load, while, for the electric current density larger than 1.25 kA/cm^2, the reduced contact modulus decreased with increasing the indentation load similar to the observation in the indentation of Zr-based metallic

glass [149] and copper [136]. When there was no electric current passing through the Cu-strips, the average reduced contact modulus was 148.1 GPa compatible with 130.7 GPa calculated from the Young's modulus of 116.5 ± 4.7 GPa given by Deng et a. [150] for the nanoindentation of Cu and Poisson's ratio of 0.33 and in accord with the result given by Yang and Zhao [147]. The reduced contact modulus of the Cu-strips with the passing of an electric current is less than that without the passing of an electric current. This result suggests that the passing of an electric current through a Cu-strip caused the decrease of Young's modulus, i.e. the Cu-strips became easily deformed elastically. It is worth of mentioning that additional indentation of the Cu-strips was performed after immediately switching off the electric circuit for an electric current density of 2.54 kA/cm^2. Both the reduced contact modulus and the apparent indentation hardness were the same as those when there was no electric current passing through the strips. For the current density larger than or equal to 3.77 kA/cm^2, it was impossible to immediately make the indentation due to the unstable state of the strips possibly from the strip shrinking during the cooling.

The dependence of the reduced contact modulus on the electric current density is depicted in Fig. 5.6 for various indentation loads. The reduced contact modulus linearly decreases with increasing electric current density for different indentation loads. This result implies the effect of electromechanical interaction on the indentation response of the Cu-strips with the passing of an electric current.

Considering the contribution of electrical-thermal-mechanical interaction to the mechanical deformation under the action of an electric current, Yang and Zhao [147] derived a semi-analytical relation between Young's modulus and electric current density as

$$E = E_0 - \beta J - \alpha J^2 \tag{5.2}$$

where E_0 is the Young's modulus of the metal at the reference temperature of T_0 (T_0 =273 K for this work), β is a parameter depending on the equilibrium distance between atoms, atomic interaction and the interaction between moving electrons and atoms, and

α is a parameter associated with Joule heating. When subjected to severed plastic deformation, both the parameters α and β are a function of local stress state. According to Eq. (5.2), the linear dependence of the reduced contact modulus on the electric current density as shown in Fig. 5.6 suggests that the contribution of Joule heating to the change of local elastic behavior is negligible. The change of local elastic deformation during the indentation was dominantly controlled by the interaction between moving electrons and atoms. From the proportionality between Young's modulus and the contact modulus, a curve-fitting of the results in Fig. 5.6 gives the value of β for each indentation load, which is listed in table 5.1. In contrast to the constant value of β for the indentation of Cu-wires with the passing of a DC electric current [147], the β value increases with increasing the indentation deformation implies the strong electromechanical interaction in the Cu-strips when there was an AC current passing the Cu-strips. The mechanism for such behavior is unclear, and it might be due to the skin effect with the current density being largest near the surface of the Cu-strips.

Figure 5.7 shows the dependence of the indentation hardness on the electric current density for various indentation loads. The indentation hardness is a linear function of the electric current density. For the indentation load less than 200 μN, the indentation hardness increased with increasing the electric current density, while, for the indentation load larger than or equal to 200 μN, the indentation hardness slightly increased with increasing the electric current density. The mechanism for the variation of the indentation hardness with the electric current density is unclear. From Fig. 5.7, one can note that the indentation hardness decreased with increasing the indentation load, demonstrating the normal indentation size effect.

Figure 5.8 shows the variation of the indentation hardness of the Cu-strips with the contact depth. The indentation hardness decreased with the increase of the contact depth for all the current densities used in the experiments. The decrease of the indentation hardness with increasing the indentation deformation has been observed in a variety of materials [151, 152]. Incorporating the concept of a scale dependence into plasticity as suggested by Ashby [151, 152], the plasticity theory has been reformulated to include the

effect of strain gradients, referred to as the theory of strain gradient plasticity [145, 153-155]. According the model of the strain gradient plasticity [145], the scale dependence of the indentation hardness can be expressed as

$$H = H_0 \sqrt{1 + \frac{1}{\rho_s b} \frac{\partial \gamma}{\partial x}} \tag{5.3}$$

Here H is the indentation hardness for the indentation depth of h, H_0 is the indentation hardness in the limit of infinite depth, b is the Burgers vector, ρ_s is the density of the dislocations that accumulate in a uniform deformation of the material, and $\partial \gamma / \partial x$ is the gradient of strain γ.

With the passing of an electric current, the interaction between moving electrons and atoms causes local lattice distortion and local strain. Electric current will generate a uniform strain field in materials of uniform cross-section area. The indentation by a sharp indenter creates surface irregularity by generating local deformation. The indentation deformation alters local structure and current distribution, which introduces local strain gradient. The strain gradient is a function of electric current density and inversely proportional to the indentation depth of h as,

$$\frac{\partial \gamma}{\partial x} = \frac{f(J)}{h} \tag{5.4}$$

Here $f(J)$ is a parameter dependent on the electric current density. Substitution of Eq. (5.4) into Eq. (5.3) yields

$$H = H_0 \sqrt{1 + \frac{f(J)}{\rho_s b} \frac{1}{h}} \equiv H_0 \sqrt{1 + \frac{\lambda}{h}} \tag{5.5}$$

with $\lambda = f(J) / (\rho_s b)$, which representing the contribution from the uniform deformation and the current-induced deformation.

Using Eq. (5.5) to fit the experimental data as given in Fig. 5.8, one obtains the values of the parameters H_0 and λ for various current densities, which are listed in table 5.2. The value of H_0 is independent of the electric current density, while the value of λ slightly decreases with increasing electric current density.

According to the finite element results given by Zhao et al. [125] for the indentation of a conducting material with simultaneous action of an electric current, the indentation deformation causes local current concentration with the maximum current density occurring at the indentation tip. The current concentration can increase the local migration rate of atoms and reduce the local strain gradient underneath the indentation, which results in the decrease of λ with increasing electric current density.

Another way of examining the effect of electric current on the indentation behavior of the Cu-strips is by analyzing the dependence of the parameter HS^2/F on the indentation load for various electric current densities. Here, S is the reduced contact stiffness as calculated from the unloading curves, and F is the indentation load. From the definitions of the indentation hardness and the relation between the reduced contact stiffness and the contact area for the contact deformation of semi-infinite elastic materials, one has [156]

$$\frac{HS^2}{F} = \frac{4\chi}{\pi} E_r^2 \tag{5.6}$$

Where χ is a constant depending on the surface profile of the indenter. Without the passage of an electric current, Eq. (5.6) indicates that the ratio of HS^2/F is only dependent on the reduced contact modulus. With the passage of an electric current, one expects that the ratio of HS^2/F will vary with the current density since the reduced contact modulus is a function of electric current density as shown in Fig. 5.5.

Figure 5.9 shows the variation of the ratio of HS^2/F with the indentation load for various current densities. For the same indentation load, the ratio of HS^2/F decreases with increasing the electric current density in accord with the current-induced decrease of the reduced contact modulus of the Cu-strips. For the current density less than or equal to 1.25 kA/cm^2 the ratio of HS^2/F is relatively independent of the indentation load, suggesting weak electromechanical interaction for electric current of low current density. Without the passage of an electric current, the constant value of the ratio of HS^2/F is

consistent with the observations by Joslin and Oliver [156] for the indentation of ASTM 136-79 Ti-6A1-4V and Yang et al. [149] for the indentation of $Zr_{57}Ti_5Cu_{20}Ni_8Al_{10}$ bulk metallic glass. For the current density larger than 1.25 kA/cm^2, the ratio of HS^2/F decreases with increasing the indentation load which demonstrates the local softening due to electromechanical interaction.

Zhang and his co-workers [157, 158] had analyzed the effect of apparent surface stress and surface roughness on the indentation depth-dependent hardness. When there is an electric current passing through the Cu-strips, one would expect that such behavior may also occur in the indentation of Cu-strips due to the field effect on the apparent surface stress and surface roughness. However, this requires the characterization of the dependence of the apparent surface stress and surface roughness on electromechanical interaction, which will be studied in the future.

5.4 Summary

Electromechanical interaction plays an important role in determining the electrical and mechanical integrity of electronic devices and systems. Large electric current density through electronic interconnects can introduce strong electromechanical interaction, which can cause structural distortion and damage. Using the nanoindentation technique, the effect of AC electric current on the indentation behavior of Cu-strips was studied for the current densities ranging from 1.25 to 4.88 kA/cm^2. The reduced conduct modulus decreased with increasing electric current density and was a linear function of the electric current density. Such behavior suggests that the electromechanical interaction due to the momentum exchange between high-speed electrons and atoms played an important role in controlling the elastic indentation of Cu-strips when there was an electric current passing through the Cu-strips. The indentation hardness decreased with increasing the indentation deformation, demonstrating the normal indentation size effect. Using the model of strain gradient plasticity, the effect of the electric current density on the strain gradient underneath the indentation was analyzed. For the same indentation depth, the strain gradient decreased slightly with increasing the electric current density.

Table 5.1 Variation of the β value with the indentation load

Indentation load (μN)	100	200	400	600	800	1000	1300	1600
β (MPa/(kA/cm^2))	2.72	5.69	7.51	10.21	12.73	14.79	15.48	17.05

Table 5.2 Variation of the H_0 and λ values with the electric current density

Electric current density (kA/cm^2)	0	1.25	2.54	3.77	4.88
H_0 (GPa)	1.64	1.73	1.74	1.75	1.78
λ (nm)	112.79	91.9	92.88	86.84	82.69

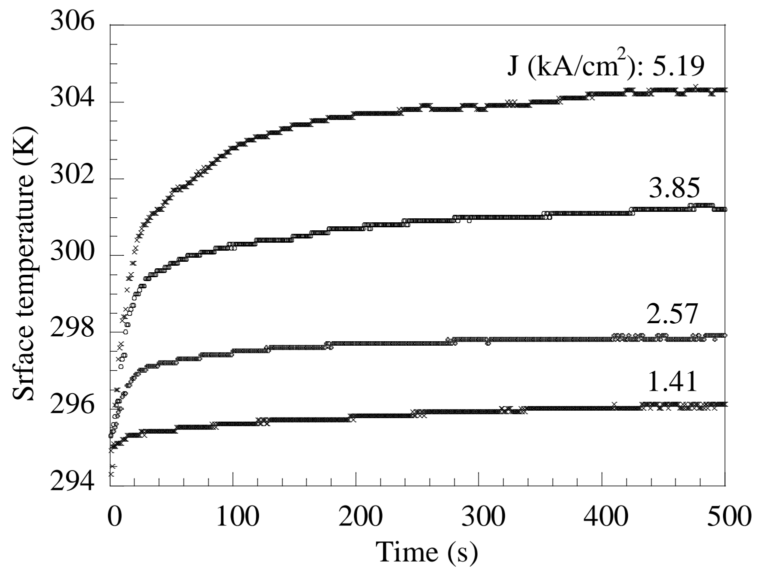

Figure 5.1 Temporal evolution of the surface temperature at the center of the Cu-strips for several current densities (*J*: electric current density)

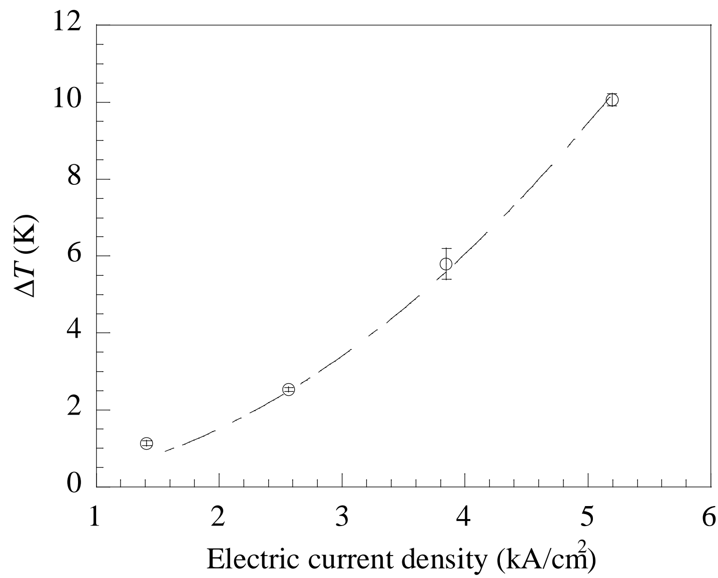

Figure 5.2 Dependence of the surface temperature rise on the electric current density

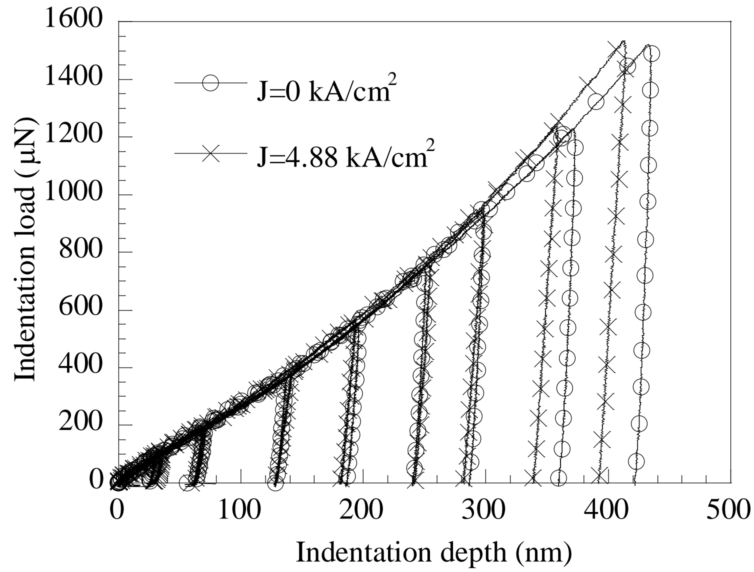

Figure 5.3 Typical indentation loading-unloading curves for the indentation of the Cu-strips with and without the passing of an electric current (J= 0 kA/cm^2, and J=4.88 kA/cm^2)

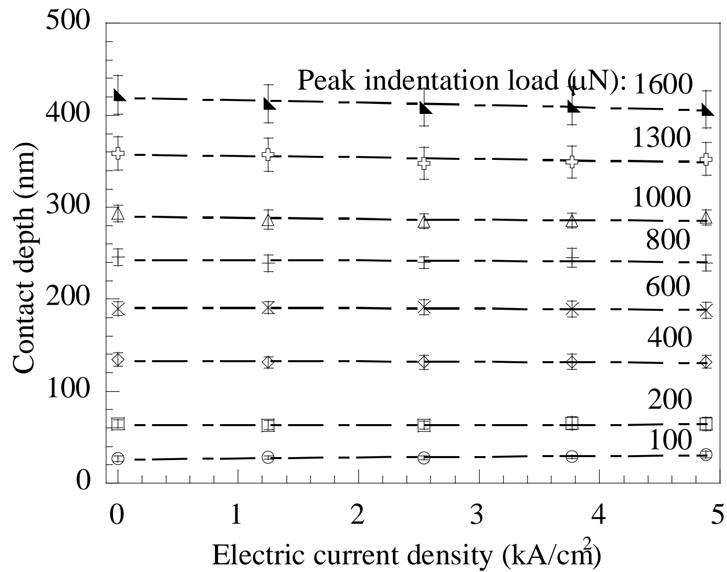

Figure 5.4 Variation of the contact depth on the electric current density for different indentation loads

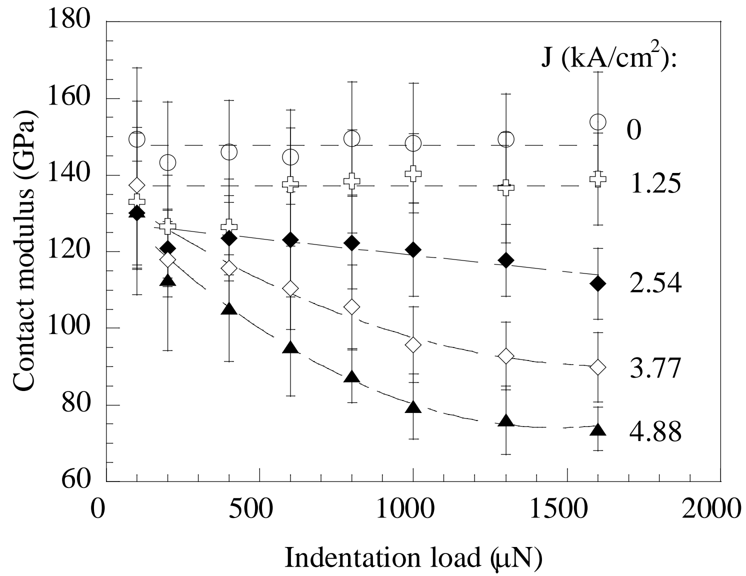

Figure 5.5 Variation of the contact modulus with the indentation load for various current densities

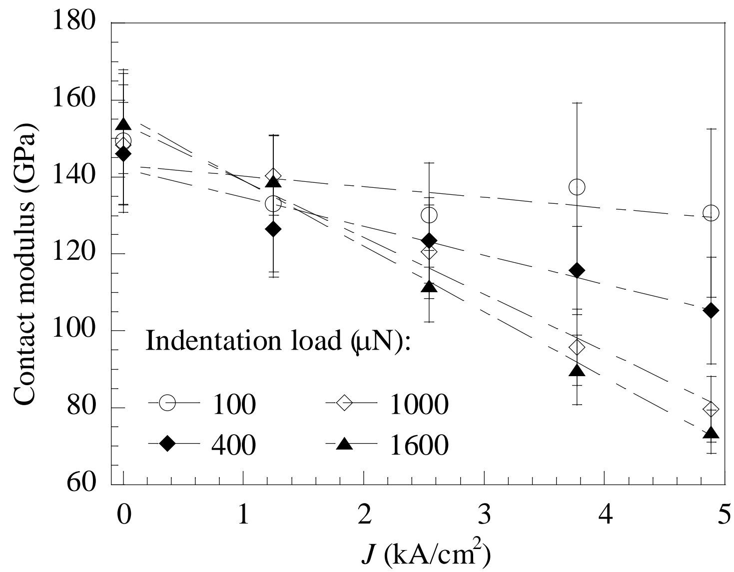

Figure 5.6 Dependence of the contact modulus on the electric current density for several indentation loads

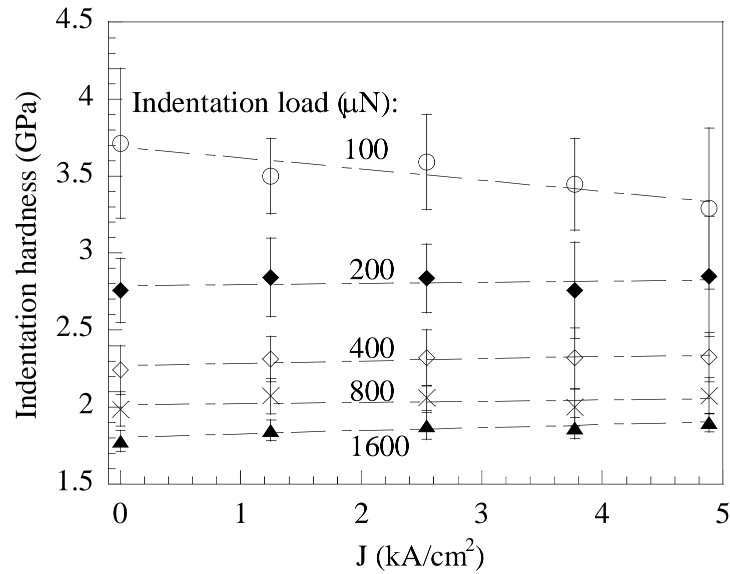

Figure 5.7 Dependence of the indentation hardness on the electric current density for several indentation loads

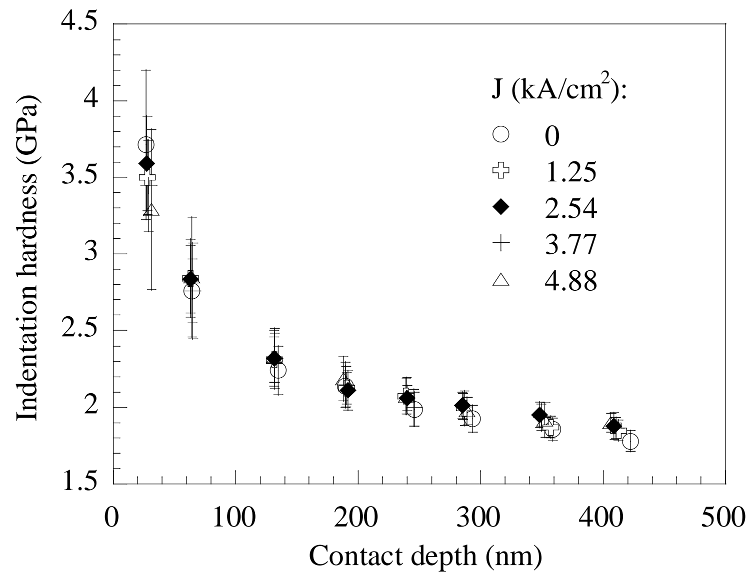

Figure 5.8 Variation of the indentation hardness with the contact depth for various current densities

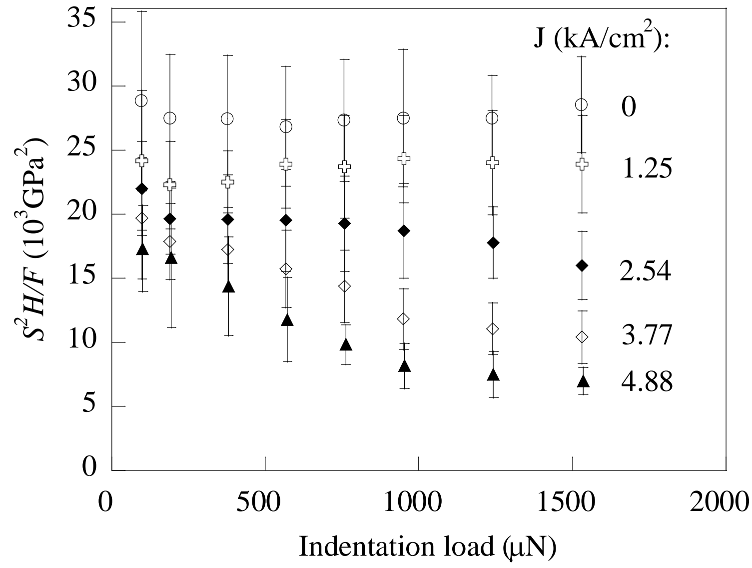

Figure 5.9 Variation of the ratio of HS^2/F with the indentation load for various current densities

Chapter 6 Electric current effect on the nanoindentation behavior of tin*

6.1 Introduction

Tin-based alloys have been extensively used in electric interconnects to provide electrical and mechanical support in microelectronic devices and systems. In contrast to structural materials, these materials experience thermomechanical deformation due to the passing of electric current in an operating electronic device. The demand for high speed and great performance of electronic devices and systems has led to the miniaturization of electronics and a significant increase in electric current. This requires electronic interconnects to carry electric current of high current density which results in electrical-thermal-mechanical interaction. The electrical-thermal-mechanical interaction has placed great challenges on understanding the effect of electric current on the mechanical deformation of electric interconnects in order to improve the performance and reliability of electronic assembly and packaging.

The mechanical deformation of materials under the action of electric current depends on local electrical-thermal-mechanical interaction. Ye et al. [46] used Moiré interferometry to measure the displacement change in Sn95.5/Ag4/Cu0.5 alloy under the action of electric current and observed large deformation in solder joint at high electric current density (10 kA/cm^2). Xu et al. [159] found that the electric current-induced back stress together with electron wind force caused the movement of indentation markers in SnAgCu solder joints. Nah et al. [160] evaluated the shear behavior of flip-chip solder joints before and after the pass of electric current and found that the electric current had a significant effect on the shear failure of the flip-chip solder joints. The failure mode changed from fracture inside the solder joint before the action of electric current to

---

*Reproduced with permission from Guangfeng Zhao, Ming Liu and Fuqian Yang, Acta Materialia, 2012. 60(9): p. 3773-3782. Copyright 2012 Acta Materialia Inc.

interfacial failure on the cathode interface after the pass of electric current. Ren et al. [161] observed that the coupling effect of electric current and tensile stress caused a ductile-to-brittle transition during the tensile test of Sn95.5Ag3.8Cu0.7 alloy. Kumar et al. [162] found that the pass of an electric current through Sn-3.5Ag solder caused brittle failure of solder joints. Chen and Yang [133, 134, 148] studied the effect of direct electric current on the creep deformation of Pb, Sn, and Sn60Pb40 alloy and found that the apparent activation energy for the steady state creep decreased with increasing electric current density. Zhu et al. [118] investigated the effect of current crowding on stress relaxation of pure tin and found that the current stressing accelerated the stress relaxation. Most of the studies were focused on the current effect on the tensile behavior and creep deformation of Sn-based alloys. There is little study addressing the effect of electric current on local mechanical deformation of Sn and Sn alloys, which determines the structural durability of electronic interconnects.

Nanoindentation is a localized testing technique, which has been used to characterize the reduced contact modulus and indentation hardness of materials of small volumes and has provided numerous insights into the fundamentals controlling localized deformation of materials. Few studies have paid attention to the evaluation of the effect of electrical-thermal-mechanical interaction on the indentation behavior of materials. In this work, we investigate the indentation deformation of tin strips when there is an electric current passing through the strips. The effect of the electric current density is examined on Joule heating, the reduced contact modulus and indentation hardness. The dependence of the indentation hardness on electric current density is also discussed.

6.2 Electrothermal analysis

Consider a conducting thin film deposited on an insulated substrate. The film thickness of t is much smaller than the film length of L, and the temperature variation in the thickness direction is expected to be negligible. Thus, a one-dimensional electrothermal analysis is adopted. For a DC electric current of I passing through the specimen, the steady state thermal conduction in the specimen can be described by the following partial differential equation as

$$\frac{d}{dx}\left(kA\frac{dT}{dx}\right)+\frac{\rho_e I^2}{A}-h_c c(T-T_\infty)=0 \tag{6.1}$$

where T is local temperature in the strip, k is the specific heat, ρ_e is the electric resistivity, I is electric current intensity passing through the strip, h_c is the heat transfer coefficient (assumed independent of T), A is the cross-sectional area of the strip,c is the summation of the lengths of side surfaces exposing to air, and T_∞ is the temperature of the environment (i.e. the temperature suitably far from the surface). The second term in Eq. (6.1) represents the heat released from Joule heating, and the third term is the heat loss through the side surfaces.

The boundary conditions at the ends of the strip is

$$T=T_0 \qquad \text{at } x=\pm L/2 \tag{6.2}$$

where T_0 is the temperature at the ends of the strip. The solution of Eq. (6.1) is

$$T=\left(T_0-T_\infty-\frac{\rho_e I^2}{Ach_c}\right)\frac{\cosh\omega x}{\cosh(\omega L/2)}+T_\infty+\frac{\rho_e I^2}{Ach_c} \tag{6.3}$$

with $\omega^2=ch_c/kA$ .At the center of the strip, the temperature rise reaches the maximum as

$$T=\left(T_0-T_\infty-\frac{\rho_e I^2}{Ach_c}\right)\frac{1}{\cosh(\omega L/2)}+T_\infty+\frac{\rho_e I^2}{Ach_c} \tag{6.4}$$

The temperature rise is a linear function of $1/\cosh(\omega L/2)$, which suggests that the longer the strip is, the smaller is the spatial increase rate of local temperature. For $T_0=T_\infty$, Eq. (6.3) gives

$$T-T_\infty=\frac{\rho_e I^2}{Ach_c}\left(1-\frac{\cosh\omega x}{\cosh(\omega L/2)}\right) \tag{6.5}$$

The temperature rise is proportional to the electric current intensity (electric current density).

6.3 Experimental

Pure tin bars used in this study were obtained from McMaster-Carr (Chicago, IL). Tin blocks were machined from the tin bars and then rolled into strips of 0.3 mm in thickness which was cut into thin strips of 3~4 mm in width and ~10 cm in length. The thin strips were then heat-treated in air at 347 K for half hour to release the residual stresses created by machining and rolling and to obtain a homogeneous microstructure before being attached to the surface of a glass slide. The average grain size was ~60 μm. A small tensile force was applied to the strips during the sample mounting to avoid possible slipping of the tin strips on the glass slide. The tensile force and mechanical pressing at the contact ends between the strips and the glass slide caused intimate contact between the strips and the glass slide, which prevented the possible indentation-induced sliding motion of the strips. The tin strips then were mechanically ground and polished parallel to the axial direction, and the cross-section areas of the polished samples were in the range of 1.96×10^{-3} to 2.29×10^{-3} cm^2. Using the current control, a direct electric current was passed through the strips before performing the indentation test and the electric current density was maintained a constant value during the indentation test. The electric current densities were in the range of 993.1 to 4087.9 A/cm^2. During the passing of an electric current through the Sn-strips, the surface temperature of the strips was measured using a thermocouple.

The nanoindentation tests were performed in a Hysitron TriboScope (Minneapolis, MN) attached to a Quesant (Agoura Hills, CA) atomic force microscope (AFM), after reaching thermal equilibrium with continuous passing of an electric current. A non-conducting diamond NorthStar cubic indenter with a nominal tip radius of ~40 nm (Minneapolis, MN) was used. The machine compliance was calibrated to be 1.0 nm/mN. Constant loading and unloading rates were used in the indentation tests with an intermediate pause of 20s between the loading phase and the unloading phase to avoid the effect of the indentation creep on the measurement of the reduced contact modulus. The

indentation load used in the tests was in the range of 50 μN to 200 μN. For each loading and electric current condition, at least fifteen indents were performed. The indentation depth and indentation load were used to calculate the reduced contact modulus and indentation hardness.

6.4 Results and discussion

6.4.1 Electrothermal curves

During the electrothermal test, the electric current intensity was maintained constant. The local surface temperature at the center of the Sn-strips was measured at room temperature. Figure 6.1 shows the variation of the surface temperature of the Sn-strips with time. The surface temperature initially increased with time and reached a constant value following a transient state. The time to reach local thermal equilibrium was less than 200 s. The equilibrium surface temperature increased with increasing the current density.

Figure 6.2 depicts the dependence of the surface temperature rise ($\Delta T = T - T_\infty$) on the current density. The surface temperature rise increased with the crease of the electric current density due to the release of Joule heat.The highest temperature was 48.7 K for an electric current density of 4087.89 A/cm^2. Using a curve-fitting, the surface temperature rise can be expressed as

$$\Delta T = 2.965 \times 10^{-6} J^2 \tag{6.6}$$

which is proportional to the square of the electric current density in accord with Eq. (6.5) for the experimental conditions. This result suggests that the temperature at both ends of the Sn-strips was approximately equal to the ambient temperature. The temperature rise is controlled by the Joule heating due to the passing of an electric current through the Sn-strips.

6.4.2 Electric nanoindentation

During the indentation test, the electric current intensity was maintained constant. The loading-unloading curves are shown in Fig. 6.3a for the indentation of the Sn-strips without the passing of an electric current. For comparison, the corresponding curves with the passing of an electric current density of 4087.89 A/cm^2 are also shown in Fig. 6.3b. Generally, there is no significant deviation in the loading curves for different indentation loads under each individual current condition. For the indentation of tin without the passing of an electric current, pop-in events first initiated at the indentation load of ~90 μN or the indentation depth of 110 nm with the pop-in depth of ~10 nm and multiple pop-in events occurred for large indentation load. Such a behavior might be due to the nucleation/activation of dislocations during nanoindentation [62, 163-165] or grain boundary sliding.

It is known that the theoretical stress for the occurrence of plastic deformation can be approximated as $\tau_c \approx G/10$ [166], which corresponds to the critical stress for the initiation of dislocation. Here, G is the shear modulus of the material. According to the Tresca criterion and the model of Hertzian contact for the indentation of a semi-infinite elastic material, the maximum shear stress, $\tau_{\max}$, underneath a spherical indenter can be expressed as [167]

$$\tau_{\max} = 0.465 \frac{F}{\pi a^2} = 0.465 \frac{4E^*}{3\pi} \sqrt{\frac{h}{R}} \tag{6.7}$$

where F is the indentation force, a is the contact radius, h is the indentation depth, and R is the radius of the indenter tip. The effective elastic modulus E^* is calculated from Young's modulus E and Poisson's ratio ν of the sample and the values of the indenter material (diamond: E_i=1141 GPa and ν_i=0.07) as

$$\frac{1}{E^*} = \frac{1-\nu^2}{E} + \frac{1-\nu_i^2}{E_i} \tag{6.8}$$

Thus the pop-in depth δ_p for the activation of an immobile dislocation or the initiation of a dislocation during an indentation by a rigid spherical indenter can be estimated as

$$\delta_p \approx \frac{R}{21.62}\left[\frac{3\pi}{4}\frac{E}{2(1+\nu)}\left(\frac{1-\nu^2}{E}+\frac{1-\nu_i^2}{E_i}\right)\right]^2 \tag{6.9}$$

The total number of the activated dislocationsfor a pop-in event can approximately calculated from the dislocation density of ρ and the indentation depth as [163]

$$N \approx \pi\rho a^2 = \pi\rho R h \tag{6.10}$$

From Eqs. (6.9) and (6.10), the total pop-in depth, h_T, for an pop-in event is

$$\delta_T = N\delta_p \approx \frac{\pi\rho R^2 h}{21.62}\left[\frac{3\pi}{4}\frac{E}{2(1+\nu)}\left(\frac{1-\nu^2}{E}+\frac{1-\nu_i^2}{E_i}\right)\right]^2 \tag{6.11}$$

Using the mechanical properties of polycrystalline Sn (*E*=43.6 GPa at room temperature of 298 K [168, 169] and ν =0.36), one obtains the pop-in depth of 1.1 nm for the activation of a dislocation during the indentation of tin by a spherical indenter of 40 nm in radius. From Fig. 3a, one obtains $\delta_T \approx 10$ nm at $h \approx 110$ nm for the indentation of Sn without the pass of an electric current. Substitution of $\delta_T \approx 10$ nm and $h \approx 110$ nm into Eq. (6.11) yields the dislocation density of 6.58×10^{10} cm^{-2}, which is much larger than that in severely deformed metals. This suggests that the activation or initiation of dislocations cannot be solely responsible for the occurrence of the pop-in events. It is likely the combination of the activation or initiation of dislocations and grain boundary sliding that causes the pop-in events.

For the indentation of Sn with the pass of an electric current of 4087.89 A/cm^2, the loading curves with the indentation load less than 125 μN deviated away those without the pass of electric current, while they generally coincided with the loading curves for the

indentation load larger than 125 μN. Such a behavior is likely due to the electrothermal interaction, which causes surface softening resulting in relatively deep indentation for the small indentation loads when there is an electric current passing through the Sn-strips. For large indentation loads, the localized mechanical behavior of materials and the electromechanical interaction played important roles in controlling the indentation deformation. In contrast to the indentation of the Sn-strips without the pass of electric current, no observable pop-in event was present in the loading curves. The pass of an electric current of high density inhibited the occurrence of the pop-in events. For the same indentation load, the slopes of the unloading curves for the indentation of the Sn-strips with the passing of an electric current of the current density of 4087.89 A/cm^{2}are less than those without the passing of an electric current. This trend suggests that the passing of electric current likely caused the change of the apparent contact stiffness of the Sn-strips.

Figure 6.4 shows the variation of the contact depth with the electric current density for the indentation of the Sn-strips. For the indentations made the indentation load less than 100 μN, the contact depth increases with increasing the electric current density, while, for larger indentation load than 75 μN, the contact depth is independent of the current density. For small indentation loads, the indentation depth is small and the indentation deformation is determined by the near-surface properties in which the electrical-thermal-mechanical interaction plays a relatively important role in controlling the local mechanical response of materials. For large indentation loads, the role of the electrothermal interaction becomes negligible for deep indentation and the indentation deformation is controlled by the mechanical behavior of materials and the scattering interaction between moving electrons and lattice atoms. This result suggests that the electrothermal interaction is one of the dominant factors controlling the indentation behavior of materials for shallow indentations.

Using the area function obtained from the indentation of quartz, we can calculate the reduced contact modulus and indentation hardness from the loading-unloading curves. The dependence of the reduced contact modulus, E_r, on the indentation load with a

holding time of 20 s is depicted in Fig. 6.5. For the same electric current density, the reduced contact modulus slightly decreases with increasing indentation load, similar to the observation in the indentation of Zr-based metallic glass [170] and copper [171, 172]. When there was no electric current passing through the Sn-strips, the reduced contact modulus decreased from an average value of 82.5 GPa for the indentation load of 50 μN to an average value of 57.5 GPa for the indentation load of 200 μN, which is slightly higher than 43.6 GPa of polycrystalline Sn. Such a difference likely is due to the anisotropic effect of tetragonal Sn, which has different elastic constants varying from 87.0 GPa to 22.6 GPa for different crystal orientations. The reduced contact modulus of the Sn-strips with the pass of an electric current is less than that without the pass of an electric current. This result suggests that the electrical-thermal-mechanical-interaction causes the decrease of Young's modulus of the Sn-strips, and the Sn-strips can be easily deform elastically with the pass of an electric current.

The dependence of the reduced contact modulus on the electric current density is depicted in Fig. 6.6 for three indentation loads. The reduced contact modulus decreases with increasing electric current density for the same indentation load, strongly reflecting the effect on the electrical-thermal-mechanical interaction on the near-surface elastic behavior of the Sn-strips. For the electric current density of 4087.89 A/cm^2, there is no significant difference of the reduced contact modulus for the indentation loads used in the work. This results suggests that the dependence of the reduced contact modulus on the electric current density can be divided into two regions – one is mainly controlled by the electrical-thermal-mechanical interaction including local Joule heating and the momentum exchange between moving electrons and lattice atoms for large electric current density and the other is controlled by the electrothermal interaction and local mechanical deformation for small electric current density.

It is known that the temperature dependence of Young's modulus of polycrystalline Sn can be expressed as [169]

$$E = 76.087 - 0.109T \text{ (GPa)} \tag{6.12}$$

which does not consider the effect of the near-surface deformation. To consider the contribution of the near-surface deformation and the local temperature rise of Eq. (6.6), one can modify Eq. (6.12) as

$$E_r = \alpha - \beta J^2 \tag{6.13}$$

Here α is the reduced contact modulus in the unit of GPa for J=0 A/cm^2, and β in the unit of GPa/(kA/cm^2) is a load-dependent constant related to Joule heat. Obviously, the results for J=4087.89 A/cm^2 cannot be described by Eq. (6.13). One needs to consider the contribution of the momentum exchange between moving electrons and lattice atoms to the indentation deformation of Sn for large electric current density.

Figure 6.7 shows the curve-fitting of the experimental results for the electric current density less than4087.89 A/cm^2. The quadratic relation given in Eq. (6.13) is in accord with the experimental results. The curve-fitting of the experimental results gives (α, β) as (82.12, 6.92), (66.55, 5.97), and (57.39, 5.77) for the indentation loads of 50, 125, and 200 μN, respectively. This result suggests that the parameter of α decreases with increasing the indentation loading agreement with the results shown in Fig. 6.5 and the parameter of β slightly decreases with increasing the indentation load for the experimental conditions. Both parameters of α and β are load-dependent.

Figure 6.8 shows the dependence of the indentation hardness on electric current density for various indentation loads. For the indentation load less than 175 μN, the indentation hardness first increases with increasing the electric current density, reaches the maximum at the current density of 1.75 kA/cm^2, and then decreases with increasing the electric current density. For the indentation load larger than or equal to 175 μN, the indentation hardness is relatively independent of the electric current density. The mechanism for the variation of the indentation hardness with the electric current density is unclear. From Fig. 6.8, one can note that, for the electric current density less than or equal to 2.80 kA/cm^2, the indentation hardness decreases with increasing the indentation load, demonstrating the normal indentation size effect. However, the indentation hardness

is independent of the indentation load for the current density of 4.09 kA/cm^2. The decrease of the indentation hardness with increasing the current density is likely due to the effect of strain gradient and local creep deformation. As shown in Fig. 6.3, there exists creep deformation in the indentation deformation during the holding period of 20 s. The indenter continuously penetrated into the Sn-strips under the action of the constant indentation load. It can be expected that the creep deformation also occurred during both the loading and unloading phases. Since the penetration depths at the holding period for different indentation loads can be treated approximately as the same, the strain gradient might play an important role in the nanoindentation of the Sn-strips.

Figure 6.9 shows the variation of the apparent indentation hardness of the Sn-strips with the contact depth. The indentation hardness decreases with the increase of the contact depth for the current density larger than or equal to 2.80 kA/cm^2, as expected from Fig. 6.8. According to the model of the strain gradient plasticity proposed by Nix and Gao [173], the geometrically necessary dislocations are created to cause permanent shape change at the surface and the statistically stored dislocations resist the continuous penetration of the indentation. The depth dependence of the indentation hardness can be expressed as [173]

$$H = H_0\sqrt{1+\frac{h^*}{h}} \tag{6.14}$$

here H is the indentation hardness for the indentation depth of h, H_0 is the indentation hardness in the limit of infinite depth, and h^* is a characteristic length that depends on the shape of the indenter, the shear modulus and H_0. In Eq. (6.14), the term of $1/h$ is proportional to the density of the geometrically necessary dislocations. The parameters of H_0 and h^* are dependent on the shear modulus of the material as

$$H_0 = \lambda_1 G b\sqrt{\rho_s} \tag{6.15}$$

$$h^* = b\lambda_2^2 \tan^2\theta \left(\frac{G}{H_0}\right)^2 \tag{6.16}$$

Here, λ_1 and λ_2 are two constants depending on the crystal structure, b is the Burgers vector, θ is the angle between the surface of indenter and the surface of specimen, and ρ_s is the density of the statistically stored dislocations. Substitution of Eq. (6.15) into Eq. (6.16) gives

$$h^* = \frac{\tan^2\theta}{b\rho_s}\left(\frac{\lambda_2}{\lambda_1}\right)^2 \tag{6.17}$$

The characteristic length is proportional to the reciprocal of the density of the statistically stored dislocations.

Using Eq. (6.14) to fit the experimental results as shown in Fig. 6.9, one obtains the parameters of H_0 and h^* for various current density, which are listed in table 6.1. The value of H_0increases with increasing electric current density, while the value of h^* decreases with increasing electric current density. From Eq. (6.17), one can conclude that the decrease of h^* with increasing electric current density is due to the increase of the density of the statistically stored dislocations. It is known that the density of the statistically stored dislocations does not change with the indentation. Thus, the increase of the density of the statistically stored dislocations is mainly controlled by the electrical-thermal-mechanical interaction when there is an electric current passing through the Sn-strips. The pass of an electric current in the Sn-strips introduces plastic deformation through the electrical-thermal-mechanical interaction between moving electrons and lattice atoms, which leads to the increase of the density of the statistically stored dislocations and H_0.

From Eqs. (6.15) and (6.16), one has

$$H_0\sqrt{h^*} = \sqrt{b}\lambda_2 G \tan\theta \tag{6.18}$$

The parameter $H_0\sqrt{h^*}$ is proportional to the shear modulus of the material. The calculated values of $H_0\sqrt{h^*}$ is also listed in table 6.1, which decreases with increasing the electric current density. This trend suggests that the shear modulus of the Sn-strips decreases with increasing the electric current density. It is known that the shear modulus is proportional to Young's modulus of material, which is proportional to the reduced contact modulus. The decrease of the shear modulus with the electric current density is qualitatively in accord with the reduced contact modulus measured from the unloading curves.

It is worth of mentioning that additional indentation of the tin strips was performed after immediately switching off the electric circuit for the electric current density less than and equal to 1.75 kA/cm^2. The reduced contact modulus was slightly larger than that with the pass of electric current and the indentation hardness was slightly smaller than that with the pass of electric current. For the current density larger than 1.75 kA/cm^2, it was impossible to make indentation due to the unstable state of the strips possibly from the wire shrinking during the cooling.

6.5 Summary

Electrical-thermal-mechanical interaction determines the mechanical response of a conducting material when there is an electric current passing through the material. Electric current of large electric current density can cause strong interaction between moving electrons and lattice atoms and lead to structural degradation. Using the nanoindentation technique, the effect of electric current on the indentation deformation of Sn-strips was studied for the current densities ranging from 993.05 to 4087.89 A/cm^2. The experimental results showed that both the reduced contact modulus and indentation hardness decreased with increasing electric current density. For the current density less than 4087.89 A/cm^2, the decrease of the reduced contact modulus with the electric current density was controlled by the Joule heating due to the electrothermal interaction. A simple relation was proposed to describe the dependence of the reduced contact modulus on the electric current density. For the current density of4087.89 A/cm^2, the

decrease of the reduced contact modulus with the electric current density was due to the electrothermal interaction and the momentum exchange between moving electrons and lattice atoms and the reduced contact modulus becomes relatively independent on the indentation load.

The indentation hardness also decreased with increasing the indentation load, which showed the normal indentation size effect. The strain gradient theory as proposed by Nix and Gao was used to explain the indentation size effect. It turns out that both the indentation hardness in the limit of infinite depth and the characteristic length were dependent on the electric current density. The value of h^* decreases with increasing electric current density, indicating that the pass of an electric current caused the increase of the density of the statistically stored dislocations. The increase of H_0 with the increase of the electric current density was due to the electrical-thermal-mechanical interaction, which caused the decrease of the elastic modulus and the increase of the density of the statistically stored dislocations. Using the values of h^* and H_0, we found that the shear modulus of the Sn-strips decreased with increasing the electric current density qualitatively in accord with the decrease of the reduced contact modulus as measured from the unloading curves.

Table 6.1Variation of the H_0 and h^* values with the electric current density

Electric current density (kA/cm^2)	0	0.99	1.75	2.34	2.80	4.09
H_0 (GPa)	0.09	0.11	0.10	0.13	0.18	0.27
h^* (nm)	2622.7	1602.1	2317.05	928.31	381.34	24.51
$H_0\sqrt{h^*}$ (GPa$\sqrt{\text{nm}}$)	4.61	4.40	4.81	3.96	3.52	1.34

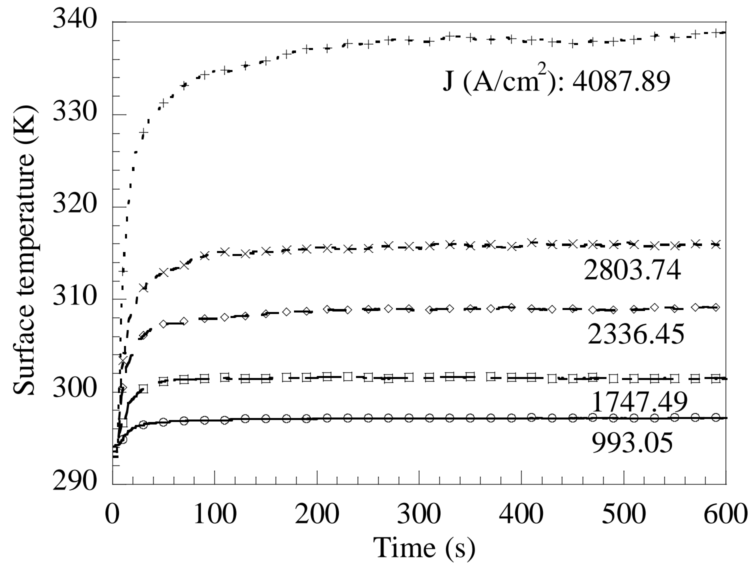

Figure 6.1 Temporal evolution of the surface temperature at the center of the Sn-strips for several current densities (*J*: electric current density)

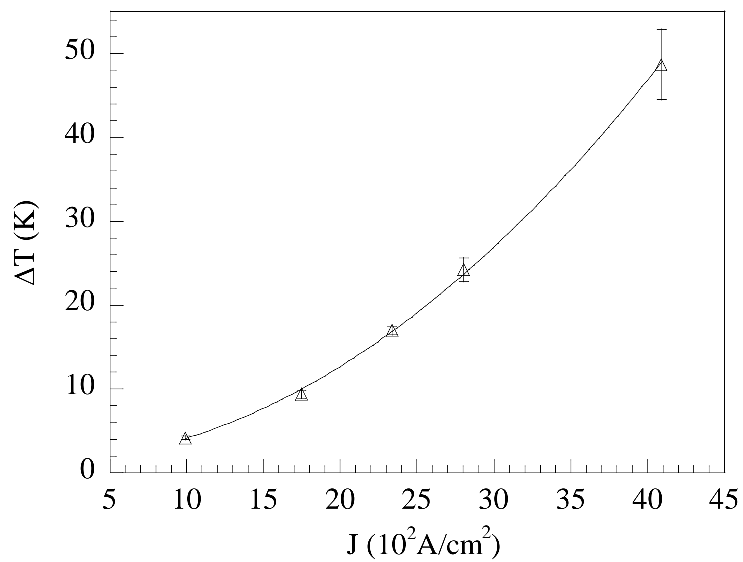

Figure 6.2 Dependence of the surface temperature rise on the electric current density

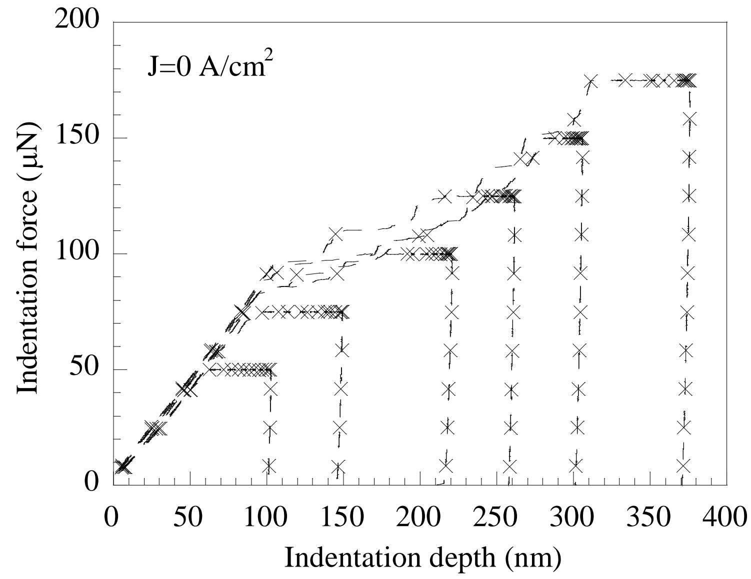

(a)

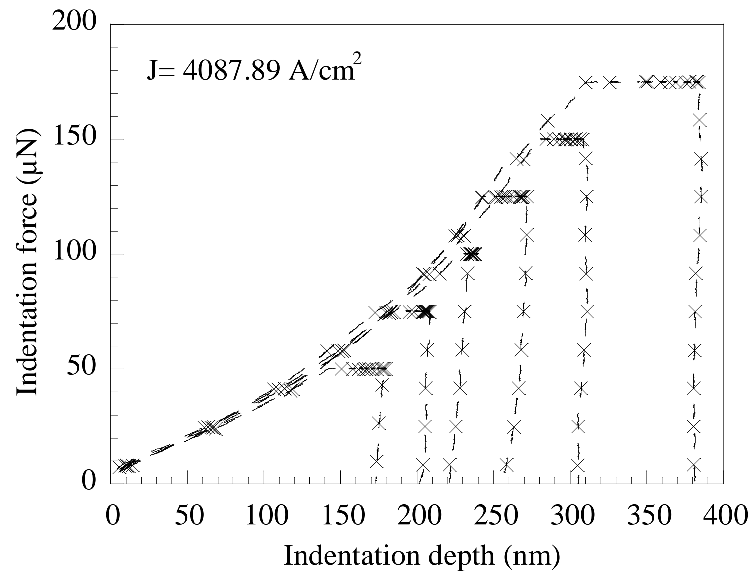

(b)

Figure 6.3 Load-displacement curves of the Sn-strips; a) without the pass of an electric current, and b) with the pass of an electric current of 4087.89 A/cm^2

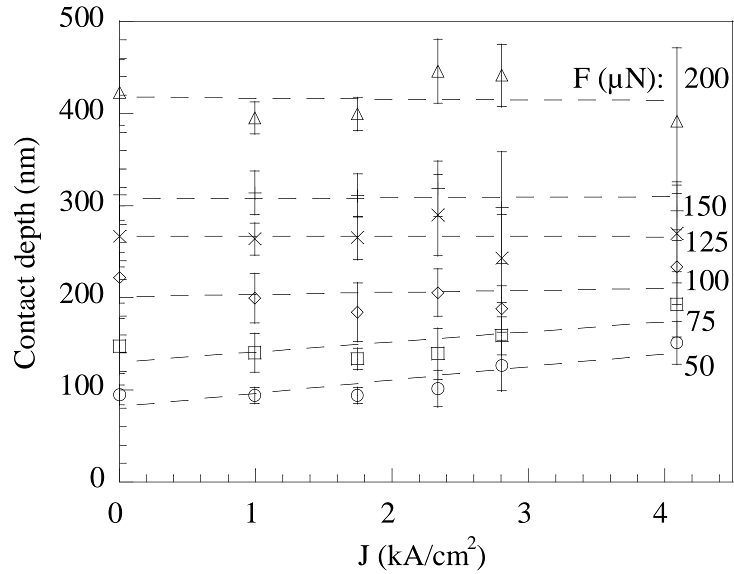

Figure 6.4 Variation of the contact depth with the electric current density for various indentation loads

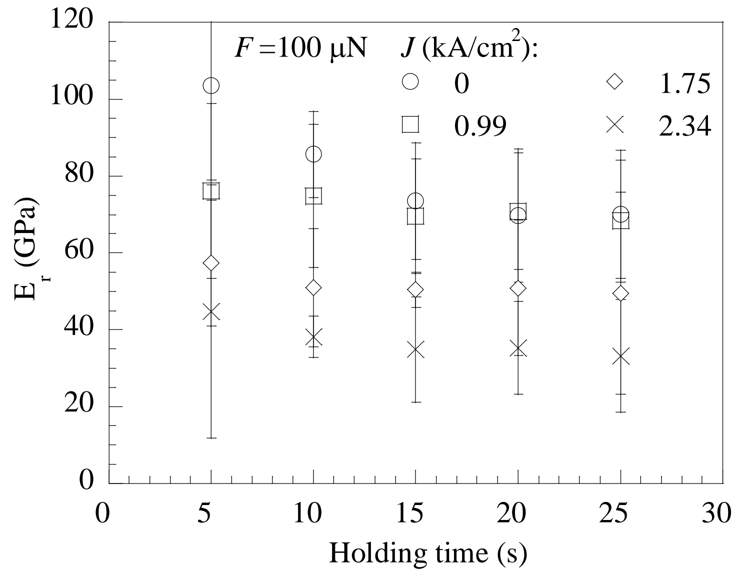

Figure 6.5 Dependence of the contact modulus on the holding time for the indentation load of 100 μN and different electric current densities

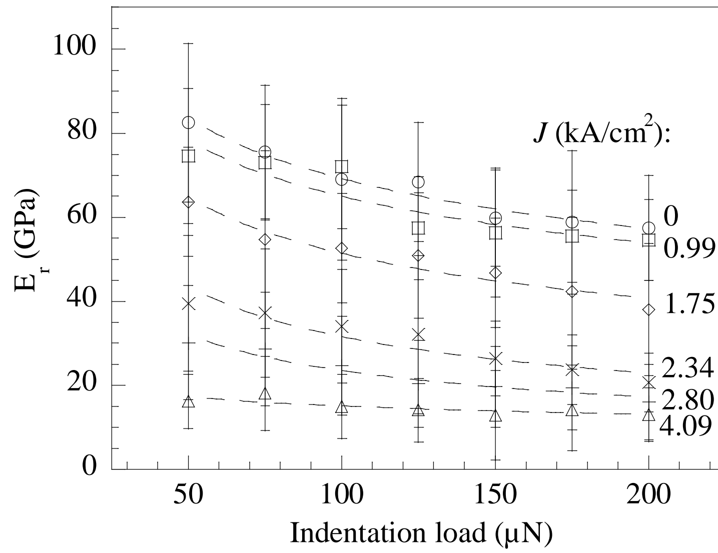

Figure 6.6 Variation of the contact modulus with the indentation load for various current densities

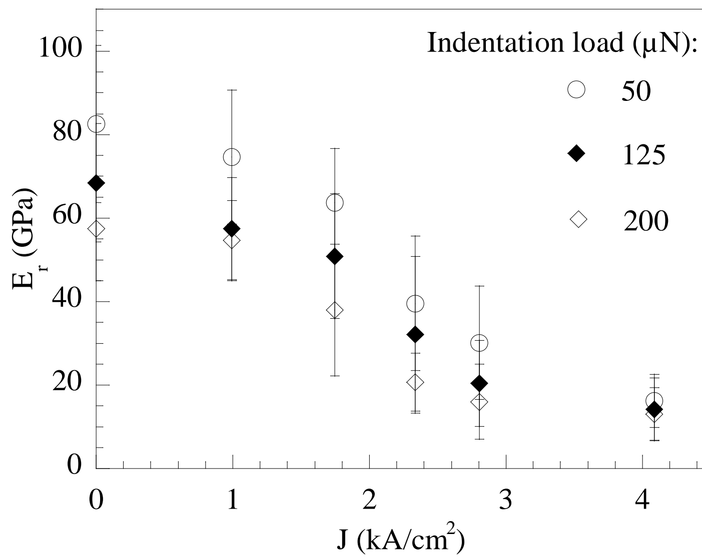

Figure 6.7 Dependence of the contact modulus on the electric current density for three indentation loads

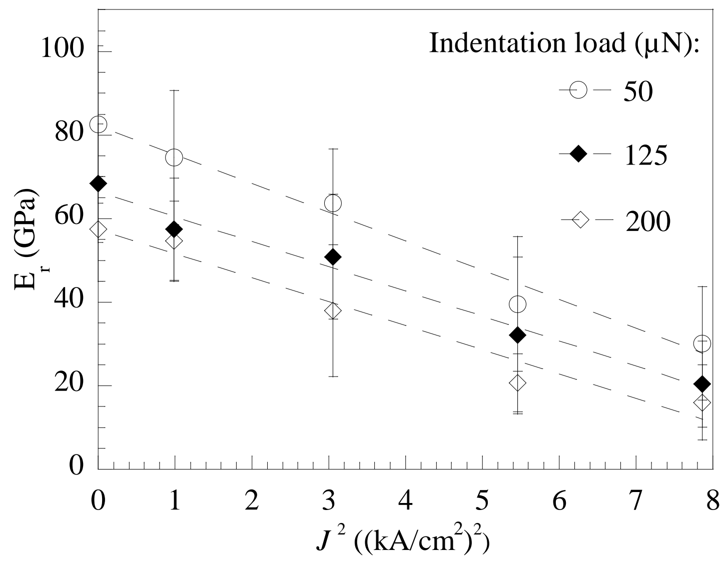

Figure 6.8 Curve-fitting of the contact modulus as a function the electric current density for three indentation loads (J<4.09 kA/cm^2)

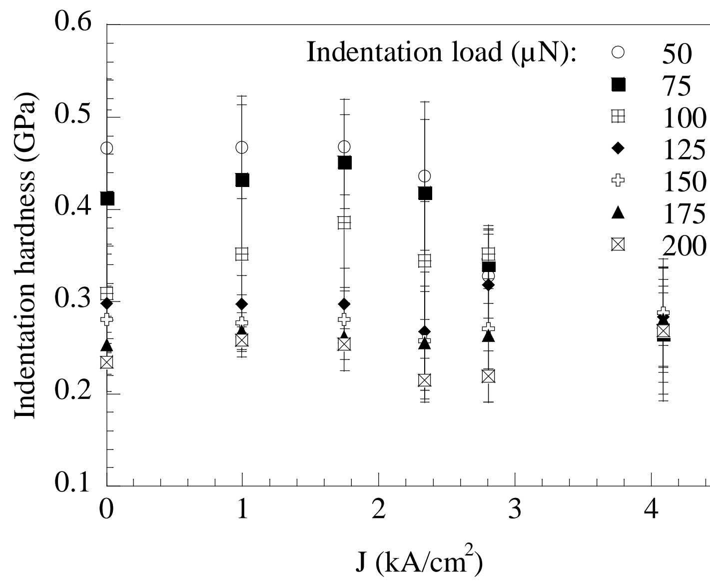

Figure 6.9 Dependence of the indentation hardness on the electric current density for various indentation loads

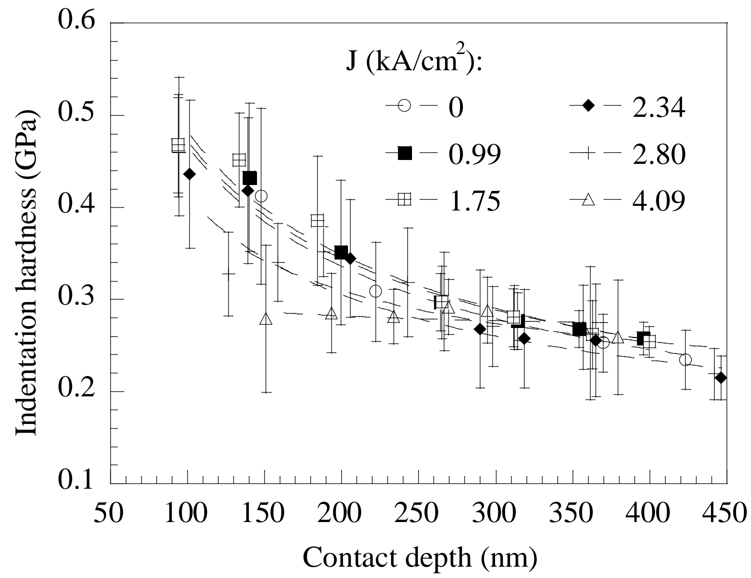

Figure 6.10 Variation of the indentation hardness with the contact depth for various current densities

Chapter 7 Effect of DC current on the tensile creep of pure tin

7.1 Introduction

Tin (Sn) and tin-based alloys have excellent physical properties, such as good conductivity, corrosion resistance, and low melting point, which make them important electronic and structural materials in electronic devices and systems. Currently, a relatively large number of Sn-based alloys has been proposed [16, 19] for the applications in microelectronic packaging. It is known that electronic interconnects are constantly subjected to the passage of electric currents of high current densities, which introduces electrical-thermal-mechanical interaction due to Joule heating [174-176]. This interaction can cause a change in local temperature and result in the time-dependent plastic deformation.

There are several reports studying the effect of electric current on the mechanical deformation of low melting alloys, assuming that is not due to Joule heating. Ren et al. [177] observed the ductile to brittle transition for the tensile fracture of eutectic 95.5Sn-3.8Ag-0.7Cu solder joints after passing an electric current of high electric current density for more than 96 hr at 145 °C. Yang and Zhao[122] and Zhao et al. [125] found that the contact modulus of pure tin and copper decrease with increasing electric current density, using nanoindentation technique. Liu et al. [178] studied the effect of current stressing on the stress relaxation behavior of Sn-solder joints and noted that the stress relaxation rate increased significantly after current stressing. Chen and Yang [11, 12, 179] studied the effect of electric current on the impression creep of Sn, SnPb alloy and Pb and found that the steady state impression velocity increased with the increase of electric current density. They suggested that the momentum exchange between moving electrons and lattice atoms reduced the energy barrier and increased the migration velocity of atoms. Kinney et al. [9] examined the effect of electric current on the double shear creep of Sn-Ag-Cu alloy and found that the creep rate increased with the current density. However, they suggested that the increase of the creep rate was caused by the temperature increase and the electric current may reduce the steady state creep rate. Kumar and Dutta [180] studied the effect of electric current on the single lap-shear creep of Si-Pb-Si sandwich structures

and observed that the sliding rate of interfaces is dependent on the relative direction of electron flow to the applied shear stress on the metal side of the interface. Shao et al. [126] analyzed the current effect on the diffusional creep in polycrystalline materials and found the field-assisted diffusional creep.

Passing an electric current through an electronic interconnect can cause an increase in local temperature due to Joule heating and an increase in mass transport due to the momentum exchange between electrons and atoms. To characterize the effect of electrical current on the time-dependent plastic deformation of electronic interconnect, this work is focused on studying the creep behavior of polycrystalline tin under the simultaneous action of an electrical current. The creep testis performed in the temperature range of 323-423 K and under the stress range from 1.93 to 13.89 MPa. A direct electric current with current density in the range of 0 to 3.78 kA/cm^{2}is passed through the tin specimen during the creep test. The evolution of surface temperature is monitored by a thermal couple as a function of time and electrical current. The stress dependence of the steady state creep rates is analyzed, using the power law relationship. The dependence of the stress exponent and apparent activation energy on electric current density is also discussed. The key differences of this work versus the literature are (a) the tensile creep is performed under the simultaneous action of an electrical current of high current density, (b) the dependence of the creep rate on the electric current density is evaluated, and (c) the surface evolution of tin specimens is examined after being subjected to electromechanical loading.

7.2 Experimental

The polycrystalline tin plate (99.99%) used in this work was purchased from McMaster-Carr (Chicago, IL). The tin plate was cut and rolled into thin sheets with a thickness of 0.317±0.007 mm. These sheets were then cut into small strips of 1.00±0.03 mm in width and ~50.00 mm in length. The gauge length for the creep test was ~15 mm in length. The thin strips were then heat-treated in air at 403 K for one hour and furnace-cooled to room temperature to release the residual stresses created by cutting and rolling and to obtain a homogeneous microstructure. The final cross-section area of the

specimens was~0.317 mm^2. All the specimens were cleaned with acetone using an ultrasonic cleaning machine before the creep test.

The RSA III (Rheometric Solids Analyzer; Rheometric Scientific Inc., Piscataway, NJ, USA) was used to perform the tensile creep test. An electric circuit was constructed to allow an electrical current to pass through the tin specimen. The specimen and electric circuit were insulated from the holding fixture, using insulation layers. The constant-load creep test was performed in a closed chamber with the chamber-temperature ranging 323 to 423 K and under the tensile stress range of 1.93 to 13.89 MPa. After the chamber reached the pre-set temperature, a small tensile pre-load was applied to the specimen. Simultaneously, an electrical current with the current density ranging from 0 to 3.78 kA/cm^2 was passed through the specimen. A thermal couple was used to monitor the evolution of surface temperature at the center of the specimen. Once the system reached thermal equilibrium, the desired load was applied to the specimen and the specimen length was recorded as a function of time. The steady state creep rate was then calculated from the slope of the creep curves, in which the creep rate is a linear function of time. The effects of stress, temperature, and electric current density on the steady state creep were analyzed.

7.3 Results and discussion

7.3.1 Electrothermalbehavior

Electrothermal tests were first conducted with the passage of an electric current of constant current intensity and without the action of mechanical loading. The surface temperature at the center of the Sn specimens was measured for different chamber temperatures. Figure 7.1 shows the evolution of the surface temperature at the center of the Sn specimens at a chamber temperature of 373 K for several electric current densities. The surface temperature increased with time due to Joule heating and reached a thermal equilibrium state after a short transient stage. The time required to reach local thermal equilibrium state was about 300 s. After reaching the local thermal equilibrium state, the surface temperature remained a constant and was higher than the chamber temperature. The passage of the larger current density led to the release of a large amount of Joule heat,

which resulted in the observed increase in local temperature for the same chamber temperature. It was important to know the true temperature of the specimen, which has an effect on the creep deformation.

Define T_e and T_0 as the equilibrium surface temperatures measured at the center of the specimen with and without the passage of an electric current, respectively. Figure 7.2 shows the dependence of T_e on the electric current density for several chamber temperatures. The equilibrium surface temperature increased with the increase in the electric current density for the same chamber temperature, which has a simple linear relationship with the square of the electric current density. The maximum temperature rise is 65.6 K for the current density of 3.78 kA/cm^2, which is 10.1% of the chamber temperature of 324.8 K. Using the best-curve fitting to fit the experimental results, one obtains

$$T_e = T_0 + 5.23J^2 \tag{7.1}$$

It is known that the Joule heat released due to the passage of an electric current is proportional to the square of the electric current density [181]. Thus, the result given in Eq. (7.1) confirms the temperature increase in the Sn specimens was controlled by the Joule heating.

7.3.2 Tensile creep

Once thermal equilibrium state was reached, the desired load was applied to the specimen and the specimen length was recorded as a function of time, from which the creep strain was calculated. Figure 7.3 shows the creep strain as a function of time for different tensile stresses at a chamber temperature of 373 K with the passage of an electric current of 1.89 kA/cm^2; the measured central temperature of the specimen was 393 K. The creep curves show typical tensile creep features. After a short transient stage due to elastoplastic deformation, the tensile creep reaches a steady state. During the steady-state stage, the tensile strain is a linear function of time, from which the steady state creep rate is calculated. After the steady state, an accelerating creep state (tertiary

creep) occurs due to the accumulating damage, which leads to the creep rupture of the Sn specimens. The steady state creep rate increases with increasing tensile stress under the action of the same electric current density (electric current) at the same chamber temperature.

Figure 7.4 shows the creep strain as a function of time at a chamber temperature of 348 K for several electric currents when subjected to a tensile stress of 4.63 MPa. The creep curves with the passage of an electric current through the tensile specimen are similar to those without the passage of an electrical current, which suggest that there always exists a steady state creep deformation in polycrystalline tin under the experimental conditions. The creep rate increases with increasing the current density for the specimens of the same geometrical configuration. Note that the passage of an electric current through the Sn strips caused the temperature increase. As shown in Fig. 7.2, the surface temperature at the center of the Sn specimens with the passage of an electric current of 2.52 kA/cm^2 is 376 K. Subjected to the same tensile stress of 3.09 MPa, the steady state creep rate for the tensile creep of the Sn-strips with the action of an electric current of 2.52 kA/cm^{2}at the chamber temperature of 348 K is found to be 5.41×10^{-6} 1/s about 3 times of 1.83×10^{-6} 1/s for the tensile creep of the Sn-strips without the action of an electric current at the chamber temperature of 376 K. This result implies that the effect of electric current on the creep deformation of the Sn-strips cannot be attributed only to Joule heating. The simultaneous action of electric current and mechanical stress introduced electrical-thermal-mechanical interaction and the Sn specimens experienced time-dependent electrical-thermal-mechanical deformation.

Figure 7.5 shows typical SEM micrographs of the polycrystalline Sn specimens under three different electromechanical conditions for ~4.7 hr. Figure 7.5a shows the initial surface morphology of the Sn strips directly before any heat treatment and electrical-mechanical loading. No surface irregularity and grain boundary boundaries were observable. Figure 7.5b shows the change of the surface morphology of a Sn strip under the action of only thermal treatment at 348 K, some grain boundary grooving and grain rotation were present. The average grain size was about 60 μm. When the heat treatment

temperature was increased to 376 K, which was the temperature for the sample with the passage of an electric current of 2.52 kA/cm^2 at the chamber temperature of 348 K, the grain boundary grooving became slightly more pronounced, as shown in Fig. 7.5c. With the tensile stress of 3.08 MPa applied to the Sn specimen at the chamber temperature of 348 K, the Sn specimen experienced creep deformation. Local grain rotation and grain boundary sliding occurred, as shown in Fig. 7.5d. But, there was no significant change in the microstructure when compared to Fig. 7.5c. Under the simultaneous action of mechanical loading and electric current, the surface of the Sn specimen became irregularity, as show in Fig. 7.5e and 7.5f with a titled angle of 80º. The electromechanical interaction created larger grain boundary sliding and grain rotation than that simply due to mechanical loading or electric loading. The severity of local surface distortion was dependent on the mechanical stress, electrical current density, Joule heating, and creep time. Thus, for the same mechanical stress and creep time, the passage of an electrical current caused more damage due to the larger deformation.

7.3.3 Dependence of creep rate on electric current and tensile stress

The passage of an electrical current through a conducting material introduces electrical-thermal-mechanical interaction, which causes 1) the temperature to increase in the material and 2) the atomic migration along the drifting direction of high speed electrons due to the momentum exchange between the electrons and atoms. Both the Joule heating and the momentum exchange are dependent on electric energy, which is proportional to the square of the electric current density.

In studying the effect of electric current on the impression creep of low melting alloys, Chen and Yang [11, 12, 179]observed that the steady state impression velocity is a linear function of the square of the electric current. From the relationship between the uniaxial creep rate and the impression velocity [81], one expects that the uniaxial creep rate is also a linear function of the square of the electric current density as

$$\dot{\varepsilon} = \dot{\varepsilon}_0 + \lambda J^2 \tag{7.2}$$

where $\dot{\varepsilon}$ is the steady state creep rate with an electrical current density of J passing through the Sn specimen, $\dot{\varepsilon}_0$ is the steady state creep rate without the passage of an electrical current, and λ is a constant dependent on the tensile stress and temperature.

Figure 7.6 shows the dependence of the steady state creep rate on the square of the electrical current density for several chamber temperatures when subjected to a tensile stress of 3.09 MPa. The steady state creep rate is a linear function of the square of the electrical current density in good accord with Eq. (7.2). It is known that electrical energy is proportional to the square of the electrical current. The result shown in Fig. 6 indicates that the tensile creep of tin under the action of electrical-mechanical loading is dependent on the electric energy dissipated in the sample.

Several relationships have been used to analyze the stress dependence of the creep deformation of Sn and Sn-alloys, which include the Garofalo relation [93, 182], hyperbolic sine relation [102, 183], and power-law relation [184, 185]. For the power-law relationship, the steady state creep rate as a function of the applied stress can be expressed as

$$\dot{\varepsilon} = A\sigma^n \exp(-\frac{Q}{RT}) \tag{7.3}$$

where $\dot{\varepsilon}$ is the steady state creep rate, σ is the applied stress, A is a constant, n is the stress exponent, Q is the activation energy for the rate process, R is the gas constant, and T is absolute temperature.

Figure 7.7 shows the dependence of the steady state creep rate on the tensile stress without the passage of an electrical current in the samples (J=0 kA/cm^2) in the log-log scale. The dependence of the creep rate on the tensile stress follows Eq. (7.3) for the experimental conditions with the stress exponent in the range of 5.32 to 6.18. Figure 7.8 shows the dependence of the steady state creep rate on the tensile stress in the log-log scale at a chamber temperature of 323 K for several electric current densities. The stress dependence of the creep rate also follows Eq. (7.3) as shown by the curve fitting in Fig. 8,

similar to the creep deformation without an electrical current passing through the specimens.

Table 7.1 lists the stress exponents calculated for the electric current densities used in the experiments. The stress exponent is in the range of 4.04 to 6.18 for all the temperatures and electric current densities, which suggests that there is no significant change in the stress exponent. The passage of an electric current does not change the stress exponent for the creep of pure tin under the experimental conditions.

Table 7.2 summarizes the stress exponents available in the literature for the creep of Sn including this work for the condition of J=0 kA/cm^2.For the impression creep, the stress given in Table 7.2 is equal to the punching stress divided by 3.3. Obviously, the result obtained in this work without the passage of an electric current is comparable to those from the conventional creep tests [88, 99, 186-190] and to that for the impression creep of Sn in the same stress range [94].

7.3.4 Activation strain volume and activation energy

For the creep deformation following the power law relation between the tensile stress and the creep rate, the activation strain volume, Ω, can be calculated as [191],

$$\Omega = RT\left(\frac{\partial \ln \dot{\varepsilon}}{\partial \sigma}\right)_T = \frac{nRT}{\sigma} \tag{7.4}$$

The stress dependence of the activation strain volume is shown in Fig. 7.9 for several electrical current densities. In the calculation of the activation strain volume, the surface temperatures measured at the center of the Sn-specimens are used. For the same electric current density, the activation strain volume decreases with increasing tensile stress in accord with the stress-assisted thermal activation process. The activation strain volume is independent of the electric current density for the same tensile stress, which implies that the electrical-thermal-mechanical interaction has no significant effect on the activation strain volume for the experimental conditions.

From Eq. (7.3), one can examine the temperature dependence of the steady state creep rate. Figure 7.10 shows the temperature dependence of the steady state creep rate without the passage of an electric current. The activation energy calculated is in the range of 60.26 to 69.17 kJ/mol. There is no stress-dependence of the activation energy.

Figure 7.11 shows the dependence of the steady state creep rate on temperature for several electric current densities when subjected to a tensile stress of 3.09 MPa. Note the surface temperatures measured at the center of the Sn-specimens are used in the calculation of the activation energy. The apparent activation energy is in the range of 55.70 to 64.76 kJ/mol. Similar to the impression creep of Sn [12], the electrical-thermal-mechanical interaction due to the passage of an electric current does not change the rate mechanisms controlling the creep deformation of the Sn-specimens for the experimental conditions. Such a result is consistent with the evolution of microstructures as shown in Fig. 7.5, i.e. the tensile creep of the Sn is controlled by the grain boundary sliding and grain rotation. There was relatively uniform distribution of temperature and electric current in the tensile test, and the momentum exchange between high-speed electrons and lattice atoms only caused the increase of the creep rate by accelerating mass transport.

Table 7.3 lists the apparent activation energies calculated for the electric current densities used in the experimental conditions. The activation energy is in the range of 55.70 to 74.03 kJ/mol. This result implies that there is no significant change in the activation energy.

Table 7.2 also summaries the activation energies available in the literature for the creep of pure Sn, including this work for the condition of J=0 kA/cm^2. Obviously, the result obtained in this work without the passage of electric current is comparable to those from the conventional creep tests [88, 186, 188-190, 192] and to that for the impression creep of Sn in the same stress range [94].

In general, the creep of crystalline metals at temperatures near melting point is controlled by dislocation motion with the activation energy approximately the same as that for lattice diffusion. However, the testing temperatures in this work are in the range

of 0.64 T_m to 0.84 T_m. The activation energy for the rate process is near one-half of the values for self-diffusion in Sn (133 kJ/mol parallel to tetragonal axis and 80.8 kJ/mol perpendicular to tetragonal axis [193]), and hence it is reasonable to interpret them as the activation energy for grain boundary diffusion [194]. This result suggests that the rate process for the tensile creep of the Sn for the experimental conditions is grain boundary activity consisting of diffusion and sliding.

According to Chen and Yang [134], the empirical relation between the apparent activation energy and the electric current can be expressed as

$$Q_{\mathrm{app}} = Q_0 - \beta J^2 \tag{7.5}$$

where Q_0 is the activation energy for the rate process at J=0 A, and β is a constant. Substituting Eqs. (7.1) and(7.5) into Eq. (7.3) gives

$$\dot{\varepsilon} = A\sigma^n \exp\left[-\frac{Q_0 - \beta J^2}{R(T + 5.23J^2)}\right] \tag{7.6}$$

To the order of J^2, Eq. (7.6) can be approximated as

$$\dot{\varepsilon} = A\sigma^n \left(1 + \frac{\beta + 5.23Q_0}{RT} J^2\right)\exp\left(-\frac{Q_0}{RT}\right) = A\sigma^n \left(1 + \alpha J^2\right)\exp\left(-\frac{Q_0}{RT}\right) \tag{7.7}$$

with $\alpha = (\beta + 5.23Q_0)/RT$. Equation (7.7) takes the effect of electromechanical interaction into consideration in describing the power-law creep of metallic alloys, which is in accord with the experimental result of Eq. (7.2) even with β=0.

7.4 Summary

The tensile creep of polycrystalline tin was studied in the chamber temperature range of 323-423 K and under the tensile stress of1.93-13.89 MPa when there was a direct electrical current simultaneously passing through the Sn specimen. The electric current density was in the range of 0-3.78kA/cm^2.The passage of an electrical current introduced

electrical-thermal-mechanical interaction and had a significant effect on the creep deformation of tin, which are summarized below.

1) The rise of the surface temperature at the center of the Sn specimens is proportional to the square of the electric current density due to the Joule heating.

2) The steady state creep rate increased linearly with the square of the electric current density, which was due to the combined effects of Joule heating and the momentum exchange between lattice atoms and high-speed electrons driven by large electric field intensity.

3) The stress dependence of the steady state creep rate followed the power-law relation. The activation strain volume decreased with the increase in the tensile stress in accord with the stress-assisted thermal activation process.

4) The apparent activation energy for the rate process was in the range of 55.70 to 64.76 kJ/mol and the stress exponent is in the range of 4.04 to 6.18.The electrical current has no significant effect on the apparent activation energy and stress exponent. The passage of an electrical current into the Sn specimens did not change the rate mechanism, which controls the creep deformation of tin under the experimental conditions.

Table 7.1 Stress exponents for the creep deformation of Sn under the action of electric current

J (kA/cm^2)	Chamber temperature (K)				
	323	348	373	398	423
0	6.18	6.15	5.46	5.39	5.32
1.26	6.15	5.29	5.51	5.54	4.98
1.89	6.05	5.31	5.12	4.97	
2.52	5.80	5.64	5.74	4.04	
2.83	5.65	6.04	5.85		
3.15	5.63	4.43			
3.78	5.81	6.07			

Table 7.2 List of the stress exponents and activation energies for the creep of Sn

Creep test	Materials	σ (MPa)	T (K)	n	Q (kJ/mol)	Ref
Tensile creep	Single crystal [100]	1 or 1.57	343-423		40-52	[192]
Tensile creep	Single crystal [100]	1 or 1.57	423-473		98-118	[195]
Tensile creep	Poly-crystal	1.8-18	293-463	6	35	[186]
Tensile creep	Poly-crystal	4.34-9.61	294.1-363	4.6	46	[186]
Tensile creep	Poly-crystal	4.34-9.61	363-433		109	[186]
Tensile creep	Poly-crystal	0.6-6	304-403	3.6-4.1	46.1	[190]
Tensile creep	Poly-crystal	0.6-6	403-492	3.6-4.1	92.1	[190]
Compression creep	Single crystal		298-394		50.2	[189]
Compression creep	Single crystal		394-493		102.6	[189]
Tensile creep	Poly-crystal	2.76-6.89	298-478		87.9	[187]
Tensile creep	Single crystal [100]	1.57	343-423		48	[188]
Tensile creep	Single crystal [100]	1.57	423-473		118	[188]
Tensile creep	Poly-crystal	1-30	296-473	7.6	60.3	[88]
Impression creep	Single crystal	2.28-14.45	313-423	3.6-5.0	12-20	[99]
Impression creep	Single crystal	2.28-14.45	423-481	3.6-5.0	104.7-108.9	[99]
Impression creep	Poly-crystal	3.03-15.15	323-423	5	43	[94]
Compression creep	Poly-crystal	3-20	323-423	5	41	[94]
Impression creep	Poly-crystal	3.64-16.67	343 – 398		27.2	[12]
Indentation creep	Single crystal	Load 0.2-0.49 N	303-403	4.5-6.5	49	[196, 197]
Indentation creep	Single crystal	Load 0.2-0.49 N	418-483	4.5-6.5	110	[196, 197]
Shear creep	Bicrystal	0.049-0.206	453-498		80.4	[198]
Shear creep	Poly-crystal	0.034-0.69	402-495	1-6.6	93.6	[199]
Tensile creep	Poly-crystal	1.93-13.89	323-423	4.04-6.18	55.70-74.03	This work

Table 7.3 Apparent activation energies for the creep deformation of Sn under the action of electric current

	Tensile Stress (MPa)					
J (kA/cm^2)	1.54	3.09	4.63	6.17	7.72	9.26
0		60.26	69.17	67.29	62.54	65.94
1.26	63.42	64.76	74.03	67.64	68.39	
1.89	67.99	55.70	58.39	57.74		
2.52	69.71	57.43	63.42			

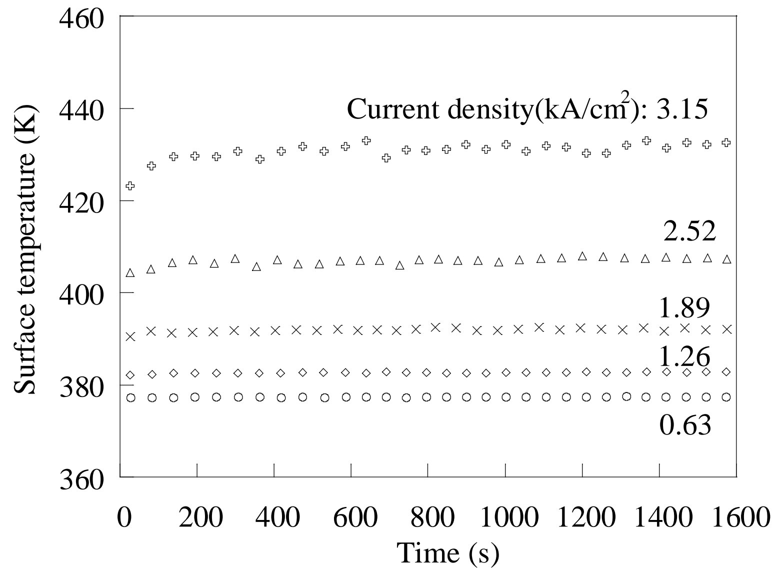

Figure 7.1Temporal evolution of the surface temperature at the center of the Sn specimens at a chamber temperature of 373 K for different electric current densities

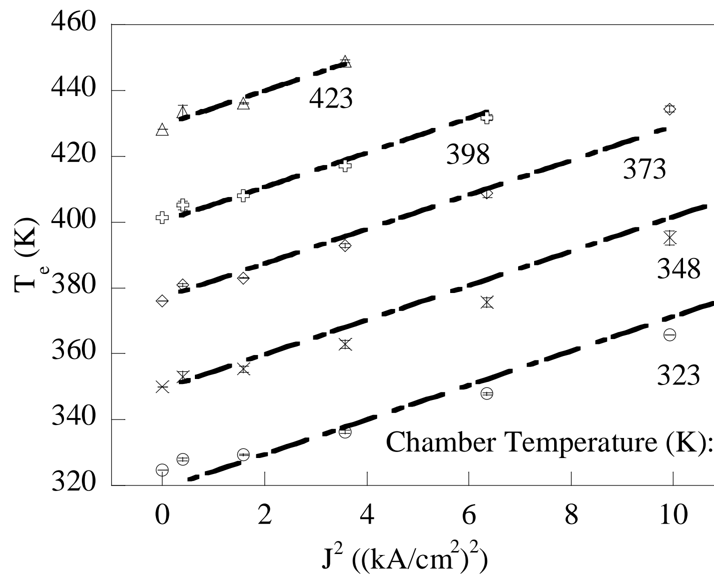

Figure 7.2 Dependence of the equilibrium surface temperature, T_e,on electric current density for several chamber temperatures

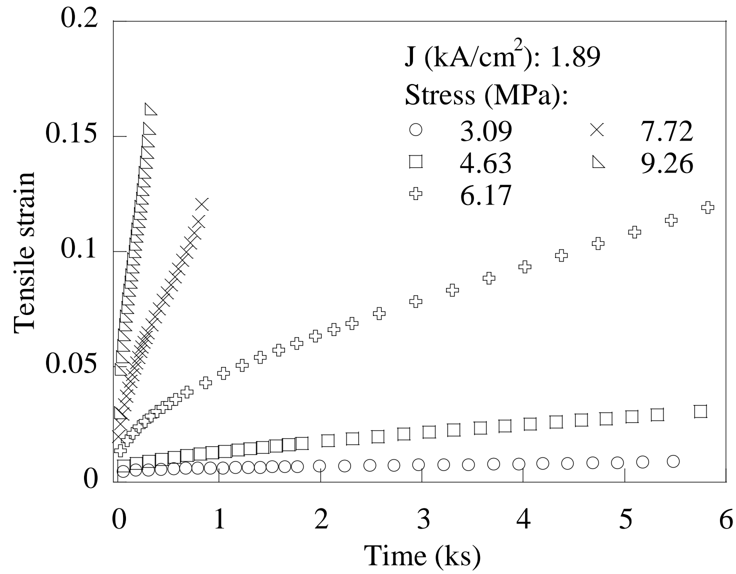

Figure 7.3 Time dependence of the tensile strain for several tensile stresses at a chamber temperature of 323 K and an electric current of 1.89 kA/cm^2

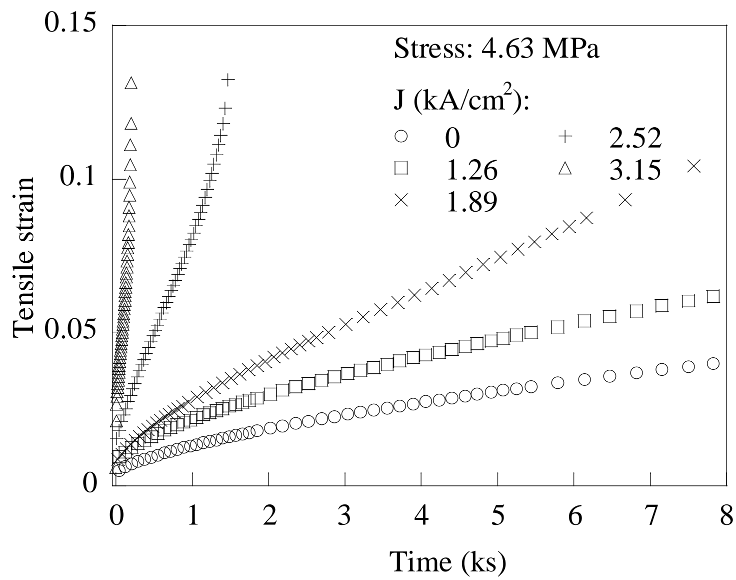

Figure 7.4 Time dependence of the tensile strain for several electrical current densities at a chamber temperature of 348 K and a tensile stress of 4.63 MPa

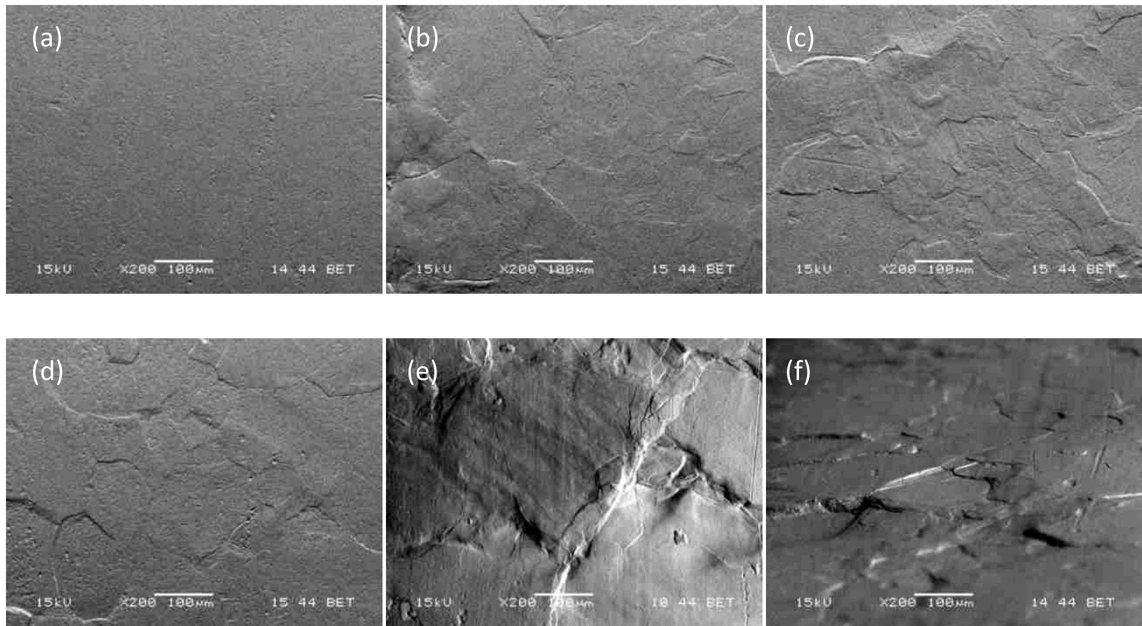

Figure 7.5 Effect of electromechanical interaction on the SEM micrographs of the polycrystalline tin specimens for ~4.7 hr; (a) J=0 A/cm^2, σ=0 MPa, and T=273 K, (b) J=0 A/cm^2, σ=0 MPa, and T=348 K,(c) J=0 A/cm^2, σ=0 MPa, and T=376 K, (d) J=0 A/cm^2, σ=3.08MPa, and T=348 K, and (e) J=2.52 kA/cm^2, σ=3.08MPa, and T=348 K,and (f) J=2.52 kA/cm^2, σ=3.08MPa, and T=348 K(titled angle: 80º)

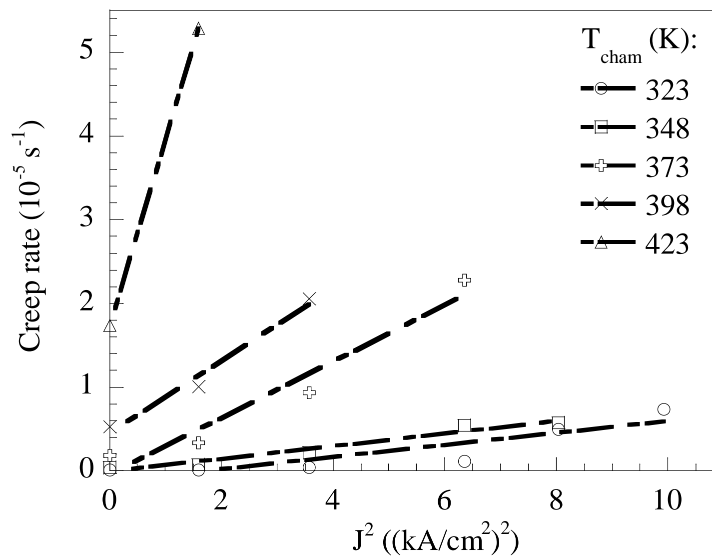

Figure 7.6 Dependence of the steady state creep rate on the electric current density for several chamber temperatures (T_{cham}) under the action of a tensile stress of 3.09 MPa

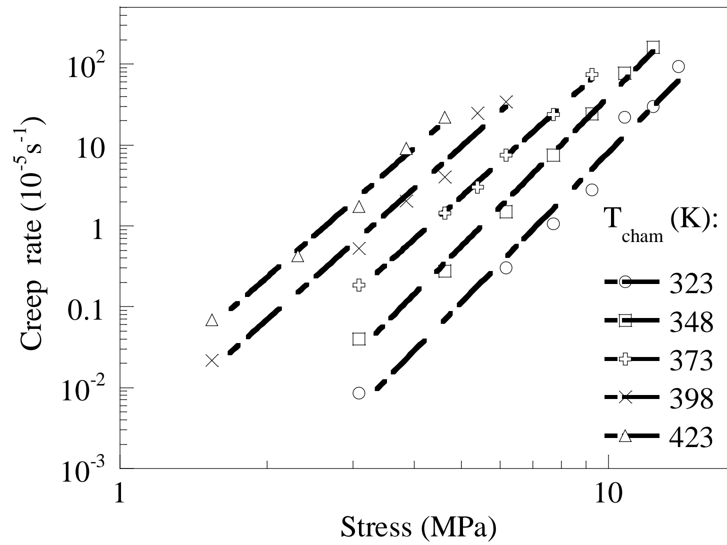

Figure 7.7 Dependence of the steady state creep rate on the tensile stress with *J*= 0 kA/cm^2 for several chamber temperatures

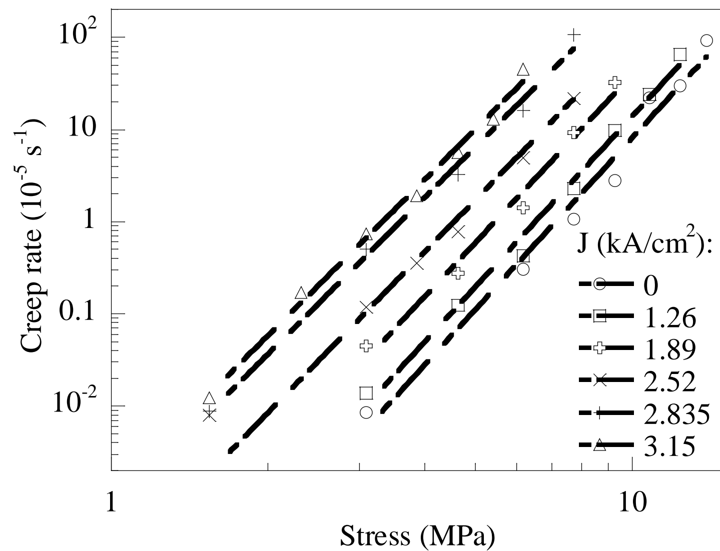

Figure 7.8 Dependence of the steady state creep rate on the tensile stress at a chamber temperature of 323 K for several electric current densities

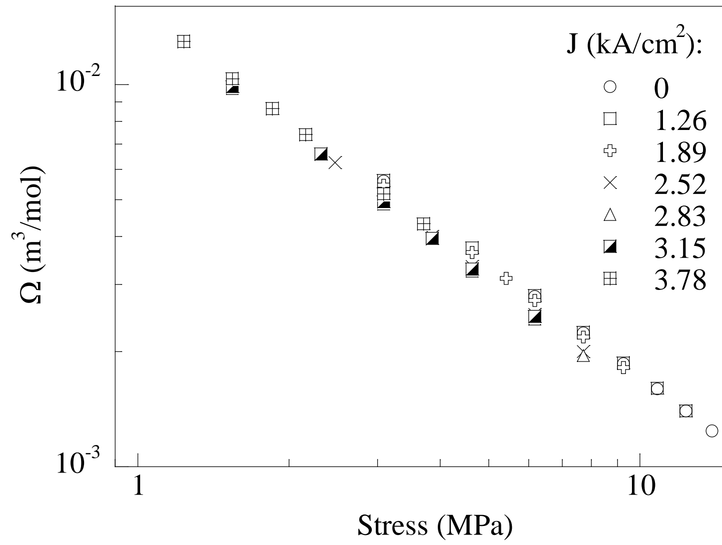

Figure 7.9 Stress dependence of the activation shear strain volume for different electric currents at a chamber temperature of 323 K

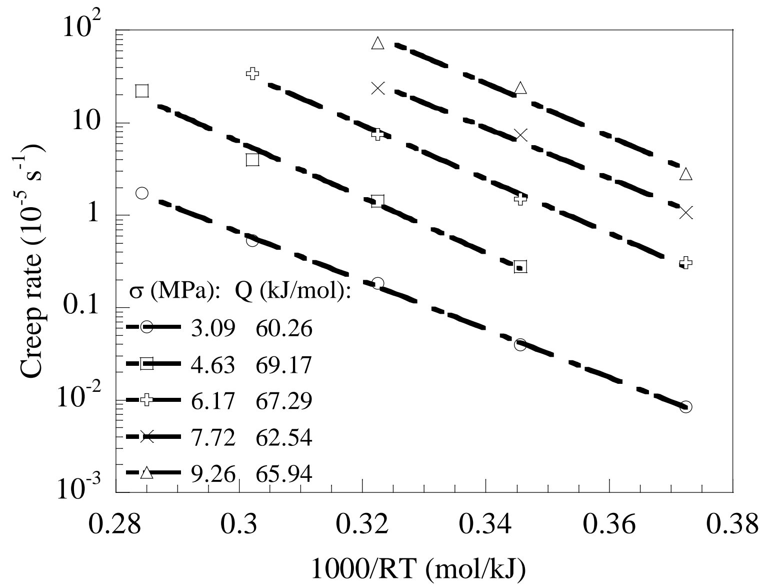

Figure 7.10 Temperature dependence of the steady state creep for several tensile stresses with $J = 0$ kA/cm^2

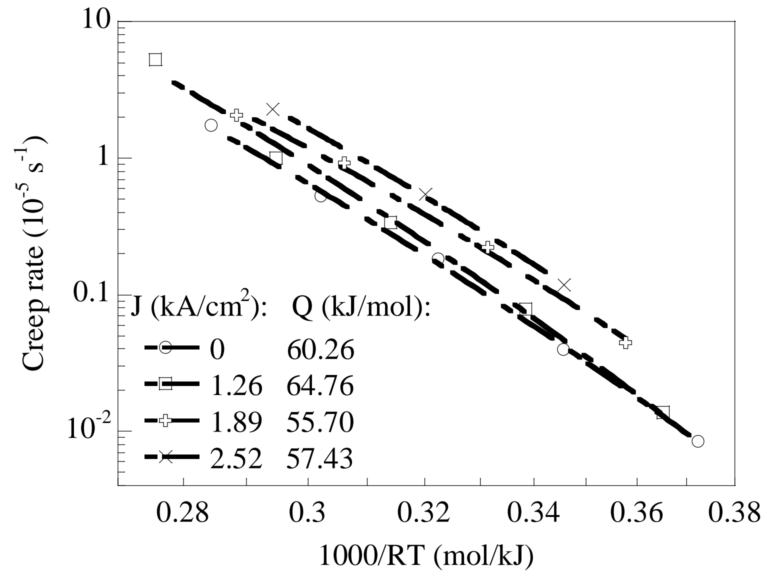

Figure 7.11 Temperature dependence of the steady state creep for several electric current densities under a tensile stress of 3.09 MPa

Chapter 8 Summary

8.1 Conclusion

With the decreasing size and increasing electric current density in today's electronics industry, the passage of electric current of high current density has placed a great challenge on controlling the reliability of electronics under service conditions. In this dissertation, the electrical-thermal-mechanical behavior of copper and tin was studied under the action of an electric current. The electromechanical response of copper, the nanoindentation of copper, the nanoindentation of tin, and the tensile creep of tin current were conducted when subjected to various current conditions.

The electromechanical response of Cu strips was investigated by passing an DC electric current through the strips with the electric current density in the range of 12.34 to 29.60 kA/cm^2. The evolution of electric resistance was monitored over time. It was found that the change of the electric resistance can be divided into three stages: transient stage, quasi-steady stage, and fusing stage. During the quasi-steady stage, the electric resistance of the Cu strips linearly increased with time before the electric fusing occurred. The time-to-fusing can be described by a power law relation. For the region of relatively low current densities the current exponent ranged from 17.9 to 44.6, and for the region of high current densities the current exponent ranged from 2.5 to 5.2. The current exponent for relatively low current densities decreased as the length of the Cu strips increased, showing size-dependence. Also, the electromechanical deformation of the Cu strips was investigated from micro and macro aspects. From the micro aspect, grain growth and grain rotation occurred in both the melted region and the heat-affected region when passing an electric current of high current density, which might be due to the electrical-thermal-mechanical interaction. From the macro aspect, electric buckling of the Cu strips was observed for various electric current densities. The maximum deflection of the strips increased with increasing electric current density, and the total strain was proportional to the square of electric current density.

Using the nanoindentation technique, the electrical-thermal-mechanical behavior of Cu and Sn strips was studied with the passage of DC and AC electric current. During the

electrothermal test with constant electric current density, the surface temperature initially increased with time and reached a constant value following a transient state. The equilibrium surface temperature increased as the electric current density increased. The loading-unloading curves from electric nanoindentation were used to calculate both the hardness and the reduced contact modulus of Cu and Sn. The reduced contact modulus decreased as the electric current density increased for the experimental conditions.

The effect of DC electric current on the indentation deformation of Cu strips was studied under the indentation load of 50 μN to 1000 μN for the current densities ranging from 6.4 to 31.8 kA/cm^2. The experimental results suggested that the reduced contact modulus decreased with increasing electric current density, which might be due to electrical-thermal-mechanical interaction introduced by the high density electric current. The decrease of the contact modulus was likely due to the electrothermal interaction caused by Joule heating and the momentum exchange between high-speed electrons and atoms, which changed the equilibrium distance between atoms. The reduced contact modulus is a function the electric current density, in accord with the experimental observation. However, the indentation hardness was found to increase with the increasing electric current density, which was possibly due to the current-induced multiplication and motion of dislocations.

The effect of AC electric current on the indentation behavior of Cu-strips was studied under the indentation load of 100 μN to 1600 μN for the current densities ranging from 1.25 to 4.88 kA/cm^2. The reduced contact modulus decreased as the electric current density increased. The dependence of the reduced contact modulus on the electric current density can be expressed with a linear relationship. The results suggested that the electromechanical interaction due to the momentum exchange between high-speed electrons and atoms played an important role in controlling the elastic indentation of Cu strips when there was an electric current passing through the strips. The indentation hardness decreased as the indentation load increased, demonstrating a normal indentation size effect. Using the theory of strain gradient plasticity, the strain gradient underneath the indentation was found to slightly decrease as the electric current density increased.

The effect of DC electric current on the indentation deformation of Sn strips was characterized under the indentation load of 50 μN to 200 μN for the current densities ranging from 0.99 to 4.09 kA/cm^2. The reduced contact modulus decreased as the electric current density increased. The decrease of the reduced contact modulus was controlled by the temperature rise due to Joule heating and the momentum exchange between the high speed electrons and the lattice atoms. However, the dominant effect of the DC electric current on the indentation deformation of Sn strips was controlled by the electrothermal interaction due to Joule heating in the experimental condition. A simple relation was proposed to describe the dependence of the reduced contact modulus on the electric current density. For the indentation load less than 150 μN, the indentation hardness first increased and then decreased as the electric current density increased. For the indentation load larger than or equal to 175 μN, the indentation hardness was independent of the electric current density. Meanwhile, the indentation hardness was found to decrease with increasing indentation load, showing normal indentation size effect. Using the theory of strain gradient plasticity, the relationship between the indentation hardness and the indentation depth was analyzed. The results suggested that both the indentation hardness in the limit of infinite depth and the characteristic length were dependent on the electric current density. From the calculation, the shear modulus of the Sn-strips was found to decrease as the electric current density increased, in accordance with the decrease of the reduced contact modulus as measured from the slope of the unloading curves.

The tensile creep deformation of Sn with passage of a DC electric current in the range from 0 to 3.78 kA/cm^2 was investigated in a temperature range of 323-423 K under the tensile stress of 1.93 to 13.89 MPa. The passage of a DC electric current introduced electrical-thermal-mechanical interaction and had a significant effect on the creep deformation of Sn. Due to the Joule heating, the equilibrium central surface temperature of the Sn strips increased as the electric current density increased, which had a linear relationship with the square of the electric current density. The steady state creep deformation was analyzed under the simultaneous action of the electric current and tensile stress. The steady state creep rate increased as the electric current density increased which was likely due to Joule heating and momentum exchange between the

high speed electrons and the lattice atoms. The steady state creep rate had a linear relationship with the square of the electric current density. The activation strain volume decreased with the increase in the tensile stress in accord with the stress-assisted thermal activation process. The stress exponent was in the range of 4.04 to 6.18, and the apparent activation energy was in the range of 55.70 to 64.76 kJ/mol, both showing no dependence on the electric current density. The experimental results suggest that the passage of a DC electric current did not change the mechanism of the tensile creep deformation of Sn strips under the experimental conditions.

8.2 Future work

In this work, Cu and Sn were used to study their electro-thermal-mechanical behavior under the action of an electric current. However, there are various metallic materials which have been widely used for electronic devices and systems, such as aluminum, tin-lead alloy, tin based lead-free alloy, and so on. They have different physical and mechanical properties, compared to Cu and Sn. Further research needs to consider the effect of microstructure and mechanical properties.

Under the action of an electric current, there exist Joule heating, the momentum exchange between the high speed electrons and lattice atoms, and magnetic field in the materials. Electric currents in various forms will have different effects on their electromechanical behavior. These effects need to be investigated carefully. In this dissertation, simple direct and alternating electric current with various electric current densities have been applied to Cu and Sn to study the corresponding electro-thermal-mechanical behavior. However, the effect of AC current require further investigation.

8.2.1 Characterization of Joule heat and temperature distribution in metallic materials

Joule heat was found to be proportional to the square of electric current density for metallic materials under the action of an electric current. The thermal conduction and temperature distribution have a great effect on the deformation behavior of metallic materials. The understanding of Joule heating is important to evaluate the mechanical properties of metallic materials with the passage of an electric current. Various contacting

conditions will be designed to investigate the thermal conduction across the materials and the interface. Also, the effect of the size and shape of these materials will be analyzed.

8.2.2 Microstructure evolution

Surface morphology change was observed for Cu and Sn after current stressing with simple DC and AC electric current. It was suggested that the microstructure evolution in metallic materials with the passage of electric current was due to the Joule heat and momentum exchange between the high speed electrons and atoms. The study of the microstructure evolution has been limited to qualitative analysis, and the quantitative analysis might not be easily conducted. It is desirable to explore the effect of electric current on the microstructure evolution of metallic materials. In addition, the real-time microstructure change caused by electric currents can be investigated by in-situ XRD and TEM.

8.2.3 Electromechanical response of metallic materials

The electromechanical response of Cu strips was studied in this dissertation. Not only microstructure evolution, but also the buckling of Cu strips was introduced by the passage of a DC electric current. Under the action of an electric current of high current density, the electronic interconnects could experience mechanical deformation due to the Joule heating and momentum exchange between the high speed electrons and lattice atoms. The deformation could be significant for electronics of micro and sub-micro sizes and cause structural damage. The electromechanical response of metallic materials needs to be studied under the action of electric current conditions, including long-time and short-time effects. For the long time effect, the deformation behavior of metallic materials after current stressing will be worthy of investigation. Both DC and AC electric current will be used to study the structural evolution and the change of mechanical behavior after long-time current stressing. For the short time effect, the real-time electromechanical response will be investigated.

8.2.4 Indentation deformation of metallic materials

In this dissertation, the indentation deformation of Cu and Sn with DC and AC electric currents was reported. It was found that the reduced contact modulus was reduced. However, the mechanism of the indentation deformation behavior has not been fully understood. The effect of the electric current on the indentation hardness was found to depend on the materials and indentation parameters. Various metallic materials with different microstructures should be used to study the effect of electric current on the indentation deformation behavior. The effect of electric current on the indentation deformation behavior of metallic materials will be studied for both short and long term aspects. For the short term effect, the test will be conducted after the sample reaches thermal equilibrium state. The temperature effect due to Joule heating can be reduced by controlling testing environment. Also, the effect of temperature on the indentation deformation of these materials can be conducted to make compare. For the long term effect, the mechanisms controlling the mechanical behavior after electromigration will be examined.

8.2.5 Creep behavior of metallic materials

The effect of an electric current on the creep deformation of pure Sn was studied by tensile creep. Only DC electric current with different densities was used. And the testing temperature and stress range were limited. Wide testing conditions need to be used to understand the creep mechanism of metallic materials with the passage of an electric current. The electro-thermal test will be helpful to analyze the temperature-related parameters of the creep behavior. Full understanding of the creep deformation of metallic materials under the action of electric current requires the investigation of the effects of electric current densities and testing conditions. In addition, many other creep testing techniques, such as compression, impression, and shear creep, should also be used to understand the creep deformation of metallic materials under the action of an electric current.

Reference

1. Le Meur, G., B. Bourouga, and J.P. Bardon, Microscopic analysis of interfacial electrothermal phenomena - definition of a heat generation factor. International Journal of Heat and Mass Transfer, 2006. **49**(1-2): p. 387-401.

2. Di Giacomo, G., Reliability of electronic packages and semiconductor devices. Electronic packaging and interconnection series1997, New York: McGraw-Hill. xiv, 410 p.

3. Dwyer, V.M., An investigation of electromigration induced void nucleation time statistics in short copper interconnects. Journal of Applied Physics, 2010. **107**(10).

4. Tao, C., W.G. Cullen, and E.D. Williams, Visualizing the Electron Scattering Force in Nanostructures. Science, 2010. **328**(5979): p. 736-740.

5. Varshni, Y.P., Temperature dependence of the elastic constants. Physical Review B-Solid State, 1970. **2**(10): p. 3952-3958.

6. Merchant, H.D., et al., Hardness-Temperature Relationships in Metals. Journal of Materials Science, 1973. **8**(3): p. 437-442.

7. Newey, D., M.A. Wilkins, and H.M. Pollock, An Ultra-Low-Load Penetration Hardness Tester. Journal of Physics E-Scientific Instruments, 1982. **15**(1): p. 119-122.

8. Lu, Y.C., et al., High Temperature Nanoindentation of PMR-15 Polyimide. Experimental Mechanics, 2010. **50**(4): p. 491-499.

9. Kinney, C., et al., The Influence of an Imposed Current on the Creep of Sn-Ag-Cu Solder. Journal of Electronic Materials, 2009. **38**(2): p. 221-226.

10. Kinney, C., et al., The Interaction Between an Imposed Current and the Creep of Idealized Sn-Ag-Cu Solder Interconnects. Journal of Electronic Materials, 2009. **38**(12): p. 2585-2591.

11. Chen, R. and F.Q. Yang, Effect of electric current on the creep deformation of lead. Materials Science and Engineering a-Structural Materials Properties Microstructure and Processing, 2011. **528**(6): p. 2319-2325.

12. Chen, R. and F.Q. Yang, Effect of DC Current on the Creep Deformation of Tin. Journal of Electronic Materials, 2010. **39**(12): p. 2611-2617.

13. Chen, R. and F.Q. Yang, Impression creep of a Sn60Pb40 alloy: the effect of electric current. Journal of Physics D-Applied Physics, 2008. **41**(15): p. -.

14. Michael, N.L., et al., Mechanism of electromigration failure in submicron Cu interconnects. Journal of Electronic Materials, 2002. **31**(10): p. 1004-1008.

15. Shao, W., et al., Electromigration in copper damascene interconnects: reservoir effects and failure analysis. Surface & Coatings Technology, 2005. **198**(1-3): p. 257-261.

16. Yang, F.Q. and J.C.M. Li, Deformation behavior of tin and some tin alloys. Journal of Materials Science-Materials in Electronics, 2007. **18**(1-3): p. 191-210.

17. Tu, K.N. and K. Zeng, Tin-lead (SnPb) solder reaction in flip chip technology. Materials Science & Engineering R-Reports, 2001. **34**(1): p. 1-58.

18. Bath, J., Lead-free soldering2007, New York: Springer.

19. Abtew, M. and G. Selvaduray, Lead-free solders in microelectronics. Materials Science & Engineering R-Reports, 2000. **27**(5-6): p. 95-141.

20. Anderson, I.E., et al., Alloying effects in near-eutectic Sn-Ag-Cu solder alloys for improved microstructural stability. Journal of Electronic Materials, 2001. **30**(9): p. 1050-1059.

21. Chen, B. and C. Basaran, Measuring Joule heating and strain induced by electrical current with Moire interferometry. Journal of Applied Physics, 2011. **109**(7).

22. Tu, K.N., Recent advances on electromigration in very-large-scale-integration of interconnects. Journal of Applied Physics, 2003. **94**(9): p. 5451-5473.

23. Herring, C., Diffusional Viscosity of a Polycrystalline Solid. Journal of Applied Physics, 1950. **21**(5): p. 437-445.

24. Huntington, H.B. and A.R. Grone, Current-Induced Marker Motion in Gold Wires. Journal of Physics and Chemistry of Solids, 1961. **20**(1-2): p. 76-87.

25. Chen, C., H.M. Tong, and K.N. Tu, Electromigration and Thermomigration in Pb-Free Flip-Chip Solder Joints, in Annual Review of Materials Research, Vol 40, D.R. Clarke, M. Ruhle, and F. Zok, Editors. 2010, Annual Reviews: Palo Alto. p. 531-555.

26. Black, J.R., Electromigration - a Brief Survey and Some Recent Results. Ieee Transactions on Electron Devices, 1969. **Ed16**(4): p. 338-&.

27. Conrad, H., et al., Effect of Electric-Current Pulses on the Recrystallization Kinetics of Copper. Scripta Metallurgica, 1988. **22**(2): p. 235-238.

28. Conrad, H., N. Karam, and S. Mannan, Effect of Electric-Current Pulses on the Recrystallization of Copper. Scripta Metallurgica, 1983. **17**(3): p. 411-416.

29. Kuo, S.M. and K.L. Lin, Recrystallization under electromigration of a solder alloy. Journal of Applied Physics, 2009. **106**(2).

30. Chen, H.T., et al., Localized recrystallization and cracking of lead-free solder interconnections under thermal cycling. Journal of Materials Research, 2011. **26**(16): p. 2103-2116.

31. Wu, A.T., et al., Electromigration-induced microstructure evolution in tin studied by synchrotron x-ray microdiffraction. Applied Physics Letters, 2004. **85**(13): p. 2490-2492.

32. Wu, A.T., et al., Electromigration-induced grain rotation in anisotropic conducting beta tin. Applied Physics Letters, 2005. **86**(24).

33. Liu, S.H., et al., Tin whisker growth driven by electrical currents. Journal of Applied Physics, 2004. **95**(12): p. 7742-7747.

34. Glazer, J., Metallurgy of Low-Temperature Pb-Free Solders for Electronic Assembly. International Materials Reviews, 1995. **40**(2): p. 65-93.

35. Sheng, G.T.T., et al., Tin whiskers studied by focused ion beam imaging and transmission electron microscopy. Journal of Applied Physics, 2002. **92**(1): p. 64-69.

36. Khosla, A. and H.B. Huntington, Electromigration in Tin Single-Crystals. Journal of Physics and Chemistry of Solids, 1975. **36**(5): p. 395-399.

37. Xu, C., et al., Driving force for the formation of Sn whiskers: Compressive stress - Pathways for its generation and remedies for its elimination and minimization. Ieee Transactions on Electronics Packaging Manufacturing, 2005. **28**(1): p. 31-35.

38. Fisher, R.M., L.S. Darken, and K.G. Carroll, Accelerated Growth of Tin Whiskers. Acta Metallurgica, 1954. **2**(3): p. 368-&.

39. Lin, C.K. and T.H. Lin, Effects of continuously applied stress on tin whisker growth. Microelectronics Reliability, 2008. **48**(10): p. 1737-1740.

40. Jiang, B. and A.P. Man, Whisker growth on tin finishes of different electrolytes. Microelectronics Reliability, 2008. **48**(1): p. 105-110.

41. Nakadaira, Y., et al., Growth of tin whiskers for lead-free plated leadframe packages in high humid environments and during thermal cycling. Microelectronics Reliability, 2008. **48**(1): p. 83-104.

42. Cheng, J., et al., Nucleation and growth of tin whiskers. Applied Physics Letters, 2011. **98**(24).

43. Liu, C.Y., C. Chen, and K.N. Tu, Electromigration in Sn-Pb solder strips as a function of alloy composition. Journal of Applied Physics, 2000. **88**(10): p. 5703-5709.

44. Kim, K.S., J.M. Yang, and J.P. Ahn, The effect of electric current and surface oxidization on the growth of Sn whiskers. Applied Surface Science, 2010. **256**(23): p. 7166-7174.

45. Tao, C.G., W.G. Cullen, and E.D. Williams, Visualizing the Electron Scattering Force in Nanostructures. Science, 2010. **328**(5979): p. 736-740.

46. Ye, H., C. Basaran, and D.C. Hopkins, Deformation of solder joint under current stressing and numerical simulation-I. International Journal of Solids and Structures, 2004. **41**(18-19): p. 4939-4958.

47. Ye, H., C. Basaran, and D.C. Hopkins, Deformation of solder joint under current stressing and numerical simulation-II. International Journal of Solids and Structures, 2004. **41**(18-19): p. 4959-4973.

48. Chen, C., H.Y. Chen, and K.N. Tu, Failure induced by thermomigration of interstitial Cu in Pb-free flip chip solder joints. Applied Physics Letters, 2008. **93**(12).

49. Ryu, C., et al., Microstructure and reliability of copper interconnects. Ieee Transactions on Electron Devices, 1999. **46**(6): p. 1113-1120.

50. Wei, F.L., et al., Electromigration-induced extrusion failures in Cu/low-k interconnects. Journal of Applied Physics, 2008. **104**(2).

51. Cheng, Y.L., W.Y. Chang, and Y.L. Wang, Line-width dependency on electromigration performance for long and short copper interconnects. Journal of Vacuum Science & Technology B, 2010. **28**(5): p. 973-977.

52. Budiman, A.S., et al., Crystal plasticity in Cu damascene interconnect lines undergoing electromigration as revealed by synchrotron x-ray microdiffraction. Applied Physics Letters, 2006. **88**(23).

53. Budiman, A.S., et al., Electromigration-Induced Plasticity: Texture Correlation and Implications for Reliability Assessment. Journal of Electronic Materials, 2009. **38**(3): p. 379-391.

54. Budiman, A.S., et al., Electromigration-Induced Plastic Deformation in Cu Interconnects: Effects on Current Density Exponent, n, and Implications for EM Reliability Assessment. Journal of Electronic Materials, 2010. **39**(11): p. 2483-2488.

55. Zhang, H., G. Wang, and G.S. Cargill, Local melting during electromigration in Cu conductor lines. Journal of Electronic Materials, 2007. **36**(2): p. 117-122.

56. Zhang, H. and G.S. Cargill, Electromigration-induced strain relaxation in Cu conductor lines. Journal of Materials Research, 2011. **26**(4): p. 498-502.

57. Oliver, W.C. and G.M. Pharr, An Improved Technique for Determining Hardness and Elastic-Modulus Using Load and Displacement Sensing Indentation Experiments. Journal of Materials Research, 1992. **7**(6): p. 1564-1583.

58. Pharr, G.M., W.C. Oliver, and F.R. Brotzen, On the Generality of the Relationship among Contact Stiffness, Contact Area, and Elastic-Modulus during Indentation. Journal of Materials Research, 1992. **7**(3): p. 613-617.

59. Doerner, M.F. and W.D. Nix, A method for interpreting the data from depth-sensing indentation instruments. Journal of Materials Research, 1986. **1**(4): p. 601-609.

60. Oliver, W.C. and G.M. Pharr, Measurement of hardness and elastic modulus by instrumented indentation: Advances in understanding and refinements to methodology. Journal of Materials Research, 2004. **19**(1): p. 3-20.

61. Page, T.F., W.C. Oliver, and C.J. Mchargue, The Deformation-Behavior of Ceramic Crystals Subjected to Very Low Load (Nano)Indentations. Journal of Materials Research, 1992. **7**(2): p. 450-473.

62. Gerberich, W.W., et al., Indentation induced dislocation nucleation: The initial yield point. Acta Materialia, 1996. **44**(9): p. 3585-3598.

63. Corcoran, S.G., et al., Anomalous plastic deformation at surfaces: Nanoindentation of gold single crystals. Physical Review B, 1997. **55**(24): p. 16057-16060.

64. Gouldstone, A., et al., Discrete and continuous deformation during nanoindentation of thin films. Acta Materialia, 2000. **48**(9): p. 2277-2295.

65. Gouldstone, A., K.J. Van Vliet, and S. Suresh, Nanoindentation - Simulation of defect nucleation in a crystal. Nature, 2001. **411**(6838): p. 656-656.

66. Suresh, S., T.G. Nieh, and B.W. Choi, Nano-indentation of copper thin films on silicon substrates. Scripta Materialia, 1999. **41**(9): p. 951-957.

67. Bolshakov, A. and G.M. Pharr, Influences of pileup on the measurement of mechanical properties by load and depth sensing indentation techniques. Journal of Materials Research, 1998. **13**(4): p. 1049-1058.

68. Duan, Z.C. and A.M. Hodge, High-temperature Nanoindentation: New Developments and Ongoing Challenges. Jom, 2009. **61**(12): p. 32-36.

69. Schuh, C.A., C.E. Packard, and A.C. Lund, Nanoindentation and contact-mode imaging at high temperatures. Journal of Materials Research, 2006. **21**(3): p. 725-736.

70. Lund, A.C., A.M. Hodge, and C.A. Schuh, Incipient plasticity during nanoindentation at elevated temperatures. Applied Physics Letters, 2004. **85**(8): p. 1362-1364.

71. Schuh, C.A., J.K. Mason, and A.C. Lund, Quantitative insight into dislocation nucleation from high-temperature nanoindentation experiments. Nature Materials, 2005. **4**(8): p. 617-621.

72. Mason, J.K., A.C. Lund, and C.A. Schuh, Determining the activation energy and volume for the onset of plasticity during nanoindentation. Physical Review B, 2006. **73**(5): p. -.

73. Song, S.X., et al., Homogeneous deformation of Au-based metallic glass micropillars in compression at elevated temperatures. Applied Physics Letters, 2009. **94**(6): p. -.

74. Ruffell, S., et al., Nanoindentation-induced phase transformations in silicon at elevated temperatures. Nanotechnology, 2009. **20**(13): p. -.

75. Li, N., et al., Deformation behavior and indentation size effect of Au49Ag5.5Pd2.3Cu26.9Si16.3 bulk metallic glass at elevated temperatures. Intermetallics, 2009. **17**(4): p. 227-230.

76. Volinsky, A.A., N.R. Moody, and W.W. Gerberich, Nanoindentation of Au and Pt/Cu thin films at elevated temperatures. Journal of Materials Research, 2004. **19**(9): p. 2650-2657.

77. Gilman, J.J., Electro-plastic effect in semiconductors. Materials Science and Engineering a-Structural Materials Properties Microstructure and Processing, 2000. **287**(2): p. 272-275.

78. Sherby, O.D. and P.M. Burke, Mechanical Behavior of Crystalline Solids at Elevated Temperature. Progress in Materials Science, 1967. **13**(7): p. 325-&.

79. Mukherje.Ak, J.E. Bird, and J.E. Dorn, Experimental Correlations for High-Temperature Creep. Asm Transactions Quarterly, 1969. **62**(1): p. 155-&.

80. Che, F.X., et al., Creep Properties of Sn-1.0Ag-0.5Cu Lead-Free Solder with Ni Addition. Journal of Electronic Materials, 2011. **40**(3): p. 344-354.

81. Chu, S.N.G. and J.C.M. Li, Impression Creep - New Creep Test. Journal of Materials Science, 1977. **12**(11): p. 2200-2208.

82. Li, J.C.M., Impression creep and other localized tests. Materials Science and Engineering a-Structural Materials Properties Microstructure and Processing, 2002. **322**(1-2): p. 23-42.

83. Mayo, M.J. and W.D. Nix, A Micro-Indentation Study of Superplasticity in Pb, Sn, and Sn-38 Wt-Percent-Pb. Acta Metallurgica, 1988. **36**(8): p. 2183-2192.

84. Murty, K.L., F.M. Haggag, and R.K. Mahidhara, Tensile, creep, and ABI tests on Sn5%Sb solder for mechanical property evaluation. Journal of Electronic Materials, 1997. **26**(7): p. 839-846.

85. Mavoori, H., et al., Creep, stress relaxation, and plastic deformation in Sn-Ag and Sn-Zn eutectic solders. Journal of Electronic Materials, 1997. **26**(7): p. 783-790.

86. McCabe, R.J. and M.E. Fine, High creep resistance tin-based alloys for soldering applications. Journal of Electronic Materials, 2002. **31**(11): p. 1276-1282.

87. Shohji, I., C. Gagg, and W.J. Plumbridge, Creep properties of Sn-8Mass%Zn-3Mass%Bi lead-free alloy. Journal of Electronic Materials, 2004. **33**(8): p. 923-927.

88. Mathew, M.D., et al., Creep deformation characteristics of tin and tin-based electronic solder alloys. Metallurgical and Materials Transactions a-Physical Metallurgy and Materials Science, 2005. **36A**(1): p. 99-105.

89. Zhu, F.L., et al., Effects of temperature and strain rate on mechanical property of Sn96.5Ag3Cu0.5. Journal of Alloys and Compounds, 2007. **438**(1-2): p. 100-105.

90. Zhang, G.S., et al., Creep behavior of eutectic 80Au/20Sn solder alloy. Journal of Alloys and Compounds, 2009. **476**(1-2): p. 138-141.

91. Vianco, P.T., J.A. Rejent, and A.C. Kilgo, Creep behavior of the ternary 95.5Sn-3.9Ag-0.6Cu solder: Part II - Aged condition. Journal of Electronic Materials, 2004. **33**(12): p. 1473-1484.

92. Vianco, P.T., J.A. Rejent, and A.C. Kilgo, Creep behavior of the ternary 95.5Sn-3.9Ag-0.6Cu solder - Part 1: As-cast condition. Journal of Electronic Materials, 2004. **33**(11): p. 1389-1400.

93. Vianco, P.T., et al., Compression stress-strain and creep properties of the 52In-48Sn and 97In-3Ag low-temperature Pb-free solders. Journal of Materials Science-Materials in Electronics, 2007. **18**(1-3): p. 93-119.

94. Park, C., et al., A comparison of impression and compression creep behavior of polycrystalline Sn. Journal of Materials Science, 2007. **42**(13): p. 5182-5187.

95. Lopez, E.P., et al., Compression Stress-Strain Behavior of Sn-Ag-Cu Solders. Journal of Electronic Materials, 2010. **39**(1): p. 97-104.

96. Fang, T.T., R.R. Kola, and K.L. Murty, An Examination of Class-a to Class-M Transition in Pb-9sn and Other Alloys. Metallurgical Transactions a-Physical Metallurgy and Materials Science, 1986. **17**(8): p. 1447-1453.

97. Murty, K.L., Viscous Creep in Pb-9 Sn. Materials Science and Engineering, 1974. **14**(2): p. 169-177.

98. Alizadeh, R., R. Mahmudi, and M.J. Esfandyarpour, Shear punch creep test: A novel localized method for evaluating creep properties. Scripta Materialia, 2011. **64**(5): p. 442-445.

99. Chu, S.N.G. and J.C.M. Li, Impression Creep of Beta-Tin Single-Crystals. Materials Science and Engineering, 1979. **39**(1): p. 1-10.

100. Juhasz, A., et al., Investigation of the Superplasticity of Tin Lead Eutectic by Impression Creep Tests. Journal of Materials Science, 1986. **21**(9): p. 3287-3291.

101. Juhasz, A., P. Tasnadi, and I. Kovacs, SUPERPLASTIC INDENTATION CREEP OF LEAD TIN EUTECTIC. Journal of Materials Science Letters, 1986. **5**(1): p. 35-36.

102. Yang, F.G., J.C.M. Li, and F.Q. Yang, Impression Test of 63sn-37pb Eutectic Alloy. Materials Science and Engineering a-Structural Materials Properties Microstructure and Processing, 1995. **201**(1-2): p. 40-49.

103. Shettigar, S. and P.P. Rao, Study of Superplasticity in Pb-Sn Eutectic Alloy Using Impression Creep Technique. Indian Journal of Engineering and Materials Sciences, 1994. **1**(3): p. 161-164.

104. Balani, K. and F.Q. Yang, Creep behavior of 90 Pb-10 Sn alloy. Physica Status Solidi a-Applied Research, 2003. **198**(2): p. 387-394.

105. Rani, S.D. and G.S. Murthy, Impression creep behaviour of tin based lead free solders. Materials Science and Technology, 2004. **20**(3): p. 403-408.

106. Dutta, I., C. Park, and S. Choi, Impression creep characterization of rapidly cooled Sn-3.5Ag solders. Materials Science and Engineering a-Structural Materials Properties Microstructure and Processing, 2004. **379**(1-2): p. 401-410.

107. Mahmudi, R., A.R. Geranmayeh, and A. Rezaee-Bazzaz, Impression creep behavior of lead-free Sn-5Sb solder alloy. Materials Science and Engineering a-Structural Materials Properties Microstructure and Processing, 2007. **448**(1-2): p. 287-293.

108. Mahmudi, R., et al., Impression creep of hypoeutectic Sn-Zn lead-free solder alloys. Materials Science and Engineering a-Structural Materials Properties Microstructure and Processing, 2008. **491**(1-2): p. 110-116.

109. Mahmudi, R., et al., Effect of rare earth element additions on the impression creep of Sn-9Zn solder alloy. Journal of Materials Science-Materials in Electronics, 2010. **21**(1): p. 58-64.

110. Fujiwara, M. and T. Hirokawa, Indentation Creep Deformation by Pencil Glide in Tin Crystals. Journal of the Japan Institute of Metals, 1992. **56**(2): p. 155-160.

111. Geranmayeh, A.R. and R. Mahmudi, Room-temperature indentation creep of lead-free Sn-5%Sb solder alloy. Journal of Electronic Materials, 2005. **34**(7): p. 1002-1009.

112. Han, Y.D., et al., Temperature Dependence of Creep and Hardness of Sn-Ag-Cu Lead-Free Solder. Journal of Electronic Materials, 2010. **39**(2): p. 223-229.

113. Hare, E.W. and R.G. Stang, Stress-Relaxation Behavior of Eutectic Tin-Lead Solder. Journal of Electronic Materials, 1995. **24**(10): p. 1473-1484.

114. Baker, E. and T.J. Kessler, INFLUENCE OF TEMPERATURE ON STRESS RELAXATION IN A CHILL-CAST, TIN-LEAD SOLDER. Ieee Transactions on Parts Hybrids and Packaging, 1973. **PHP9**(4): p. 243-246.

115. Kashyap, B.P. and G.S. Murty, EXPERIMENTAL CONSTITUTIVE RELATIONS FOR THE HIGH-TEMPERATURE DEFORMATION OF A PB-SN EUTECTIC ALLOY. Materials Science and Engineering, 1981. **50**(2): p. 205-213.

116. Arrowood, R. and A.K. Mukherjee, STRESS-RELAXATION OF A EUTECTIC ALLOY IN THE SUPERPLASTIC CONDITION. Materials Science and Engineering, 1987. **92**: p. 33-41.

117. Liu, H.Y., et al., Enhanced stress relaxation of Sn-3.8Ag-0.7Cu solder by electrical current. Journal of Materials Research, 2010. **25**(6): p. 1172-1178.

118. Zhu, Q.S., et al., Stress relaxation behavior of Cu/Sn/Cu micro-connect after electrical current. Materials Science and Engineering a-Structural Materials Properties Microstructure and Processing, 2011. **528**(3): p. 1467-1471.

119. Nix, W.D. and E. Arzt, On Void Nucleation and Growth in Metal Interconnect Lines under Electromigration Conditions. Metallurgical Transactions a-Physical Metallurgy and Materials Science, 1992. **23**(7): p. 2007-2013.

120. Gungor, M.R. and D. Maroudas, Modeling of electromechanically-induced failure of passivated metallic thin films used in device interconnections. International Journal of Fracture, 2001. **109**(1): p. 47-68.

121. Zhao, G.F. and F.Q. Yang, Effect of alternating electric current on the nanoindentation of copper. Applied Physics a-Materials Science & Processing, 2012. **109**(3): p. 553-559.

122. Yang, F.Q. and G.F. Zhao, Effect of Electric Current on Nanoindentation of Copper. Nanoscience and Nanotechnology Letters, 2010. **2**(4): p. 322-326.

123. Park, Y.B., R. Monig, and C.A. Volkert, Thermal fatigue as a possible failure mechanism in copper interconnects. Thin Solid Films, 2006. **504**(1-2): p. 321-324.

124. Zhang, J., et al., Unusual thermal fatigue behaviors in 60 nm thick Cu interconnects. Scripta Materialia, 2009. **60**(4): p. 228-231.

125. Zhao, G.F., M. Liu, and F.Q. Yang, The effect of an electric current on the nanoindentation behavior of tin. Acta Materialia, 2012. **60**(9): p. 3773-3782.

126. Shao, S.S., F.Q. Yang, and F.Z. Xuan, Effect of electromigration on diffusional creep in polycrystalline materials. International Journal of Applied Electromagnetics and Mechanics, 2012. **40**(2): p. 165-171.

127. Harris, C.O., Introduction to stress analysis1959, New York,: Macmillan. 330 p.

128. Chen, K., et al., Plastic deformation in Al (Cu) interconnects stressed by electromigration and studied by synchrotron polychromatic x-ray microdiffraction. Journal of Applied Physics, 2008. **104**(1).

129. Jr., W.D.C. and D.G. Rethwisch, Materials science and engineering: an introduction2009: John Wiley & Sons, Inc. .

130. P.M.Opsal, et al., Properties of materias. in Standard Handbook for Electrical Engineers2007: McGraw Hill.

131. Fang, T.H. and W.J. Chang, Nanomechanical properties of copper thin films on different substrates using the nanoindentation technique. Microelectronic Engineering, 2003. **65**(1-2): p. 231-238.

132. Hsieh, J.Y., et al., Temperature dependence in nanoindentation of a metal substrate by a diamondlike tip. Physical Review B, 2004. **70**(19).

133. Chen, R. and F. Yang, Effect of DC Current on the Creep Deformation of Tin. Journal of Electronic Materials, 2010. **39**(12): p. 2611-2617.

134. Chen, R. and F. Yang, Impression creep of a Sn60Pb40 alloy: the effect of electric current. Journal of Physics D-Applied Physics, 2008. **41**(15).

135. Yang, F., Current-induced thermal stresses in a metal cylinder. Journal of Applied Physics, 2009. **106**(11).

136. Srinivasarao, V., et al. Nanoindentation study of the sputtered Cu thin films for interconnect applications. in Electronics Packaging Technology Conference, 2004. EPTC 2004. Proceedings of 6th. 2004.

137. Black, J.R., ELECTROMIGRATION FAILURE MODES IN ALUMINUM METALLIZATION FOR SEMICONDUCTOR DEVICES. Proceedings of the Ieee, 1969. **57**(9): p. 1587-&.

138. Michael, N.L., et al., Electromigration failure in ultra-fine copper interconnects. Journal of Electronic Materials, 2003. **32**(10): p. 988-993.

139. Gladkikh, A., et al., HILLOCK FORMATION DURING ELECTROMIGRATION IN CU AND AL THIN-FILMS - 3-DIMENSIONAL GRAIN-GROWTH. Applied Physics Letters, 1995. **66**(10): p. 1214-1215.

140. Nitta, T., et al., ELECTRICAL-PROPERTIES OF GIANT-GRAIN COPPER THIN-FILMS FORMED BY A LOW KINETIC-ENERGY PARTICLE PROCESS. Journal of the Electrochemical Society, 1992. **139**(3): p. 922-927.

141. Park, C.W. and R.W. Vook, Activation-Energy for Electromigration in Cu Films. Applied Physics Letters, 1991. **59**(2): p. 175-177.

142. Chen, K.-C., et al., Stability of nanoscale twins in copper under electric current stressing. Journal of Applied Physics, 2010. **108**(6).

143. Ogi, H., et al., Significant softening of copper nanowires during electromigration studied by picosecond ultrasound spectroscopy. Physical Review B, 2010. **82**(15).

144. Sebastian, S. and S.K. Biswas, EFFECT OF INTERFACE FRICTION ON THE MECHANICS OF INDENTATION OF A FINITE LAYER RESTING ON A

RIGID SUBSTRATE. Journal of Physics D-Applied Physics, 1991. **24**(7): p. 1131-1140.

145. Poole, W.J., M.F. Ashby, and N.A. Fleck, Micro-hardness of annealed and work-hardened copper polycrystals. Scripta Materialia, 1996. **34**(4): p. 559-564.

146. Chaudhri, M.M., Subsurface strain distribution around Vickers hardness indentations in annealed polycrystalline copper. Acta Materialia, 1998. **46**(9): p. 3047-3056.

147. Yang, F. and G. Zhao, Effect of Electric Current on Nanoindentation of Copper. Nanoscience and Nanotechnology Letters, 2010. **2**(4): p. 322-326.

148. Chen, R. and F. Yang, Effect of electric current on the creep deformation of lead. Materials Science and Engineering a-Structural Materials Properties Microstructure and Processing, 2011. **528**(6): p. 2319-2325.

149. Yang, F., et al., Deformation in a Zr57Ti5CU20Ni8Al10 bulk metallic glass during nanoindentation. Acta Materialia, 2007. **55**(1): p. 321-327.

150. Deng, X., et al., Deformation behavior of (Cu, Ag)-Sn intermetallics by nanoindentation. Acta Materialia, 2004. **52**(14): p. 4291-4303.

151. Atkinson, M., ORIGIN OF THE SIZE EFFECT IN INDENTATION OF METALS. International Journal of Mechanical Sciences, 1991. **33**(10): p. 843-850.

152. Manika, E. and J. Maniks, Size effects in micro- and nanoscale indentation. Acta Materialia, 2006. **54**(8): p. 2049-2056.

153. Fleck, N.A. and J.W. Hutchinson, A reformulation of strain gradient plasticity. Journal of the Mechanics and Physics of Solids, 2001. **49**(10): p. 2245-2271.

154. Gudmundson, P., A unified treatment of strain gradient plasticity. Journal of the Mechanics and Physics of Solids, 2004. **52**(6): p. 1379-1406.

155. Muhlhaus, H.B. and E.C. Aifantis, A VARIATIONAL PRINCIPLE FOR GRADIENT PLASTICITY. International Journal of Solids and Structures, 1991. **28**(7): p. 845-857.

156. Joslin, D.L. and W.C. Oliver, A NEW METHOD FOR ANALYZING DATA FROM CONTINUOUS DEPTH-SENSING MICROINDENTATION TESTS. Journal of Materials Research, 1990. **5**(1): p. 123-126.

157. Zhang, T.Y., W.H. Xu, and M.H. Zhao, The role of plastic deformation of rough surfaces in the size-dependent hardness. Acta Materialia, 2004. **52**(1): p. 57-68.

158. Zhang, T.Y. and W.H. Xu, Surface effects on nanoindentation. Journal of Materials Research, 2002. **17**(7): p. 1715-1720.

159. Xu, L., J.H.L. Pang, and K.N. Tu, Effect of electromigration-induced back stress gradient on nanoindentation marker movement in SnAgCu solder joints. Applied Physics Letters, 2006. **89**(22).

160. Nah, J.W., et al., Effect of electromigration on mechanical shear behavior of flip chip solder joints. Journal of Materials Research, 2006. **21**(3): p. 698-702.

161. Ren, F., et al., Electromigration induced ductile-to-brittle transition in lead-free solder joints. Applied Physics Letters, 2006. **89**(14).

162. Kumar, A., et al., Effect of Electromigration on the Mechanical Performance of Sn-3.5Ag Solder Joints with Ni and Ni-P Metallizations. Journal of Electronic Materials, 2009. **38**(1): p. 78-87.

163. Lorenz, D., et al., Pop-in effect as homogeneous nucleation of dislocations during nanoindentation. Physical Review B, 2003. **67**(17).

164. Kiely, J.D., et al., Initial stages of yield in nanoindentation. Journal of Materials Research, 1999. **14**(6): p. 2219-2227.

165. Gerberich, W.W., et al., THE INJECTION OF PLASTICITY BY MILLINEWTON CONTACTS. Acta Metallurgica Et Materialia, 1995. **43**(4): p. 1569-1576.

166. Meyers, M.A. and K.K. Chawla, Mechanical behavior of materials. 2nd ed2009, Cambridge ; New York: Cambridge University Press. xxii, 856 p.

167. Lawn, B.R., Indentation of ceramics with spheres: A century after Hertz. Journal of the American Ceramic Society, 1998. **81**(8): p. 1977-1994.

168. Yang, F. and J.C.M. Li, Deformation behavior of tin and some tin alloys. Journal of Materials Science-Materials in Electronics, 2007. **18**(1-3): p. 191-210.

169. Rotherham, L., A.D.N. Smith, and G.B. Greenough, INTERNAL FRICTION AND GRAIN-BOUNDARY VISCOSITY OF TIN. Journal of the Institute of Metals, 1951. **79**(12): p. 439-454.

170. Briscoe, B.J., L. Fiori, and E. Pelillo, Nano-indentation of polymeric surfaces. Journal of Physics D-Applied Physics, 1998. **31**(19): p. 2395-2405.

171. Ngan, A.H.W. and B. Tang, Viscoelastic effects during unloading in depth-sensing indentation. Journal of Materials Research, 2002. **17**(10): p. 2604-2610.

172. Geng, K.B., et al., Nanoindentation behavior of ultrathin polymeric films. Polymer, 2005. **46**(25): p. 11768-11772.

173. Nix, W.D. and H.J. Gao, Indentation size effects in crystalline materials: A law for strain gradient plasticity. Journal of the Mechanics and Physics of Solids, 1998. **46**(3): p. 411-425.

174. Chen, R. and F.Q. Yang, Electrocontact heating in a Sn60-Pb40 solder alloy. Journal of Physics D-Applied Physics, 2008. **41**(6).

175. Chiao, M. and L.W. Lin, Self-buckling of micromachined beams under resistive heating. Journal of Microelectromechanical Systems, 2000. **9**(1): p. 146-151.

176. Yang, F.Q., Current-induced thermal stresses in a metal cylinder. Journal of Applied Physics, 2009. **106**(11).

177. Ren, F., et al., Electromigration induced ductile-to-brittle transition in lead-free solder joints. Applied Physics Letters, 2006. **89**(14).

178. Liu, H.Y., et al., Stress relaxation behavior of Cu/Sn/Cu micro-connect after electrical current. Materials Science and Engineering a-Structural Materials Properties Microstructure and Processing, 2011. **528**(3): p. 1467-1471.

179. Chen, R. and F.Q. Yang, Impression creep of a Sn60Pb40 alloy: the effect of electric current. Journal of Physics D-Applied Physics, 2008. **41**(15).

180. Kumar, P. and I. Dutta, Influence of electric current on diffusionally accommodated sliding at hetero-interfaces. Acta Materialia, 2011. **59**(5): p. 2096-2108.

181. Fangohr, H., et al., Joule heating in nanowires. Physical Review B, 2011. **84**(5).

182. Garofalo, F., An Empirical Relation Defining Stress Dependence of Minimum Creep Rate in Metals. Transactions of the Metallurgical Society of Aime, 1963. **227**(2): p. 351-&.

183. Montes, J.M., F.G. Cuevas, and J. Cintas, New creep law. Materials Science and Technology, 2012. **28**(3): p. 377-379.

184. Chen, I.W. and A.S. Argon, Steady-State Power-Law Creep in Heterogeneous Alloys with Coarse Microstructures. Acta Metallurgica, 1979. **27**(5): p. 785-791.

185. Wilkinson, D.S. and M.F. Ashby, Pressure Sintering by Power Law Creep. Acta Metallurgica, 1975. **23**(11): p. 1277-1285.

186. Breen, J.E. and J. Weertman, Creep of Polycrystalline Tin. Transactions of the American Institute of Mining and Metallurgical Engineers, 1955. **203**(11): p. 1230-1234.

187. Frenkel, R.E., O.D. Sherby, and J.E. Dorn, Activation Energies for Creep of Cadmium, Indium, and Tin. Acta Metallurgica, 1955. **3**(5): p. 470-472.

188. Suh, S.H., J.B. Cohen, and J. Weertman, X-Ray-Diffraction Studies on the Misorientation of Subgrains during Creep of Tin Single-Crystals. Scripta Metallurgica, 1981. **15**(5): p. 517-522.

189. Weertman, J., Compressional Creep of Tin Single Crystals. Journal of Applied Physics, 1957. **28**(2): p. 196-197.

190. Weertman, J. and J.E. Breen, Creep of Tin Single Crystals. Journal of Applied Physics, 1956. **27**(10): p. 1189-1193.

191. Balasubr.N and J.C.M. Li, Activation Areas for Creep Deformation. Journal of Materials Science, 1970. **5**(5): p. 434-&.

192. Suh, S.H., J.B. Cohen, and J. Weertman, X-Ray-Diffraction Study of Subgrain Misorientation during High-Temperature Creep of Tin Single-Crystals. Metallurgical Transactions a-Physical Metallurgy and Materials Science, 1983. **14**(1): p. 117-126.

193. Fensham, P.J., Self-Diffusion in Tin Crystals. Australian Journal of Scientific Research Series a-Physical Sciences, 1950. **3**(1): p. 91-104.

194. Mei, Z., et al., Superplastic Creep of Eutectic Tin-Lead Solder Joints. Journal of Electronic Materials, 1990. **19**(11): p. 1273-1280.

195. Adeva, P., et al., Microstructure and High-Temperature Mechanical-Properties of Tin. Materials Science and Engineering a-Structural Materials Properties Microstructure and Processing, 1995. **194**(1): p. 17-23.

196. Fujiwara, M. and M. Otsuka, Indentation creep of beta-Sn and Sn-Pb eutectic alloy. Materials Science and Engineering a-Structural Materials Properties Microstructure and Processing, 2001. **319**: p. 929-933.

197. Fujiwara, M. and M. Otsuka, Characterization of micro-indentation creep in beta-Sn single crystals at elevated temperatures. Journal of the Japan Institute of Metals, 1999. **63**(6): p. 760-769.

198. Puttick, K.E. and R. King, Boundary Slip in Bicrystals of Tin. Journal of the Institute of Metals, 1952. **80**(10): p. 537-&.

199. Mohamed, F.A., K.L. Murty, and J.W. Morris, Harper-Dorn Creep in Al, Pb, and Sn. Metallurgical Transactions, 1973. **4**(4): p. 935-940.

Vita

Guangfeng Zhao was born in the county of Juxian, Shandong Province, P. R. China.

Education

Master, Materials Science and Engineering, Shandong University, Jinan, 2008

Bachelor, Materials Science and Engineering, Shandong University, Jinan, 2005

Publication

1. **Zhao, G.F.**, M. Liu, Z. An, Y. Ren, P.K. Liaw, and F.Q. Yang, Electromechanical responses of Cu strips, Applied Physics Letters, in press

2. **Zhao, G.F.** and F.Q. Yang, Effect of alternating electric current on the nanoindentation of copper. Applied Physics a-Materials Science & Processing, 2012. **109**(3): p. 553-559

3. **Zhao, G.F.**, M. Liu, and F.Q. Yang, The effect of an electric current on the nanoindentation behavior of tin. Acta Materialia, 2012. **60**(9): p. 3773-3782

4. Yang, F.Q. and **G.F. Zhao**, Effect of Electric Current on Nanoindentation of Copper. Nanoscience and Nanotechnology Letters, 2010. **2**(4): p. 322-326

5. Shao G., **G.F. Zhao**, C.Y. Xu, F.Q. Yang, and L.N. An, Ceramic nanocomposites reinforced with a high volume fraction of carbon nanofibers. Materials Letters, 2012. **68**: p. 108-111

6. Lee Y.K., **G.F. Zhao**, B. Yu, H. Lim, and H. Lu, Goniochromatic properties of human tooth dentin, Color Research and Application 2012. **37**: p. 206-211

7. Yu B., **G.F. Zhao**, J.I. Lim, and Y.K. Lee, Compressive mechanical properties of bovine cortical bone under varied loading rate, Proceedings of the Institution of Mechanical Engineers, Part H: Journal of Engineering in Medicine 2011. **225**: p. 941-947

8. Yu B., **G.F. Zhao**, H. Lim, J.I. Lim, and Y.K. Lee, Influence of aging and 2-hydroxyethyl-methacrylate content on the color stability of experimental 2-hydroxyethyl-methacrylate-added dental glass ionomers, Journal of Materials Science & Technology, 2010, **26**: p. 379-384

9. Lee Y.K., B. Yu, **G.F. Zhao**, and J.I. Lim, Effect of aging and HEMA content on the translucency, fluorescence, and opalescence properties of experimental HEMA-added glass ionomers, Dental Materials Journal 2010, **29**: p. 9-14

10. Wang A.J., Y.P. Lu, R.F. Zhu, S.T. Li, G.Y. Xiao, **G.F. Zhao,** and W.H. Xu, Effect of sintering on porosity, phase, and surface morphology of spray dried hydroxyapatite microspheres, Journal of Biomedical Materials Research Part A, 2008, **87A**: p. 557-562

Conference Presentation

1. **Zhao G.F.** and F.Q. Yang, Effect of electric current on the tensile creep of tin, Materials Science & Technology 2012, Pittsburgh, October 2012

2. **Zhao G.F.** and F.Q. Yang, Nanoindentation of pure tin: effect of electric current, Materials Science & Technology 2011, Columbus, October 2011

Professional Affiliations

Student Member in Materials Advantage, 2011 – present